Numerical study of the non-Oberbeck-Boussinesq effects in turbulent water-filled cavities

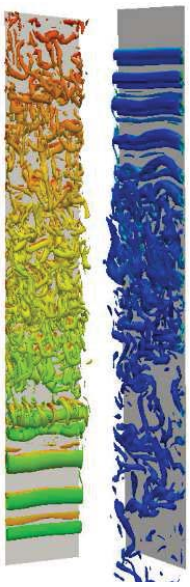

Centre Tecnològic de Transferència de Calor
Departament de Màquines i Motors Tèrmics
Universitat Politècnica de Catalunya

Deniz Kizildag

Doctoral Thesis

Numerical study of the non-Oberbeck-Boussinesq effects in turbulent water-filled cavities

Deniz Kizildag

TESI DOCTORAL

presentada al

Departament de Màquines i Motors Tèrmics
E.S.E.I.A.A.T.
Universitat Politècnica de Catalunya

per a l'obtenció del grau de

Doctor per la Universitat Politècnica de Catalunya

Terrassa, January, 2016

Numerical study of the non-Oberbeck-Boussinesq effects in turbulent water-filled cavities

Deniz Kizildag

Directors de la Tesi

Dr. Ivette Rodríguez

Dr. F. Xavier Trias

Tutor de la Tesi

Dr. Assensi Oliva

Tribunal Qualificador

Dr. Antonio Pascau
Universidad de Zaragoza

Dr. Andrey Gorobets
Keldysh Institute of Applied Mathematics of RAS

Dr. Joaquim Rigola
Universitat Politècnica de Catalunya

Anneme ve Babama

Kızım Aylin'e

ve

Eşim Queralt'a

Cada año, cuando la primavera se posa sobre las flores, cuando la tierra canta nanas, llegan los pastores de todas las partes del Ararat, extienden sus capas sobre la tierra cobriza de las orillas del lago y se sientan sobre una tierra de mil años de amor. Cuando despunta el alba, sacan las flautas de sus cintos y tocan la ira y el amor del Ararat. Y cuando el sol se pone, llega un pájaro blanco...

La leyenda del monte Ararat, Yaşar Kemal

Acknowledgements

First and foremost, I would like to express my gratitude to Prof. Assensi Oliva, who offered me the possibility of pursuing doctoral studies and introduced me to the fascinating world of heat transfer and fluid dynamics. I highly appreciate all his contributions of time and ideas to make my research experience stimulating. I highly value his never-ending enthusiasm in transmitting the joy of doing useful stuff with much of dedication and hard work. He both consciously and unconsciously provided me an example, which most probably will affect the way I think and act till the end of my life.

Secondly, I'm very grateful to Ivette Rodríguez who has contributed immensely in my research. Her ability to interpret and visualize the physical phenomena opened up new horizons in my understanding of the physics of the turbulent flow in the cavity. I'm very thankful to Ivette, also because of her dedication and help in making this dissertation thesis possible. She worked day and night to revise this manuscript, to make new suggestions which later proved to be key points in capturing the physics lying behind the Non-Oberbeck-Boussinesq phenomena. It has not always been easy, there have been tough moments. However, all her contributions in a way or another, helped me grow in my research and also personally.

This dissertation has been possible thanks to Xavi Trias, who introduced me to the direct numerical simulations of the differentially heated cavity. His admirable work in the subject made the things much easier. I very much benefited from our conversations during coffee-time. His analytical thinking and mathematical power was always an inspiration. I am grateful to Xavi, not only for his patience and availability throughout my research period, but also for his friendship and for all the nice moments we lived in these years.

I also would like to thank specially Cristian Orozco, who guided me through the initial stages of my PhD project. He provided very didactic conversations, introducing me to the concept of the verification of transient CFD results. Although not directly related with this PhD project, it was a pleasure to learn from him the concept of moving boundaries.

Indeed, I am indebted to all the members of CTTC Group for their intellectual or personal contributions. I feel privileged to have met you, and to have shared an important portion of my life around you. Without your help, none of the work I did could have been possible. I would like to show my gratitude to:

Guillem Colomer, for always coming up with a solution each time I asked for advice. Jorge Chiva, Octavi Pavon, Ramiro Alba, and Dani Fernández for solving any problem related with computers. Nicolás Ablanque, Marlon Alegre, and Rashmin Damle, for the great friendship, and for their patience in listening with interest all my irrelevant conversations. Prof. David Pérez-Segarra, Quim Rigola, Carles

Oliet, and Joan López, for being a role model in integrity and work ethics. Oriol Lehmkuhl, Jordi Ventosa, Jesus Castro, and Debora Faggembauu, for useful conversations on TermoFluids code, variable thermophysical properties, solar collectors, and building façades. Joan Farnós, for his friendship, and for motivating me during the last stages of my PhD work. Joan Calafell, Ricard Borrell, Daniel Martínez, Imanol Aizpurua, Sergio Morales, Ángel Carmona, and Eduardo García for the interesting conversations they offered during the lunch time. Manolo Ordoñez and Víctor Ruíz, for helping me with the experimental work. Guillermo Oyarzun, Santiago Torras, and Pedro Galione, for contributing in the superiority of the *Rest of the World* team. Lluís Jofre and Jordi Muela, for giving me a ride in *Bus Maresme*. Firas Dabbagh, Hamdi Kessentini, and Nicolás Valle, for helping me with data visualization issues and the collector tests. Roser Capdevila, Giorgos Papakokkinos, and Arnau Pont, for sharing office with me.

I would like to acknowledge *Agència de Gestió i Ajuts Universitaris i de Recerca*, and *Ministerio de Educación, Cultura y Deporte* for partly financing me during the PhD project. Some of the DNS calculations have been performed on the IBM MareNostrum supercomputer at the Barcelona Supercomputing Center, whose support is highly appreciated.

Voldria agrair molt especialment a: Santiago, Maruja, Pilar, Rafel, Mariona, Jaume, Raül, Xavi, Fer, Clàudia, Rafa, Montse, Oriol i Ferran, per ser la meva Família, per la seva amistat i suport. Especialment voldria donar les gràcies a la Maruja i a la Pilar, sense la seva ajuda no hauria estat possible.

Benim için arkadaştan da öte olan, iyi ve kötü günde hep yanımda olduklarını bildiğim, hep aynı konular bile olsa konuşmak ve paylaşmaktan hiç bıkmadığım ve bıkmayacağım Yeşilvadi'den Bora, Hakan, İlker, Cemer, Berk, Aytaç ve Cemmen'e de çok teşekkür ederim.

Beni hep cesaretlendiren Çağrı'ya, ailemizin neşe kaynağı olan Defne ve Oğuz'a, bu yola beraber çıktığım kardeşim Sema'ya da çok şey borçluyum.

Bu tezi, hayattaki tek önceliği benim ve kardeşimin mutluluğu olan, bir baltaya sap olmam için türlü fedakarlıklarda bulunan, beni hayata getiren ve sevgi ile büyüten, her zaman nazımı çekeceklerini bildiğim, canım *Annem* ve *Babam*'a armağan ediyorum.

Yakın zaman önce karşıma çıkan, ama sanki hep varmış gibi olan, bana verdiklerini kelimelere sığdıramayacağım kızım Aylin'e, ve...

Per últim, i no menys important, a la meva dona Queralt per aguantar-me durant tots aquests anys, per ser la meva inspiració, i per donar sentit a la meva existència. Te la dedico...

Deniz Kızıldağ, January 2016

Contents

Abstract

The work carried out in the framework of the present thesis is motivated by the modeling of a particular integrated collector-storage element of water, mounted into a building façade. Given the complex phenomenology taking place within this collector-storage element, the success in the prediction of the thermal behavior of the whole façade is highly dependent on the proper resolution of this element, which involves the turbulent natural convection flow of water. At a first glance, two issues regarding the collector-storage element modeling have to be concerned: i) the simplicity of the available widely-used collector-storage models which do not allow for capturing the complex phenomena involved in the water-filled cavities, ii) the established practice of employing constant thermophysical properties, which could partly be responsible for the mismatch between the numerical models and experimental measurements encountered for situations like those addressed in this work. Thus, this work aims at shedding light into these two issues by means of numerical studies of turbulent differentially heated cavity flow of water, considering the potential of this flow configuration to model the particular collector-storage element to be analyzed.

First, the relevance of the variable thermophysical properties have been submitted to investigation by means of direct numerical simulations of a differentially heated cavity flow using the aspect ratio of a particular prototype. The simulations consider the so-called non-Oberbeck-Boussinesq effects, and study the temperature range for which these effects could be considered relevant. The work has been conducted employing a two-dimensional flow assumption, estimating that this methodology -promoted by the necessity of a compromise between the accuracy and the cost of the simulations- would be valid to detect the non-Oberbeck-Boussinesq effects without the loss of generality, even though the actual flow structures of the flow are inherently three-dimensional. The numerical results have revealed that up to the temperature difference of 30 °C, Oberbeck-Boussinesq solution can estimate the heat transfer with about 1 % error, although the loss of symmetry of the flow is certified even for a temperature difference of 10 °C. Moreover, it has been observed that the boundary layers at hot and cold isothermal confining walls behave differently, such that the boundary layer instabilities and transition to turbulence location move downstream along the hot wall and upstream along the cold wall. As a consequence, the stratification region shifts upwards, giving rise to higher stratification numbers.

Later, the non-Oberbeck-Boussinesq effects have been studied considering three-dimensional domain by means of direct numerical simulations, in the quest of analyzing their impact on the three-dimensional flow structure. The results have revealed delayed transition in the hot wall and earlier triggered transition in the cold

wall boundary layers. This has been shown to be a consequence of the initial heating of the cavity due to favorable heat transfer properties in the hot wall boundary layer, which results in warmer upper cavity. As time advances, due to the influence of the stratified flow feeding the hot and cold boundary layers, the strength of the natural convection gradually decreases and increases in the hot and cold boundary layers, respectively. When a balance is attained between these two boundary layers, the cold wall boundary is found at higher equivalent Rayleigh number, justifying its premature transition. Accordingly, the early transitioning cold wall boundary layer has been found considerably thicker. This boundary layer interacts actively with the hot wall boundary layer, causing vertical oscillations in the transition to turbulent locations on both boundary layers. This interaction is also responsible for the degradation of the already shifted stratification zone. This important effect is not captured by means of two-dimensional simulations, which makes the two dimensional flow hypothesis not valid when it comes to describe the flow characteristics with non-Oberbeck-Boussinesq effects. As for the heat transfer, the non-Oberbeck-Boussinesq effects do not necessarily enhance the heat transfer, as Oberbeck-Boussinesq solution is observed to overestimate the Nusselt number by about 3 %.

Last but not the least, considering the huge computational resources required for simulating these turbulent natural convection flows with water, and bearing in mind the importance of an appropriate modeling of the present phenomena, different subgrid-scale models have been analyzed in order to predict the thermal and fluid dynamics of the flow within a turbulent water-filled cavity. It has been shown that the performance of the models is directly linked to the accurate prediction of the transition to turbulence, which is the main challenge in the proper modeling of this phenomena.

The computed data and the results obtained within the framework of the present thesis will be made available for the research community via their publication on the CTTC database.

Chapter 1

Introduction

1.1 Prologue

1.1.1 Motivation

The existing buildings account for over 40 % of the total energy consumption in Europe. Growth in population, increasing demand for building services and comfort levels, together with the rise in time spent inside the buildings, indicate that the upward trend in energy consumption within buildings will continue to grow [1]. This fact not only stimulates the efforts in the development of innovative and efficient products of reduced environmental impact, but also makes necessary tools and methodologies for analyzing the performance of these products and the buildings into which they are integrated.

The envelopes play an important role in the thermal behavior of the buildings. In addition to fulfilling the architectural requirements, the energy efficient design of the building envelopes can contribute greatly in reducing the heating and cooling loads of the dwellings [2]. Multi-functional ventilated façades appear as an interesting solution taking into consideration aspects like improved thermal behavior, acoustic insulation and daylight illumination, attractive outdoor aspect, possibility of incorporating innovative elements.

In this context, the use of an integrated collector storage in the building façade might be one of the possibilities that this kind of innovative concept might offer. The work carried out in this thesis is motivated by the modeling of a double skin façade component mounted into a building façade. The module is composed of different elements where an external single-pane glass skin is separated from the inner skin by a ventilation channel. Natural and forced convection operational modes are possible. The inner skin consists of two zones: i) the upper double-pane glass skin, ii) the lower integrated collector-storage element (see Figure 1.1).

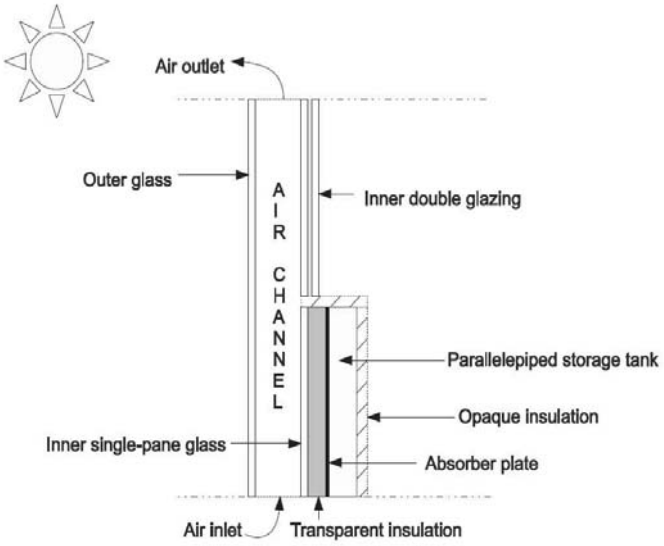

Figure 1.1: Scheme of a collector-storage element integrated into a multi-functional faade module.

In the context of the simulation of integrated collector storage, the main issues observed were the simplicity of the vast majority of the available models in the literature and the established use of constant thermophysical properties in these models. The former, i.e. the use of simplified models such as the multinode model [3], can not take into consideration the complex phenomena associated with tall water-filled cavities, such as the laminar-turbulent transition and its effect on the heat transfer. The latter is related with the impact of variable thermophysical properties when large temperature gradients are found between the hot and cold walls. The combination of both effects were the possible causes of the differences encountered between numerical simplified models and the experimental measurements (see for instance Appendix A). It is in this framework that the present thesis is developed, and also based on previous experiences at CTTC in modeling air-filled cavities [4, 5, 6, 7].

1.1.2 Transient natural convection in cavities

Transient natural convection in cavities has attracted the researchers due to its implications in numerous engineering applications such as in the thermal design of build-

ings, solar collectors, nuclear reactor design, cooling of electronic devices, amongst many others. The problem of natural convection was studied analytically by Batchelor [8] and since then it has received the attention of many researchers. Indeed, substantial work has been devoted to two canonical configurations: i) a cavity heated from below; ii) a cavity heated from the sides. The first configuration is known as the Rayleigh-Bénard problem, where the gravitational vector is parallel to the thermal gradient. The latter case is commonly referred to as the differentially heated cavity (DHC) problem.

So far, most of the studies conducted -whether they address the Rayleigh-Bénard or the differentially heated cavity problems- have considered constant thermophysical properties, i.e. the so-called Oberbeck-Boussinesq approximation (see for instance [9, 10, 11, 12]). Although the differentially heated cavity configuration represents a simple geometry, the flow gets complex for sufficiently large Rayleigh numbers (see for instance [13]). The flow undergoes a gradual transition to a chaotic state as the Rayleigh number reaches a critical value. In these cavities, both laminar, transitional, and turbulent zones are expected to coexist within the domain (see Figure 1.2). Generally, the core of the cavity together with the upstream part of the vertical boundary layers remain laminar while after some location in the downstream part of the vertical boundary layers, the transition to turbulent regime occurs. With these complex phenomena present, it is a challenging task to detect accurately the location of the transition to turbulence [5].

When it comes to the numerical simulation of these cavities, there is a large amount of contributions using Reynolds-Averaged Navier-Stokes equations (RANS) (see for instance [14, 15, 16]), large-eddy simulations (LES) (e.g. [13, 17]) and direct numerical simulations (DNS) (e.g. [18, 19, 20, 5, 6]). The conducted studies so far showed that the accurate assessment of the transition location is essential in predicting flow configuration in a turbulent DHC flow. However, most of the previous works on this kind of cavities have focused on air-filled cavities ($Pr \approx 0.7$). In the case of a water-filled cavity, i.e. greater Prandtl number compared with air, obtaining solutions for the governing equations gets more complicated since the thermal boundary layer becomes thinner for the same Rayleigh number [9]. Therefore, finer grids are required to capture the smallest scales of the flow. This may be one of the reasons explaining that numerical studies of water-filled DHC are quite scarce when compared with air-filled ones and are generally limited to a two-dimensional domain [21, 22].

1.1.3 Water-filled cavities. Major challenges

In many engineering applications, with both air and water-filled cavities, due to the large temperature gradients across the fluid medium, thermophysical properties exhibit a significant variation. This is especially true in the case of water-filled cavities,

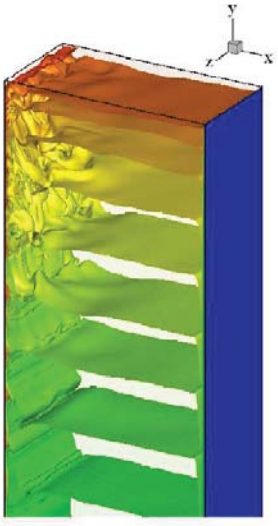

Figure 1.2: Laminar to turbulence transition in the vicinity of the hot wall in a differentially heated cavity. Notice that part of the cavity is dominated by the laminar and stratified zones.

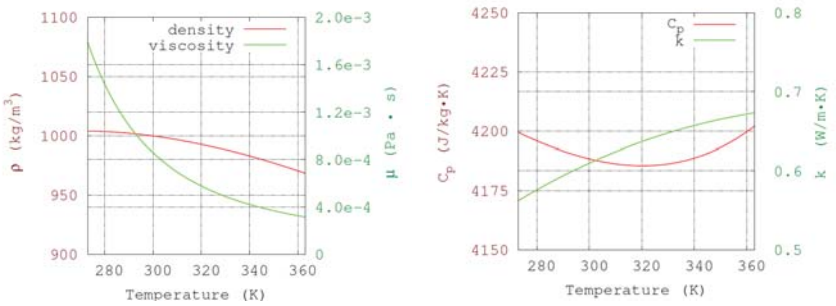

(a) (b)

Figure 1.3: Variation of the water thermophysical properties with the temperature (a) Density and viscosity; (b) heat capacity and conductivity.

where the variation of the viscosity with the temperature is rather large (see figure 1.3). In this kind of situations, the impact of this variable property on the natural convection should be addressed as it might imply significant variations in the flow configuration and in the heat transfer.

In such situations, the validity of the Oberbeck-Boussinesq (OB) approximation has to be questioned. This hypothesis is a good approximation if the fluid properties are weakly dependent on the temperature or the temperature difference within the walls are small enough. According to Gray and Giorgini [23], the use of the OB approximation can be considered valid for variations of thermophysical properties up to 10% with respect to the mean value.

When it comes to the influence of the thermophysical properties on the turbulent phenomena taking place in these cavities, most of the research has been performed on Rayleigh-Bénard cavities (e.g. [24, 25, 26]). The effect of the variable thermophysical properties on the transition to turbulence and in a more general sense on the fluid dynamics and heat transfer taking place in DHC have received lesser attention being most of the work performed limited to relatively low Rayleigh numbers.

1.2 Objectives

Based on the foregoing, this thesis will focus on:

- Exploring the limits of the Oberbeck-Boussinesq approximation in the natural convection of water-filled tall cavities. This approximation is valid if the

fluid properties are weakly dependent on the temperature or the temperature difference within the walls are small enough. However, under real working conditions, important variations of thermophysical properties can be expected.

- Gaining insight into the physics of natural convection flows in cavities and, in particular, into the influence of the thermophysical properties on the transition to turbulence in both hot and cold walls.

- Exploring the validity of different large-eddy simulation (LES) models for capturing both the transition to turbulence, heat transfer and fluid dynamics phenomena present in cavities. To do this, the results of different subgrid-scale models will be studied and compared with the results obtained by means of direct numerical simulations (DNS)

The computed data and the results obtained will be made available for the research community via their publication on the CTTC database.

1.3 Outline

The outline of this thesis is the following. The next Chapter is devoted to the assessment of the limits of the Oberbeck-Boussinesq approximation on the natural convection in a two-dimensional cavity by means of direct numerical resolutions. As it will be shown, and without loss of generality, the two-dimensional hypothesis can be a rather good approximation for isolating the effects of the variable thermophysical properties when the temperature gradient between the walls increases.

Having obtained the influence of the variable thermophysical properties for two-dimensional flow assumption in Chapter 2, the analysis is extended in Chapter 3 to the three-dimensionality of the observed effects. The role of vortex stretching mechanism associated with the variable thermophysical properties is assessed through the comparison of the results obtained by means of direct numerical simulations considering both Oberbeck-Boussinesq and non-Oberbeck-Boussinesq approaches.

Chapter 4 is devoted to the assessment of different subgrid-scale models for the simulation of tall differentially heated water-filled cavities. As it will be shown in the chapter, not only the influence of the model is important for capturing the location of the transition to turbulence, but also a proper selection of the numerical mesh plays an important role. The influence of different models on the heat transfer in the cavity will also be assessed by means of direct numerical simulations.

Finally, in Chapter 5, concluding remarks are provided. The ongoing research and future actions are described.

References

[1] Liu Yang, Haiyan Yan, and Joseph C. Lam. Thermal comfort and building energy consumption implications- A review. *Applied Energy*, 115:164–173, 2014.

[2] D. Faggembauu, M. Costa, M. Soria, and A. Oliva. Numerical analysis of the thermal behaviour of glazed ventilated facades in Mediterranean climates. Part I: Development and validation of a numerical model. *Solar Energy*, 75(3):217–228, 2003.

[3] E.M. Kleinbach, W.A. Beckman, and S.A. Klein. Performance study of one-dimensional models for stratified thermal storage tanks. *Solar Energy*, 50(2):155–166, 1993.

[4] F.X. Trias. Direct numerical simulation and regularization modelling of turbulent flows on loosely coupled parallel computers using symmetry-preserving discretizations. PhD thesis, Universitat Politècnica de Catalunya, 2006.

[5] X. Trias, M. Soria, D. Pérez-Segarra, and A. Oliva. Direct Numerical simulations of two and three dimensional turbulent natural convection flows in a differentially heated cavity of aspect ratio 4. *Journal of Fluid Mechanics*, 586:259–293, 2007.

[6] F. X. Trias, A. Gorobets, M. Soria, and A. Oliva. Direct numerical simulation of a differentially heated cavity of aspect ratio 4 with Rayleigh numbers up to 10^{11}. part i: Numerical methods and time-averaged flow. *International Journal of Heat and Mass Transfer*, 53(4):665 – 673, 2010.

[7] F.X. Trias, A. Gorobets, A. Oliva, and C.D. Pérez-Segarra. {DNS} and regularization modeling of a turbulent differentially heated cavity of aspect ratio 5. *International Journal of Heat and Mass Transfer*, 57(1):171 – 182, 2013.

[8] G.K. Batchelor. Heat transfer by free convection across a closed cavity between vertical boundaries at different temperatures. *Q. J Appl Math*, 12(3):209–233, 1954.

[9] Verzicco R. and R. Camussi. Numerical experiments on strongly turbulent thermal convection in a slender cylindrical cell. *Journal of Fluid Mechanics*, 477:19–49, 2003.

[10] Denis Funfschilling and Guenter Ahlers. Plume Motion and Large-Scale Circulation in a Cylindrical Rayleigh-Bénard Cell. *Physical Review Letters*, 92(19):1–4, May 2004.

[11] E. Brown and G. Ahlers. Large-scale circulation model for turbulent Rayleigh-Bénard convection. *Physical Reviews Letters*, 98(134501), 2007.

[12] G. Ahlers, S. Grossmann, and D. Lohse. Heat transfer and large scale dynamics in turbulent Rayleigh-Bénard convection. *Reviews of Modern Physics*, 81(2):503–537, 2009.

[13] D. G. Barhaghi and L. Davidson. Natural convection boundary layer in a 5:1 cavity. *Physics of Fluids*, 19(12):125106, 2007.

[14] K. Hanjalić. One-point closure models for buoyancy-driven turbulent flows. *Annual Review of Fluid Mechanics*, 34:321–347, 2002.

[15] X. Albets-Chico, A. Oliva, and C. D. Pérez-Segarra. Numerical experiments in turbulent natural convection using two-equation eddy-viscosity models. *Journal of Heat Transfer*, 130(7):072501, 2008.

[16] a. Omranian, T.J. Craft, and H. Iacovides. The computation of buoyant flows in differentially heated inclined cavities. *International Journal of Heat and Mass Transfer*, 77:1–16, 2014.

[17] Niranjan S. Ghaisas, Dinesh A. Shetty, and Steven H. Frankel. Large eddy simulation of thermal driven cavity: Evaluation of sub-grid scale models and flow physics. *International Journal of Heat and Mass Transfer*, 56(1-2):606–624, 2013.

[18] S. Xin and P. Le Quéré. Direct numerical simulations of two-dimensional chaotic natural convection in a differentially heated cavity of aspect ratio 4. *Journal of Fluid Mechanics*, 304:87–118, 1995.

[19] R.A.W.M. Henkes and P.Le Quéré. Three-dimensional transition of natural-convection flows. *Journal of Fluid Mechanics*, 319:281–303, 1996.

[20] P.Le Quéré and M. Behnia. From onset of unsteadiness to chaos in a differentially heated square cavity. *Journal of Fluid Mechanics*, 359:81–107, 1998.

[21] P. Le Quéré. Transition to unsteady natural convection in a tall water-filled cavity. *Physics of Fluids A*, 2(4):503–515, 1990.

[22] P. J. A. Janssen and R. A. W. M. Henkes. Influence of Prandtl number on instability mechanisms and transition in a differentially heated square cavity. *Journal of Fluid Mechanics*, 290:319–344., 1995.

[23] DD Gray and A. Giorgini. The validity of the Boussinesq approximation for liquids and gases. *International Journal of Heat and Mass Transfer*, 19:545–551, 1976.

[24] Guenter Ahlers, Eric Brown, Francisco Fontenele Araujo, Denis Funfschilling, Siegfried Grossmann, and Detlef Lohse. Non-Oberbeck-Boussinesq effects in strongly turbulent Rayleigh-B'enard convection. *Journal of Fluid Mechanics*, 569:409–445, 2006.

[25] K. Sugiyama, Enrico Calzavarini, Siegfried Grossmann, and D. Lohse. Non-Oberbeck-Boussinesq effects in two-dimensional Rayleigh-Bénard convection in glycerol. *Europhysics Letters (EPL)*, 80(3):34002, 2007.

[26] Guenter Ahlers, Enrico Calzavarini, F.F. Araujo, D. Funfschilling, Siegfried Grossmann, Detlef Lohse, and Kazuyasu Sugiyama. Non-Oberbeck-Boussinesq effects in turbulent thermal convection in ethane close to the critical point. *Physical Review E*, 77(4):046302, 2008.

Chapter 2

Limits of the Oberbeck-Boussinesq approximation in a tall differentially heated cavity filled with water

This chapter have been published as:

Kizildag, D., Rodríguez, I., Oliva, A., & Lehmkuhl, O. (2014). Limits of the Oberbeck-Boussinesq approximation in a tall differentially heated cavity filled with water. International Journal of Heat and Mass Transfer, 68, 489-499. doi:10.1016/j.ijheatmasstransfer.2013.09.046

Abstract.

The present work assesses the limits of the Oberbeck-Boussinesq (OB) approximation for the resolution of turbulent fluid flow and heat transfer inside a tall differentially heated cavity of aspect ratio $\Gamma = 6.67$ filled with water ($Pr = 3.27, Ra = 2.12 \times 10^{11}$). The cavity models the integrated solar collector-storage element installed on an advanced façade. The implications of the Oberbeck-Boussinesq approximation is submitted to investigation by means of direct numerical simulations (DNS) carried out for a wide range of temperature differences. Non-Oberbeck-Boussinesq (NOB) effects are found to be relevant, especially beyond the temperature difference of 30 $^{\circ}C$, in the estimation of heat transfer, stratification, and flow configuration.

2.1 Introduction

Natural convection flows in cavities have attracted the attention of many researchers due to their presence in many applications of industrial relevance, such as the air flow in buildings, heat transfer in solar collectors, nuclear reactors, among others. Substantial work has been devoted to two canonical configurations: i) a cavity heated from below; ii) a cavity heated from the sides. The first configuration is known as the Rayleigh-Bénard problem, where the gravitational vector is parallel to the thermal gradient. The latter case is commonly referred to as the differentially heated cavity (DHC) problem.

The present work focuses on the DHC configuration, which is characterized by a thermal gradient orthogonal to the gravitational field. Several contributions to understand the physics of this flow appeared in the literature along the last three decades. The vast majority of the presented work was related to air-filled cavities (Prandtl number $Pr \sim 0.71$) and, considering the so-called Oberbeck-Boussinesq (OB) approximation. This approximation, being more mathematical than physical, considers constant thermophysical properties of the fluid, except for the density in the gravitational term of the momentum equation. By means of this approximation, the exact governing equations are modified to derive more tractable equations. As indicated in the work of Gray & Giorgini [1], the employment of the OB approximation can be justified for a wide range of temperature differences, as the air-filled enclosures are concerned.

The earlier efforts to model this phenomena addressed mainly steady laminar two-dimensional flows [2]. Driven by the increased computational power, works on two- and three-dimensional transitional and turbulent flows gradually emerged in the last two decades, each time addressing more chaotic flows [3, 4, 5]. The accumulated knowledge shows that although the DHC configuration represents a simple geometry, the flow gets extremely complex for sufficiently large Rayleigh numbers (*Ra*), since it undergoes a gradual transition to a chaotic state beyond a critical *Ra* (see for instance Refs. [6, 7]). For high *Ra*, different regimes are expected to coexist within the enclosure: i) laminar flow in the upstream part of the vertical boundary layer and ii) turbulent flow at some location downstream in the vertical boundary layer [8, 9]. Furthermore, due to the flow regime established in the hot and cold walls, some level of stratification is expected at the mid height of the cavity. This stratification phenomenon taking place in the core has been studied for a wide range of aspect ratios [10]. There have been found controversies about the stratification measured experimentally and numerically, which can be attributed to thermal radiation effects [11]. For more details about flow configuration, scale analysis, and stability properties the reader is referred to Refs. [12, 13, 14].

For the DHC configuration, works conducted without OB approximation are relatively limited in number. Paolucci et al. [15] investigated numerically the transition

from laminar to turbulent flow in a two dimensional air filled cavity for different aspect ratios. Later, Paolucci [16] studied the two-dimensional turbulent natural convection in an air filled square cavity for $Ra = 10^{10}$. Both studies were conducted without OB approximation, although the density variations in these works were restricted to the values within the so-called OB limit. Suslov and Paolucci [17] studied the linear stability of the natural convection flow in a tall DHC under non-Oberbeck-Boussinesq (NOB) conditions, investigating the dependence of the critical Rayleigh number on the temperature difference. Their results showed that the instabilities can be controlled by a competition between the shear and buoyancy mechanisms. Later, Mlaouah et al. [18] studied the case of a square air-filled cavity by means of a low-Mach number approximation, indicating the difficulties in describing the transition behavior of the flow at higher Rayleigh numbers if the exact equations are not used. Recently, Szewc et al. [19] obtained steady laminar natural convection solutions for a square cavity of $Ra = 10^5$ by means of smoothed particle hydrodynamics method, comparing results with OB and general NOB formulations. They studied different sets of Gay-Lussac numbers including considerable departures from the so-called OB regime, pointing significant variations in velocity and temperature profiles with respect to the reference OB solution.

For the Rayleigh-Bénard configuration, many authors studied this flow without considering the OB approximation. These studies can serve as reference to understand the physics of the DHC problem, despite the expected differences due to the direction of the thermal gradient. The NOB effects in low Prandtl gasses were studied by Robinson and Chan [20], and by Madruga and Riecke [21]. For the case of liquids, NOB effects on the temperature profile and the Nusselt number were previously studied for water by Ahlers et al. [22]. Later, Sugiyama et al. [23] extended their study to glycerol. In these cases NOB effects are mainly due to variations of the viscosity with temperature. However, Ahlers et al. [24] also studied NOB effects caused by the strong dependence of the thermal expansion coefficient on the temperature for ethane near its critical point.

The present work is focused on a water-filled DHC configuration. When the working fluid is water, i.e. greater Prandtl numbers compared with air, obtaining solutions for the governing equations gets even more complicated since the boundary layer becomes thinner than for air at the same conditions. As a consequence, there is an increasing demand for excessively fine grids in space and time in order to capture the smallest scales of the turbulent flow. Additionally, in most applications using water under practical working conditions, the OB approximation has to be questioned. This approximation is valid if the fluid properties are weakly dependent on the temperature or the temperature difference within the walls are small enough. However, under real working conditions, important variations of thermophysical properties can be observed. This study aims at addressing situations which

are well out of the OB regime.

Due to the large computational resources required to compute three-dimensional (3D) simulations, being even more demanding for water-filled cavities, this work considers two-dimensional (2D) simulations. This hypothesis is expected to be adequate to study the validity of the OB approximation, and the conclusions are expected to be acceptable without the loss of generality. In fact, there are several studies which support this hypothesis in the natural convection flow within enclosures. Schmalzl et al. [25] studied the Rayleigh-Bénard flow by means of 2D and 3D simulations, concluding that both show similar characteristics in the flow structure and global quantities at high Prandtl numbers, while differing -even qualitatively- at Prandtl numbers smaller than unity. DeLuca et al. [26] showed for the OB Rayleigh-Bénard convection that the most important flow features can be well captured by 2D simulations. More recently, Sugiyama et al. [27] also performed 2D simulations for the Rayleigh-Bénard convection considering both OB approximation and NOB effects, showing that 2D approach reflects well the dynamics of the boundary layer and the behavior of the Nusselt numbers. Trias et al. [28] performed 2D and 3D simulations of a DHC of aspect ratio 4 for Ra up to 10^{10}, observing that 2D computations were in good agreement with 3D ones in terms of time-averaged structures and averaged local and overall Nusselt numbers. It is important to note that they pointed out significant deviations in second order turbulent statistics. Although 2D approximation, especially in the turbulent regions, may not be suitable to predict the actual flow structures, it must be borne in mind that the primary scope of this work is to shed more light on the NOB effects, studying qualitatively and quantitatively the influence of temperature difference when the conditions depart from the so-called OB regime. Under these circumstances, the 2D approximation can be considered less critical since NOB effects can be present in both 2D and 3D cases, and 2D simulations can be considered sufficient to capture the dynamics of the flow and particularly the influence of NOB effects.

This paper is organized as follows: in Section 2 the case is briefly described. Section 3 is devoted to the mathematical and numerical model. In Section 4 the validation of the numerical model is presented. The numerical results are discussed in Section 5, and finally the conclusions are given in Section 6.

2.2 Description of the case

The integrated solar collector-storage element to model is a two-dimensional cavity (see Figure 2.1) of width $W = 0.11m$, with two vertical isothermal walls of height $H = 0.735m$. Wall temperatures are set to T_h and T_c so that $T_m = (T_h + T_c)/2 = 52$ $^\circ C$. The adopted geometry has an aspect ratio of $\Gamma = 6.68$. The cavity has adiabatic end walls. No-slip boundary conditions are imposed at the walls, which are rigid

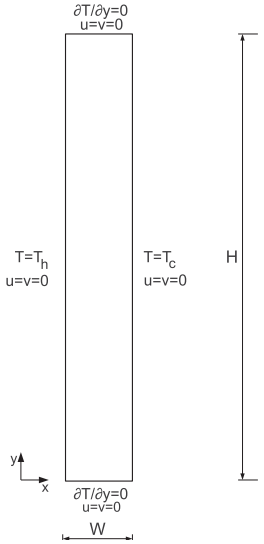

Figure 2.1: Geometry and boundary conditions

and impermeable.

This work aims at studying the relevance of the NOB effects in the DHC filled with water. For this reason a wide range of temperature differences ($\Delta T = T_h - T_c$ = 10, 20, 30, 40, 60 $^\circ C$) is chosen to compare both OB and NOB results obtained for the same mean Rayleigh and Prandtl numbers in order to shed light on qualitative and quantitative implications of NOB approximation.

In this paper, the OB case will be referred to as *BSQ*, while the reference to a particular NOB case will be done with the associated temperature difference, e.g. *NOB10*, *NOB20*, etc.

2.3 Mathematical and numerical model

In buoyancy driven flows a common approach is to consider constant thermophysical properties of the fluid, with the exception of the density variations that are only taken into account in the buoyancy forces, i.e., the so-called OB approximation. Thus, the temperature dependence of density in the buoyancy force is linearized as:

$$\rho(T) = \rho_m - \rho_m \beta_m (\mathbf{T} - T_m) \tag{2.1}$$

where ρ_m is the density, β_m is the thermal expansion coefficient ($\beta_m = -\rho_m^{-1}\partial\rho/\partial T|_{T_m}$) at the mean temperature $T_m = (T_h + T_c)/2$. These assumptions have several implications. First, continuity equation is treated in its incompressible form, neglecting acoustic phenomena, which in the case of liquids has no major implications. Furthermore, for liquids, deviations from the aforementioned hypothesis are mainly due to viscosity variations, as the viscosity strongly decreases with the temperature increase.

Assuming the OB approximation, the finite volume discretization of the incompressible Navier-Stokes and continuity equations on an arbitrary mesh can be written as:

$$\mathbf{M}\mathbf{u} = \mathbf{0} \tag{2.2}$$

$$\Omega\frac{\partial \mathbf{u}}{\partial t} + \mathbf{C}(\mathbf{u})\mathbf{u} + \nu\mathbf{D}\mathbf{u} + \Omega\rho^{-1}\mathbf{G}p + f = \mathbf{0} \tag{2.3}$$

$$\Omega\frac{\partial \mathbf{T}}{\partial t} + \mathbf{C}(\mathbf{u})\mathbf{T} + \alpha\mathbf{D}(\mathbf{T}) = \mathbf{0} \tag{2.4}$$

where $\mathbf{u} \in \mathbb{R}^{3n}$, $\mathbf{T} \in \mathbb{R}^n$ and $p \in \mathbb{R}^n$ are the velocity vector, temperature and pressure, respectively (here n applies for the total number of control volumes (CV) of the discretized domain), ν is the kinematic viscosity, α is the thermal diffusivity ($\alpha = k/\rho C_p$), k is the conductivity, and C_p is the specific heat. f is the body force $f = \beta(\mathbf{T} - T_m)\mathbf{g}$. Note that all the thermophysical properties are evaluated at T_m. Convective and diffusive operators in the momentum equation for the velocity field are given by $\mathbf{C}(\mathbf{u}) = (\mathbf{u}\cdot\nabla) \in \mathbb{R}^{3n\times 3n}$, $\mathbf{D} = \nabla^2 \in \mathbb{R}^{3n\times 3n}$ respectively. Gradient and divergence (of a vector) operators are given by $\mathbf{G} = \nabla \in \mathbb{R}^{3n\times 3n}$ and $\mathbf{M} = \nabla\cdot \in \mathbb{R}^{n\times 3n}$ respectively. $\Omega \in \mathbb{R}^n$ is a matrix with the volumes of the cells.

In our work when considering the NOB effects, the thermophysical properties of water are calculated following a temperature dependence:

$$\phi(T) = \Sigma_{n=0}^{N} a_n T^n \tag{2.5}$$

where ϕ is the thermophysical property (ρ, C_p, μ, k), T is the temperature in Kelvins, and the coefficients a_n of the equation 3.1 are given in Table 3.1.

Thus, equations 2.2 to 2.4 with variable thermophysical properties of incompressible fluid read:

$$\mathbf{M}\mathbf{u} = \mathbf{0} \tag{2.6}$$

$$\Omega\rho(T)\frac{\partial \mathbf{u}}{\partial t} + \mathbf{C}(\rho(T)\mathbf{u})\mathbf{u} + \mathbf{D}(\nu(T)\mathbf{u}) + \Omega\mathbf{G}p - \rho(T)\mathbf{g} = \mathbf{0} \tag{2.7}$$

$$\Omega\rho(T)C_p(T)\frac{\partial \mathbf{T}}{\partial t} + \mathbf{C}\left(C_p(T)\rho(T)\mathbf{u}\right)\mathbf{T} + \mathbf{D}\left(k(T)\mathbf{T}\right) = \mathbf{0} \tag{2.8}$$

n	ρ (kg/m^3)	C_p $(J/kg \cdot K)$	μ $(kg/m \cdot s)$	k (W/m)
0	8.49×10^{2}	2.28×10^{4}	1.94×10^{-1}	-2.98
1	1.29	-1.94×10^{2}	-2.19×10^{-3}	3.07×10^{-2}
2	-2.65×10^{-3}	7.52×10^{-1}	9.89×10^{-6}	-9.80×10^{-5}
3		-1.29×10^{-3}	-2.22×10^{-8}	1.43×10^{-7}
4		8.28×10^{-7}	2.46×10^{-11}	-8.21×10^{-11}
5			-1.09×10^{-14}	

Table 2.1: Coefficients a_n of the equation 3.1 to calculate the temperature dependent thermophysical properties of water.

Considering the reference scales for length, time, velocity, temperature and dynamic pressure as $L_{ref} = H$, $t_{ref} = (H^2/\alpha)Ra^{-0.5}$, $v_{ref} = (\alpha/H)Ra^{0.5}$, $\Delta T_{ref} = T_h - T_c$, $p_{ref} = \rho(\alpha/H^2)Ra$, respectively, OB thermal convection in the cavity is governed by the Rayleigh number $\left(Ra = g\beta\left(T_h - T_c\right)H^3Pr/\nu^2\right)$, Prandtl number $(Pr = \nu/\alpha)$, and height aspect ratio $\Gamma = H/W$. The problem under study is defined by $Pr = 3.27$, $Ra = 2.12 \times 10^{11}$, and $\Gamma = 6.67$ due to the particular geometry, mean temperature, and thermophysical properties of the present investigation.

The governing equations are discretized on a collocated unstructured grid arrangement by means of second-order conservative schemes [29]. Such discretization preserves the symmetry properties of the continuous differential operators, i.e., the conservation properties are held if, the convective term is discretized by a skew-symmetric operator and the diffusive term is approximated by a symmetric, positive-definite coefficient matrix. These properties ensure both stability and conservation of the global kinetic-energy balance on any grid. Energy transport is also discretized by means of a conservative scheme.

For the temporal discretization of the momentum equation, a two-step linear explicit scheme on a fractional-step method has been used, while for the pressure-gradient term an explicit first-order scheme has been employed [30]. This methodology has been previously used with accurate results for solving the flow over bluff-bodies with massive separation (see for instance [31, 32]), but also for the turbulent natural convection in enclosures [33, 34].

It might be argued that collocated meshes do not conserve kinetic energy when fractional step method is used due to the contribution of the pressure gradient term to the evolution of the kinetic energy [35, 36]. However, pressure errors have been proven to be of the order of $\mathcal{O}(\triangle x^2 \triangle t^2)$ [36]. Thus, in DNS the impact of such errors should be minimum due to the grid sizes and time-steps used.

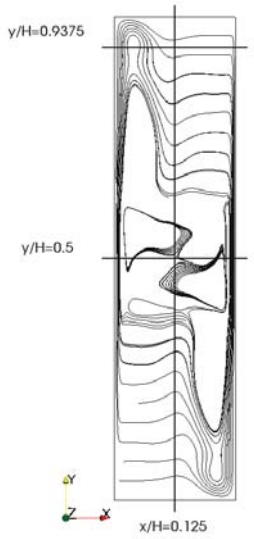

Figure 2.2: Locations in the cavity where computational results are compared.

2.4 Validation of the numerical model

The OB model is validated by means of a 2D differentially heated cavity case with $Ra = 10^{10}$, $Pr = 0.71$, and height aspect ratio $\Gamma = 4$ for which Trias et al. [28] presented two-dimensional DNS results considering OB approximation.

For validation purposes, a computational grid of 88201 CVs (193 $\times$ 457) is generated. The grid is uniform in the streamwise direction, while in the wall normal direction the following hyperbolic-tangent function is used:

$$x_i = \frac{W}{2}\left(1 + \frac{tanh\left[\gamma_x\left(2(i-1)/N_X - 1\right)\right]}{tanh\gamma_x}\right) \tag{2.9}$$

where x_i indicates the location of the west control volume face, γ_x is the mesh concentration factor and N_X is the number of CVs in the wall-normal direction. For the generated computational grid γ_x is 1.997. The numerical results obtained with this computational grid are compared with the results obtained by Trias et al. [28]. The comparison is carried out considering overall averaged Nusselt numbers, and first order statistics at different locations within the cavity.

The overall averaged Nusselt number calculated yielded 100.46, which is within a relative error of 0.14% with respect to the benchmark solution ($Nu = 100.60$), indi-

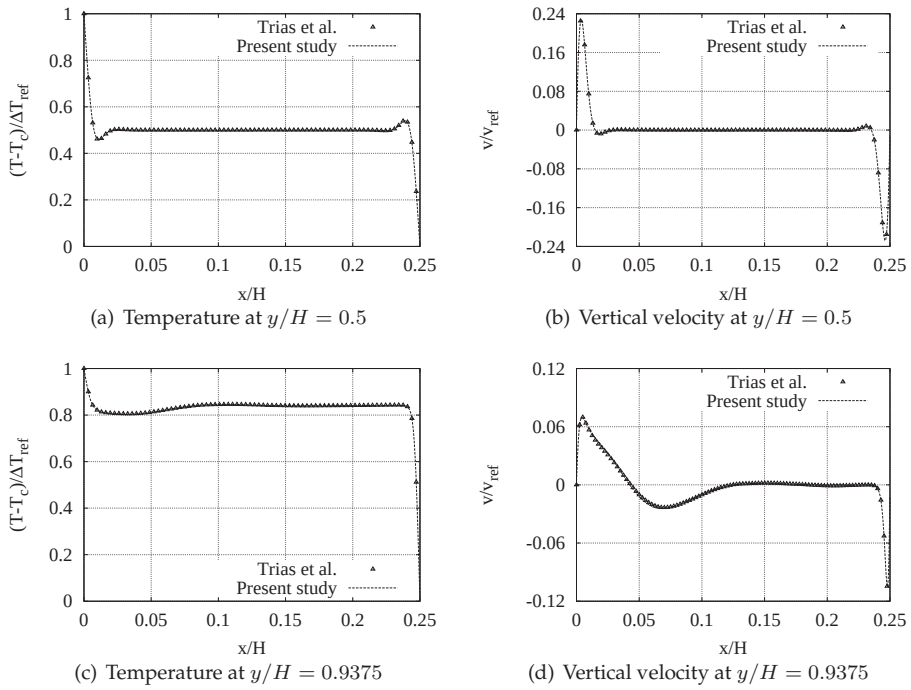

(a) Temperature at $y/H = 0.5$

(b) Vertical velocity at $y/H = 0.5$

(c) Temperature at $y/H = 0.9375$

(d) Vertical velocity at $y/H = 0.9375$

Figure 2.3: Validation of the numerical model. Comparison with DNS results from [28].

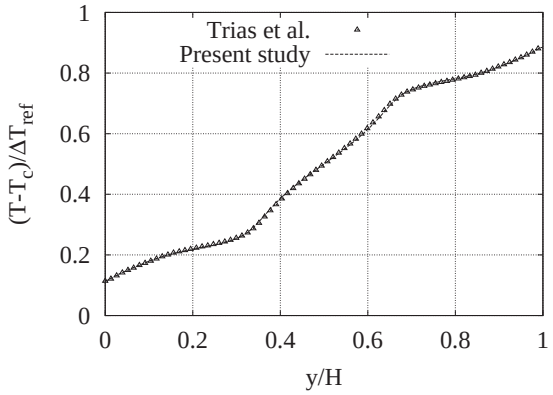

Figure 2.4: Temperature profile at $x/H = 0.125$. Comparison with DNS results from [28].

cating a satisfactory agreement, that can also be confirmed when the first order flow variables are compared at different locations of the cavity (see Figure 2.2). As can be seen in Figure 2.3, the velocity and temperature profiles are well reproduced, not only at the mid height of the cavity where the flow is laminar, but also at the top ($y/H = 9.9375$) where the flow is turbulent. Indeed, the agreement in the results is not limited to certain locations, but to the whole cavity as can be observed in Figure 2.4, where the vertical temperature profile along the cavity height is depicted. Owing to these results, it can be concluded that the current model is properly validated.

2.5 Numerical results

In this section, instantaneous and time-averaged results are presented after assessing the quality of the mesh resolutions. Although two-dimensional simulations may capture important flow features at more affordable costs (see [25, 26, 27, 28]), the turbulence can only be well predicted considering the three-dimensionality of the flow. However, the present investigation focuses on the limits of the OB approximation, for which the present simulations might be considered adequate without the loss of generality. Thus, the results are compared in detail to highlight the influence of the so-called NOB effects.

Mesh	N_X	N_Y	Δx_{min}	Δx_{max}	γ_x	Δy
I	177	913	1.36×10^{-4}	1.72×10^{-3}	1.952	1.09×10^{-3}
II	227	913	1.36×10^{-4}	1.24×10^{-3}	1.778	1.09×10^{-3}
III	227	1221	1.36×10^{-4}	1.24×10^{-3}	1.778	8.19×10^{-4}
IV	615	1405	5.44×10^{-5}	4.45×10^{-4}	1.715	7.12×10^{-4}

Table 2.2: Main parameters of the meshes used in the mesh resolution studies. N_X and N_Y are the number of CVs; Δx_{min} and Δx_{max} are the smallest and biggest wall-normal CV sizes, respectively; γ_x is the wall-normal mesh concentration factor; Δy is the streamwise CV size.

2.5.1 Mesh refinement studies

In order to capture all features of the flow, an adequate spatial discretization has to be performed. The viscous and thermal boundary layers at the isothermal confining walls should be well resolved, while, at the same time, the grid size at the bulk zone must be smaller than the smallest scales of the flow. An *a priori* estimate of the boundary layer has shown that for the studied mean Prandtl number, the thermal boundary layer is thinner than the viscous one as $\delta_t \sim H/Ra^{0.25}$ and $\delta_\nu \sim Pr^{0.5}\delta_t$ [12]. Four different meshes are generated attaining the aforementioned criteria to carry out extensive mesh refinement studies, being the finest mesh of 864075 CVs (615×1405). The meshes are uniform in the streamwise direction, while in the wall-normal direction CVs are spaced according to Equation 4.8. All the meshes guarantee sufficient CVs within the boundary layers. Details of the tested meshes are given in Table 2.2. Although not shown here for the sake of brevity, the main parameters of the flow are compared in detail for the tested meshes using OB model. Comparisons have shown good agreement for meshes III and IV, resulting in, for instance, relative differences of as low as 1.8% and 2.1% for overall averaged Nusselt number and time-averaged wall shear stress respectively. Considering these two meshes, first-order statistics are in fair good agreement, even though mesh III is more than 3 times coarser than mesh IV.

In order to further assess the quality of the mesh resolution used in the present computations, an *a posteriori* analysis comparing the actual mesh size h ($h \equiv (\Delta x \times \Delta y)^{1/2}$) with the theoretical smallest scales of the flow is carried out.

In Figure 2.5, the profile of the ratio h/L_d over the cavity height at three different positions ($x/H = 1/4\Gamma, 1/2\Gamma, 3/4\Gamma$) is given, where $L_d = \nu^{1/2}/\hat{\eta}^{1/6}$ is the enstrophy dissipation length scale, and $\hat{\eta}$ is the enstrophy dissipation rate. The vertical profiles are chosen so as to have representative values for the whole cavity, and the positions are selected at the mid width and in the vicinity of the hot and cold isothermal walls to account for different flow regimes in the cavity. As can be observed in the figure,

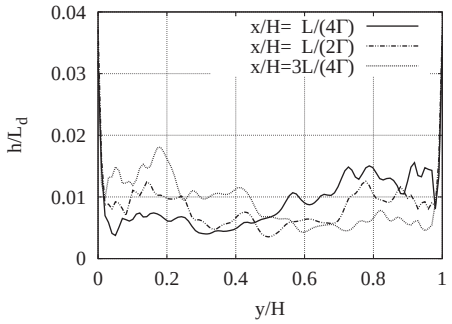

Figure 2.5: Ratio of h/L_d along vertical lines x=H/4Γ, H/2Γ, 3H/4Γ.

for the finest computational mesh (mesh *IV*) the grid size is of 1 to 2 orders of magnitude smaller than the reference length scale, which shows that the selected grid is more than adequate to solve the smallest scales of the flow.

2.5.2 Instantaneous flow

Instantaneous flow parameters might be useful for identifying the influence of the NOB effects when the temperature difference increases. In this regard, the instantaneous isotherms at $t/t_{ref} = 700$ are depicted for the studied cases in Figure 2.6. In the figure, 28 homogeneously spaced isothermal contour lines between $\Phi = (T - T_c)/(T_h - T_c) = 0$ and $\Phi = 1$ are plotted. In all the flows, quasi-horizontal isothermal contour lines are formed except for the regions in the vicinity of the vertical boundary layers, where higher temperature gradients are observed. Instabilities appear at some stage downstream along the hot and cold horizontal walls, while their locations and intensities differ depending on the case. Specially for the *NOB40* and *NOB60* cases, the flow behavior is substantially different.

The OB solution is symmetric around the center of the cavity as can be seen in Figure 2.6(a), where isotherms are placed symmetrically around the central isotherm. For the *NOB10*, *NOB20*, and *NOB30* cases the symmetry is only slightly broken, which can be observed especially at the core of the cavity where warmer regions extend partially over the neighboring colder ones. In the *NOB40* and *NOB60* cases (Figures 2.6(e)-2.6(f)), however, the symmetry no longer exists. For instance, in the *NOB40* case, the region containing the mean temperature of the cavity (T_m) shifts upwards, resulting in colder cavity center. In both the hot and cold walls the instabilities get intensified. In between these instabilities that indicate transition along the hot and cold walls, 6 regions of isotherms shrink to form a highly stratified zone.

(a) (b) (c) (d) (e) (f)

Figure 2.6: Instantaneous temperature isotherms at $t/t_{ref} = 700$ for (a) BSQ, (b) NOB10, (c) NOB20, (d) NOB30, (e) NOB40, and (f) NOB60.

(a) (b) (c) (d) (e) (f)

Figure 2.7: Instantaneous magnitude of the velocity vector at $t/t_{ref} = 700$ for (a) *BSQ*, (b) *NOB10*, (c) *NOB20*, (d) *NOB30*, (e) *NOB40*, and (f) *NOB60*.

This zone is bounded from the top and bottom by a large region of isothermal flow, which is a sign of enhanced horizontal motion. In view of the observed contrast with the OB solution, beyond the temperature difference of 30 $^{\circ}C$ the NOB effects are found decisive. These effects can be attributed to the behavior of the vertical boundary layers and particularly their interaction.

The magnitude of the instantaneous velocity vector is plotted in Figure 2.7. It can be observed that when the NOB effects are considered, the instabilities along the cold wall occur slightly upstream, thus extending the so-called turbulent zone with respect to the hot wall. This is especially true for the temperature differences of 40 and 60 $^{\circ}C$, where a pronounced flow separation is observed. Thus, the outcome from the instantaneous temperature isotherms on the validity of the OB approximation is confirmed.

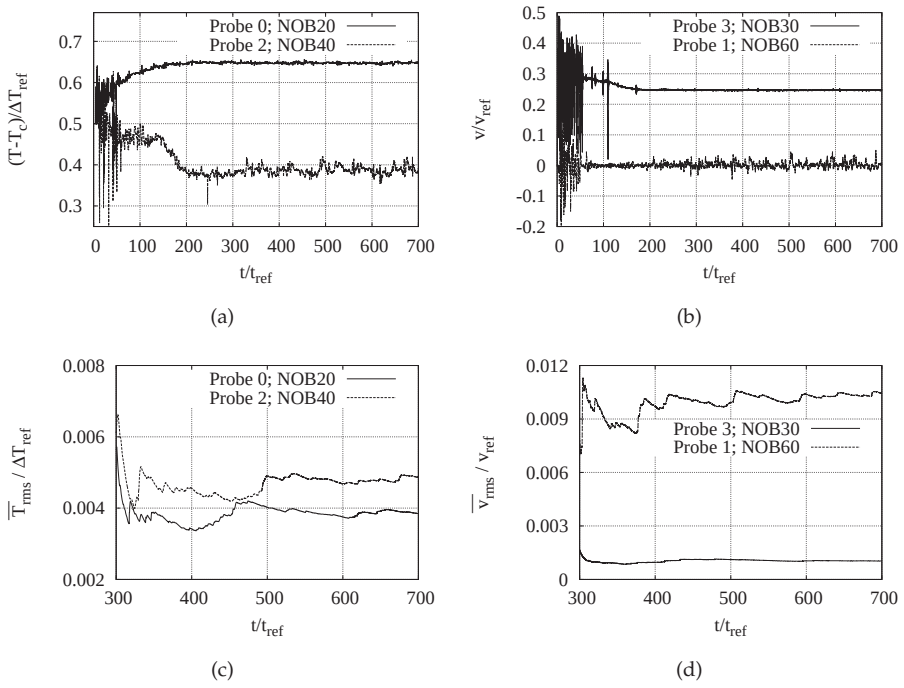

Figure 2.8: (a) Transient temperature, (b) vertical velocity, (c) accumulated temperature fluctuations, (d) accumulated velocity fluctuations, at different probe positions considering different cases. Probe 0 (1/2Γ,0.9); Probe 1 (1/2Γ,0.7); Probe 2 (1/2Γ,0.5); Probe 3 (0.002,0.5).

2.5.3 Mean flow parameters

In order to assure that time-independent solution is obtained, numerical probes are placed in key locations. In Figure 2.8, the time evolution of temperature and streamwise velocity component, and their accumulated fluctuations are plotted for different cases at some of these locations. Although not shown here for the sake of brevity, 19 probes are placed in representative locations to check the corresponding time scales of the flow. In the light of the gathered information from all the probes, time integration started from $t/t_{ref} = 300$. In order to have converged statistics, the flow has then been integrated over a period of 400 time units, which is shown to be a good compromise between accuracy and integration time as the accumulated fluctuations of the variables asymptotically approach to a certain mean value (see Figures 2.8(c)

and 2.8(d)).

In Table 2.3, the maximum and minimum values of the streamwise velocity component, i.e. v_{max} and v_{min}, are summarized together with their locations for each of the studied cases. Note that for the *BSQ*, the maximum and minimum velocities are equal in absolute value, being symmetric the locations where these extrema are encountered. For the NOB cases, neither the magnitudes are equal nor their locations are symmetric. However, confirming the observations from the instantaneous flow, the absolute value of the maximum (minimum) velocity increases (diminishes) only slightly (within 5 % with respect to the *BSQ*) as the temperature difference increases up to the *NOB30* case. For the *NOB40* case, an abrupt increment in the velocities of both boundary layers is observed (approximately 21 % and 6 % in maximum and minimum values, respectively). The generalized trend in the NOB effects are followed with a further increase in the temperature difference (i.e. *NOB60*), without essential differences with respect to the *NOB40* case. In all the NOB cases, the velocities in the vicinity of the cold wall are smaller in absolute terms than their counterparts in the vicinity of the hot wall, indicating thicker boundary layer. Note that the relative change in the vertical velocity (i.e. $\frac{|v_{max}|-|v_{min}|}{|v_{max}|}$) increases with the temperature difference.

In Figure 2.9, streamwise velocity profiles in the vicinity of the hot wall are plotted for different cavity heights ($y/H = 0.3, 0.5, 0.65, 0.8$). At $y/H = 0.3$, the maximum velocity only slightly increases with the temperature difference. However, at the mid height of the cavity a significant departure from the OB solution is observed beyond the temperature difference of 30 $^{\circ}C$. Further downstream, at $y/H = 0.65$, the *BSQ*, *NOB10*, *NOB20*, and *NOB30* cases have indistinguishable behavior, while for the *NOB40* case, a major deceleration is observed. The vertical velocity component reduces more than 50% due to the flow separation taking place. Finally, at $y/H = 0.8$, the flow gets more chaotic thus registering smaller streamwise velocity components. This is especially true for the *NOB40* and *NOB60* cases where the vertical velocity component is approximately 15% lower than in the *BSQ* solution.

In Figure 2.10, streamwise velocity component along the cold wall is plotted at equivalent locations. The loss of symmetry is observed as early as $y/H = 0.7$. At mid height of the cavity, the behavior of the *NOB40* and *NOB60* cases are totally different, as instabilities occur upstream than in hot wall. This can also be anticipated in Table 2.3, where in the cold wall the absolute maximum values are reached well before mid height. As the flow goes downstream, similar effects as in the hot wall are observed, although the NOB effects break totally the symmetry.

In view of the present analysis on the velocity field, the temperature difference of 30 $^{\circ}C$ appears as a limit beyond which the NOB effects become dominant.

In Table 4.3, overall averaged Nusselt numbers are given together with the location where transition occurs in hot and cold walls. The location of the transition is de-

	v_{max}/v_{ref}	x^*_{max}	y^*_{max}	v_{min}/v_{ref}	x^*_{min}	y^*_{min}
BSQ	0.245	1.87×10^{-3}	4.65×10^{-1}	-0.245	1.87×10^{-3}	4.65×10^{-1}
NOB10	0.247	1.80×10^{-3}	4.91×10^{-1}	-0.241	1.94×10^{-3}	4.37×10^{-1}
NOB20	0.251	1.80×10^{-3}	5.13×10^{-1}	-0.236	1.94×10^{-3}	4.12×10^{-1}
NOB30	0.254	1.72×10^{-3}	5.37×10^{-1}	-0.234	2.02×10^{-3}	3.87×10^{-1}
NOB40	0.297	1.72×10^{-3}	5.30×10^{-1}	-0.260	2.17×10^{-3}	3.91×10^{-1}
NOB60	0.308	1.65×10^{-3}	5.60×10^{-1}	-0.254	2.24×10^{-3}	3.62×10^{-1}

Table 2.3: Time-averaged maximum and minimum vertical velocities, v_{max}/v_{ref} and v_{min}/v_{ref} respectively, and their locations. x^*_{max}, and x^*_{min} are the wall-normal distances from hot and cold wall respectively. y^*_{max} and y^*_{min} are the vertical distances from the upstream adiabatic horizontal wall, i.e. from the bottom and the top of the cavity respectively.

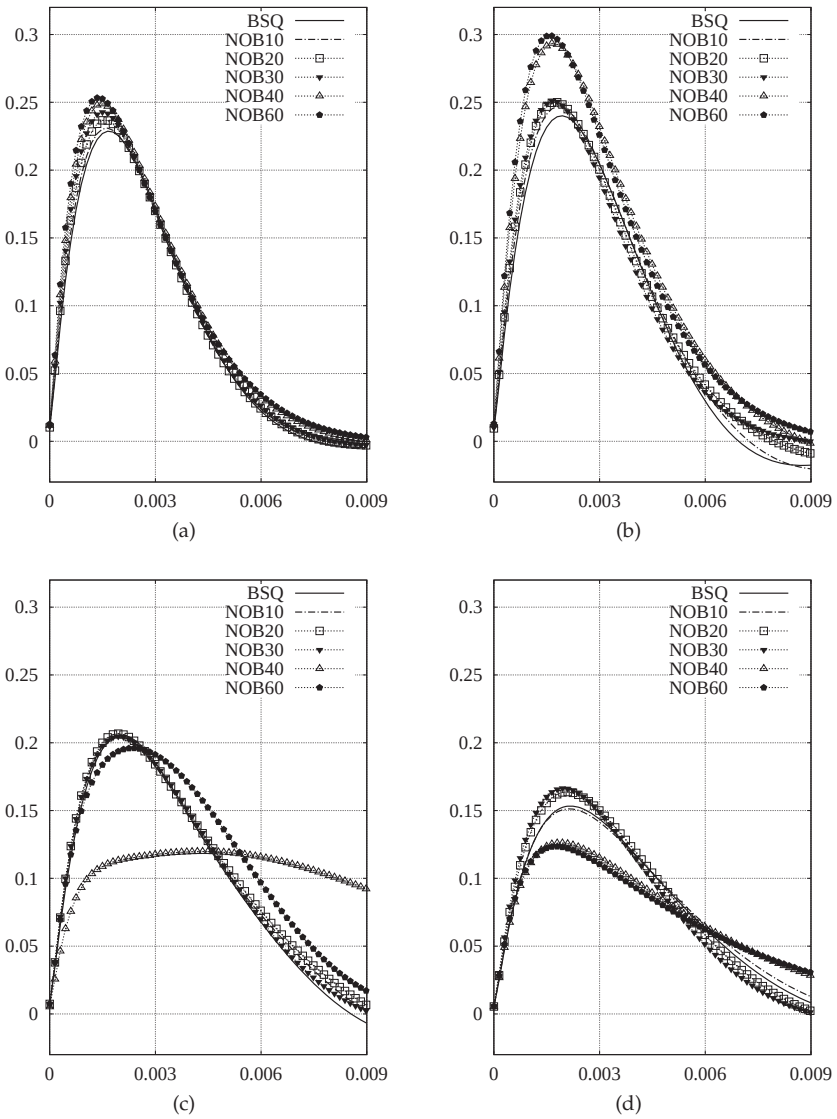

Figure 2.9: Streamwise velocity profile v/v_{ref} in the vicinity of the hot wall at different locations. X-axis corresponds to normal distance to the hot wall. (a) y/H=0.3 (b) y/H=0.5 (c) y/H=0.65 (d) y/H=0.8.

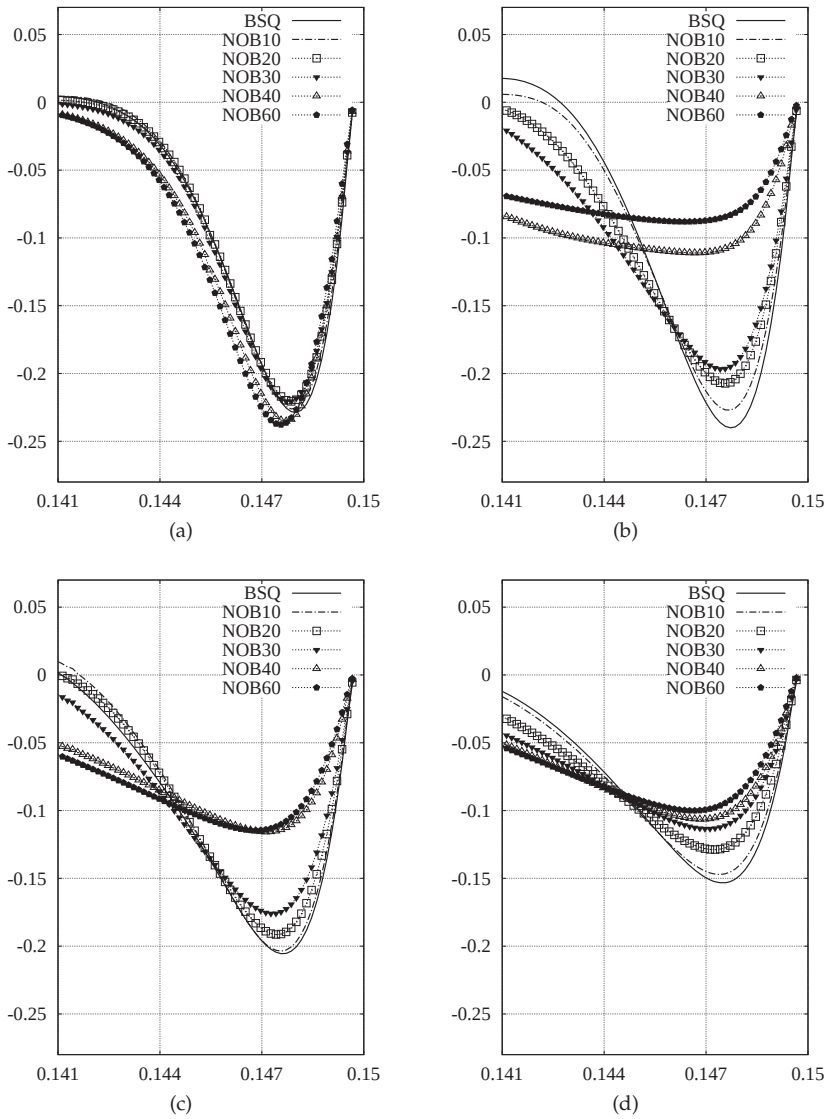

Figure 2.10: Streamwise velocity profile v/v_{ref} in the vicinity of the cold wall at different locations. X-axis corresponds to normal distance to the hot wall. (a) y/H=0.7 (b) y/H=0.5 (c) y/H=0.35 (d) y/H=0.2.

	$\overline{Nu}$	y_{tr}^{hot}/H	y_{tr}^{cold}/H
BSQ	231.18	0.56	0.56
NOB10	231.85	0.59	0.53
NOB20	232.23	0.61	0.50
NOB30	233.92	0.64	0.48
NOB40	251.07	0.66	0.50
NOB60	248.85	0.69	0.47

Table 2.4: Overall averaged Nusselt numbers and transition point at hot and cold wall. y_{tr}^{hot}/H and y_{tr}^{cold}/H are the vertical distance from the bottom and the top of the cavity, respectively.

fined as the position where local $\overline{Nu_{rms}}$ peaks. In order to clarify the adopted criterion, the local $\overline{Nu_{rms}}$ distribution in the hot and cold walls are plotted in Figure 2.11. Note that the figure is not to scale, and the graphs are shifted in y-direction to expose comparatively the transition to turbulence locations along hot and cold walls for the studied cases. However, the relative intensities of each peak value with respect to their upstream quasi-constant values are scaled. For the *NOB40* and *NOB60* cases, there is one large peak value unlike the lower temperature difference cases, which have a secondary broadband peak occurring downstream before reaching the horizontal boundary. The transition locations presented in Table 4.3 are consistent with the selected criterion. It should be pointed out that for the *NOB40* and *NOB60* cases, a small plateau prior to the $\overline{Nu_{rms}}$ peak is observed. In fact, in these two cases, transition to turbulence starts to occur slightly upstream the location where $\overline{Nu_{rms}}$ peaks. The analysis of the local $\overline{Nu_{rms}}$ reveals the major influence of the NOB effects beyond the temperature difference of 30 $^{\circ}C$. For lower temperature differences, the NOB effects are manifest in the form of a slight loss of symmetry.

In order to further highlight the NOB effects, local average Nusselt numbers in the cold wall are plotted in Figure 4.8. At lower temperature differences, NOB effects are not dominant in heat transfer. The minor increment of the order of 1 % in overall averaged Nusselt number can be attributed to the upstream transition in the cold wall. Beyond 30 $^{\circ}C$ of temperature difference, the NOB effects cause a visible enhancement in heat transfer. Note that if these are not considered, the overall averaged Nusselt number can be underestimated by about 8%.

Thermal behavior within the cavity is analyzed at the vertical profile in the half width ($x/H = 1/2\Gamma$) location in Figure 2.13. The stratification region occurs symmetrically at the center of the cavity for the BSQ case, being the non-dimensional stratification number 0.97 at this location. Note that when the NOB effects are considered, a slight upward shift in the location of the stratification region is observed up to $\Delta T = 30\ ^{\circ}C$. At higher temperature differences, these effects are not only re-

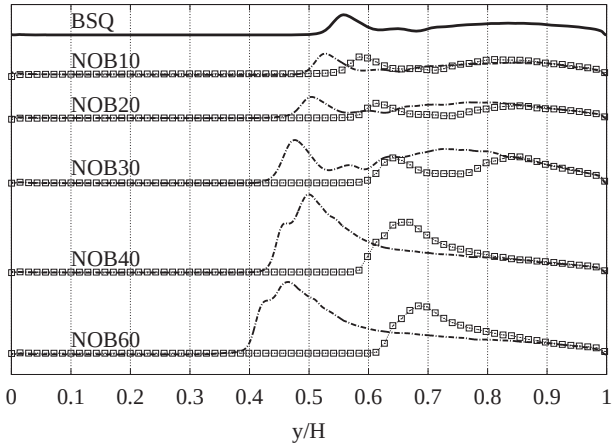

Figure 2.11: Local $\overline{Nu_{rms}}$ from the leading edge. Squares (hot wall); dashed line (cold wall).

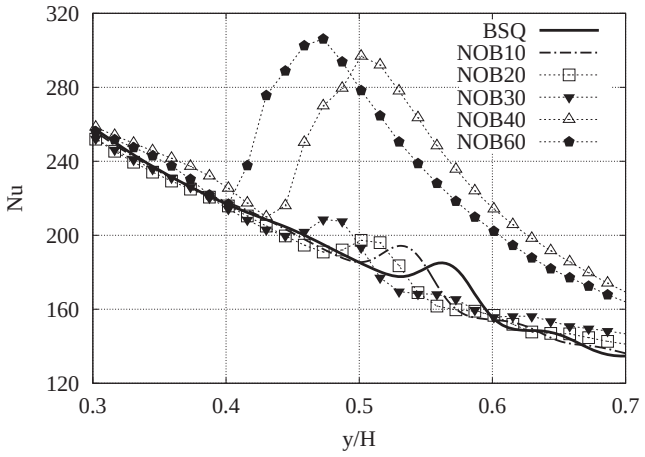

Figure 2.12: Local average Nusselt numbers along the cold wall.

CASE	y_p/H	stratification peak	Δy_{core}
BSQ	0.46	1.25	0.08
NOB10	0.49	1.27	0.08
NOB20	0.51	1.22	0.08
NOB30	0.54	1.29	0.07
NOB40	0.56	2.79	0.02
NOB60	0.59	2.90	0.02

Table 2.5: Parameters of the stratification number for the studied cases.

inforced as major departure of the stratification region from the center of the cavity, but also the corresponding stratification number undergoes a major increment. This can be better observed in Figure 2.13(c) where the stratification number profiles of the tested cases are plotted. In the literature, the stratification number is reported at the center of the cavity for DHC flows. When the symmetry is broken due to the NOB effects, this approach can be misleading. As an alternative, the stratification region can be defined as the one in between the two local stratification peak locations. Accordingly, the stratification peak value can be reported. This is summarized in Table 2.5, where y_p is the location of the stratification peak, and Δy_{core} is the size of the stratification region in the streamwise direction. Note that for the *NOB40* and *NOB60* cases, Δy_{core} is calculated using the minimum location of the second derivative of temperature, since only one stratification peak is observed. It can be concluded that if the NOB effects are not accounted for, the thermal stratification in the cavity can be strongly underestimated beyond the temperature difference of 30 $^{\circ}C$.

In Figure 2.14, the dimensionless time-averaged wall shear stress is presented for the studied cases. In accordance with the previous indicators, the sudden decrease in the wall shear stress for the *NOB40* and *NOB60* cases certifies a remarkable thickening of the boundary layer. This is not observed in the lower temperature difference cases, where the reduction in the shear stress occurs in a more gradual manner.

2.6 Conclusions

The relevance of the NOB effects in a tall two-dimensional DHC cavity filled with water at $Ra = 2.12 \times 10^{11}$, $Pr = 3.27$, and $\Gamma = 6.67$ has been submitted to investigation. A second-order symmetry-preserving formulation for solving the governing equations has been used. The numerical model has been validated by means of the comparison with two-dimensional direct numerical simulations from the literature for a differentially heated cavity of aspect ratio 4. NOB effects have been studied up to a temperature difference of 60 $^{\circ}C$. Time-averaged flow parameters and represen-

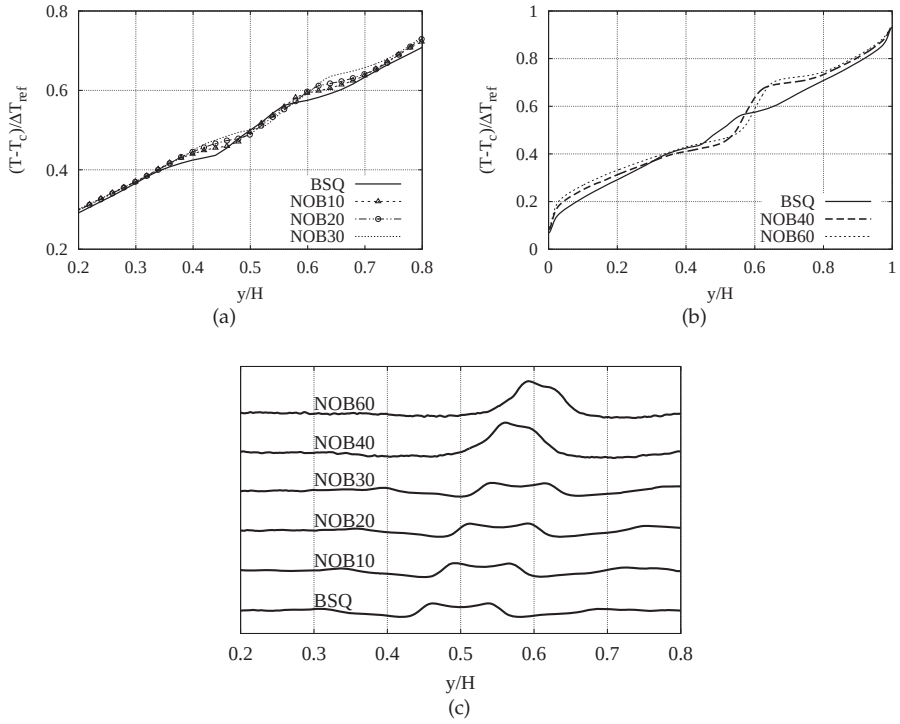

Figure 2.13: Comparative temperature and stratification profiles at ($x = 1/2\Gamma$) location. (a) temperature for BSQ, NOB10, NOB20, NOB30; (b) temperature for BSQ, NOB40, NOB60; (c) stratification number. Stratification plots are separated by 3 vertical stratification units for the comparison of the peak locations.

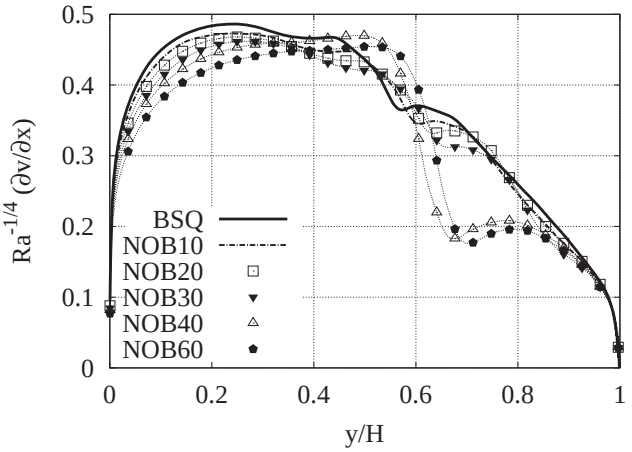

Figure 2.14: Dimensionless time-averaged wall shear stress at the hot wall scaled by $Ra^{-1/4}$ for the tested cases.

tative instantaneous fields have been presented. The numerical results reveal that up to the temperature difference of 30 $^{\circ}C$, OB solution can estimate the heat transfer with about 1% error, although the loss of symmetry of the flow is certified even for a temperature difference of 10 $^{\circ}C$.

Beyond the temperature difference of 30 $^{\circ}C$, a substantially different flow configuration is observed with respect to the OB solution, affecting the heat transfer and thermal stratification. The boundary layers at hot and cold isothermal confining walls behave differently, such that the instabilities move downstream along the hot wall and upstream along the cold wall. Due to the upward shift in both boundary layers, the stratification region changes, resulting in higher stratification numbers. For these cases, the interaction between the two boundary layers results in a more complex flow, where neglecting the NOB effects may lead to erroneous estimations of the phenomena taking place.

References

[1] D. Gray, A. Giorgini, The validity of the Boussinesq approximation for liquids and gases, International Journal of Heat and Mass Transfer 19 (1976) 545–551.

[2] G. De Vahl Davis, Natural Convection of Air in a Square Cavity: a Benchmark Numerical Solution, International Journal for Numerical Methods in Fluids 3

(1983) 249–264.

[3] R. Henkes, F. van Der Vlugt, C. Hoogendoorn, Natural convection flow in a square cavity calculated with low Reynolds-number turbulence models, International Journal of Heat and Mass Transfer 34 (1991) 377–388.

[4] T. Fusegi, J. M. Hyun, K. Kuwahara, B. Farouk, A numerical study of three-dimensional natural convection in a differentially heated cubical enclosure, International Journal of Heat and Fluid Flow 34 (6) (1991) 1543–1557.

[5] R. J. A. Janssen, R. A. W. M. Henkes, C. J. Hoogendorn, Transition to Time-Periodicity of a Natural-Convection Flow in a 3-D Differentially Heated Cavity, International Journal of Heat and Mass Transfer 36 (11) (1993) 2927–2940.

[6] S. Xin, P. L. Queré, Direct numerical simulations of two-dimensional chaotic natural convection in a differentially heated cavity of aspect ratio 4, Journal of Fluid Mechanics 304 (1995) 87–118.

[7] P. Quere, M. Behnia, From onset of unsteadiness to chaos in a differentially heated square cavity, Journal of Fluid Mechanics 359 (1998) 81–107.

[8] D. G. Barhaghi, L. Davidson, Natural convection boundary layer in a 5:1 cavity, Physics of Fluids 19 (12) (2007) 125106–125106.

[9] F. X. Trias, A. Gorobets, M. Soria, A. Oliva, Direct numerical simulation of a differentially heated cavity of aspect ratio 4 with Rayleigh numbers up to 10^{11} Part II: Heat transfer and flow dynamics, International Journal of Heat and Mass Transfer 53 (1) (2010) 674–683.

[10] J. Salat, S. Xin, P. Joubert, A. Sergent, F. Penot, P. Le Quere, Experimental and numerical investigation of turbulent natural convection in large air-filled cavity, International Journal of Heat and Fluid Flow 25 (2004) 824–832.

[11] F. X. Trias, A. Gorobets, M. Soria, A. Oliva, Direct numerical simulation of a differentially heated cavity of aspect ratio 4 with Rayleigh numbers up to 10^{11} Part I: Numerical methods and time-averaged flow, International Journal of Heat and Mass Transfer 53 (1) (2010) 665–673.

[12] J. Patterson, J. Imberger, Unsteady natural convection in a rectangular cavity, Journal of Fluid Mechanics 100 (1) (1980) 65–86.

[13] R. Janssen, S. Armfield, Stability properties of the vertical boundary layers in differentially heated cavities, International Journal of Heat and Fluid Flow 17 (6) (1996) 547–556.

[14] M. Farhangnia, S. Biringen, L. J. Peltier, Numerical simulation of two-dimensional buoyancy-driven turbulence in a tall rectangular cavity, International Journal for Numerical Methods in Fluids 23 (1996) 1311–1326.

[15] S. Paolucci, D. Chenoweth, Transition to chaos in a differentially heated vertical cavity, Journal of Fluid Mechanics 201 (1989) 379–410.

[16] S. Paolucci, Direct numerical simulation of two-dimensional turbulent natural convection in an enclosed cavity, Journal of Fluid Mechanics 215 (1990) 229–262.

[17] S. Suslov, S. Paolucci, Stability of natural convection flow in a tall vertical enclosure under non-Boussinesq conditions, International Journal of Heat and Mass Transfer 38 (12) (1995) 2143–2157.

[18] H. Mlaouah, T. Tsuji, Y. Nagano, A study of non-Boussinesq effect on transition of thermally induced flow in a square cavity, International Journal of Heat and Fluid Flow 18 (1) (1997) 100–106.

[19] S. Szewc, J. Pozorski, A. Taniere, Modeling of natural convection with Smoothed Particle Hydrodynamics: Non-Boussinesq formulation, International Journal of Heat and Mass Transfer 54 (2011) 4807–4816.

[20] F. Robinson, K. Chan, Non-Boussinesq simulations of Rayleigh-Benard convection in a perfect gas, Physics of Fluids 16 (5) (2004) 1321.

[21] S. Madruga, H. Riecke, Non-Boussinesq convection at low Prandtl numbers: Hexagons and spiral defect chaos, Physical Review E 75 (2007) 026210.

[22] G. Ahlers, E. Brown, F. F. Araujo, D. Funfschilling, S. Grossmann, D. Lohse, Non-Oberbeck-Boussinesq effects in strongly turbulent Rayleigh-Bénard convection, Journal of Fluid Mechanics 569 (2006) 409–445.

[23] K. Sugiyama, E. Calzavarini, S. Grossmann, D. Lohse, Non-Oberbeck-Boussinesq effects in two-dimensional Rayleigh-Bénard convection in glycerol, Europhysics Letters (EPL) 80 (3) (2007) 34002.

[24] G. Ahlers, E. Calzavarini, F. Araujo, D. Funfschilling, S. Grossmann, D. Lohse, K. Sugiyama, Non-Oberbeck-Boussinesq effects in turbulent thermal convection in ethane close to the critical point, Physical Review E 77 (4) (2008) 046302.

[25] J. Schmalzl, M. Breuer, U. Hansen, On the validity of two-dimensional numerical approaches to time-dependent thermal convection, Europhys. Lett. 67 (3) (2004) 390–396.

[26] E. DeLuca, J. Werne, R. Rosner, F. Cattaneo, Numerical simulations of soft and hard turbulence: preliminary results for two-dimensional convection, Phys. Rev. Lett. 64 (20) (1990) 2370–2373.

[27] K. Sugiyama, E. Calzavarini, S. Grossmann, D. Lohse, Flow organization in two-dimensional non-Oberbeck-Boussinesq Rayleigh-Bénard convection in water, Journal of Fluid Mechanics 637 (2009) 105–135.

[28] F. X. Trias, M. Soria, C. D. Pérez-Segarra, A. Oliva, Direct Numerical simulations of two and three dimensional turbulent natural convection flows in a differentialy heated cavity of aspect ratio 4, Journal of Fluid Mechanics 586 (2007) 259–293.

[29] R. W. C. P. Verstappen, A. E. P. Veldman, Symmetry-Preserving Discretization of Turbulent Flow, Journal of Computational Physics 187 (2003) 343–368.

[30] F. X. Trias, O. Lehmkuhl, A self-adaptive strategy for the time integration of navier-stokes equations, Numerical Heat Transfer. Part B 60 (2) (2011) 116–134.

[31] I. Rodríguez, R. Borrell, O. Lehmkuhl, C. D. Pérez-Segarra, A. Oliva, Direct Numerical Simulation of the Flow Over a Sphere at Re = 3700, Journal of Fluids Mechanics 679 (2011) 263–287.

[32] I. Rodríguez, O. Lehmkuhl, R. Borrell, C. D. Pérez-Segarra, A. Oliva, Low-frequency variations in the wake of a circular cylinder at $Re = 3900$, in: Proceedings of the 13th European Turbulence Conference, 2011.

[33] D. Kizildag, J. Ventosa, I. Rodriguez, A. Oliva, Non-Oberbeck-Boussinesq natural convection in a tall differentially heated cavity, in: Proceedings of the Fifth European Conference on Computational Fluid Dynamics ECCOMAS CFD 2010, 2010, pp. 1–13.

[34] I. Rodríguez, O. Lehmkuhl, R. Borrell, C. D. Perez-Segarra, On DNS and LES of natural convection of wall-confined flows: Rayleigh-Benard convection, in: H. Kuerten, B. Geurts, V. Armenio, J. Fröhlich (Eds.), Direct and Large-Eddy Simulation VIII (ERCOFTAC Series), Springer, 2011, pp. 389–394.

[35] Y. Morinishi, T. Lund, O. Vasilyev, P. Moin, Fully conservative higher order finite difference schemes for incompressible flow, Journal of Computational Physics 143 (1) (1998) 90–124.

[36] F. Felten, T. Lund, Kinetic energy conservation issues associated with the collocated mesh scheme for incompressible flow, Journal of Computational Physics 215 (2) (2006) 465–484.

Chapter 3

Non-Oberbeck-Boussinesq effects in a tall turbulent water-filled differentially heated cavity by means of direct numerical simulation

The results presented in this chapter have been partly published as:

Kizildag, D. and Rodríguez, I., Trias, F. X. & Oliva, A. (2014). Direct and large eddy simulations of non-Oberbeck-Boussinesq effects in a turbulent tall water-filled differentially heated cavity. 11th World Congress on Computational Mechanics, WCCM 2014, 5th European Conference on Computational Mechanics, ECCM 2014 and 6th European Conference on Computational Fluid Dynamics, ECFD 2014 pp. 5689-5697

Kizildag, D., Rodríguez, I., Trias, F. X., Oliva, A., & Pérez-Segarra, C. D. (2015). Non-Oberbeck-Boussinesq effects in a turbulent tall water-filled differentially heated cavity. In Proceedings of the International Symposium Turbulence, Heat and Mass Transfer 8, by K. Hanjalić, T. Miyauchi, D. Borello, M. Hadžiabdić and P. Venturini, Begel House Inc.

Abstract.

The present work studies the non-Oberbeck-Boussinesq effects in a tall water-filled (Prandtl number $Pr = 3.41$, Rayleigh number $Ra = 3 \times 10^{11}$) differentially heated cavity of aspect ratio

$\Gamma = 10$ by means of direct numerical simulation. The obtained results reveal significant Non-Oberbeck-Boussinesq effects for this configuration, due mainly to the dissimilar flow behavior in the vertical boundary layers. The results have revealed that transition to turbulence in the hot boundary layer shifts towards the top of the cavity (with respect the Oberberck-Boussinesq case), whereas in the cold boundary layer transition to turbulence is earlier triggered. This has been shown to be a consequence of the initial heating of the cavity due to favorable heat transfer properties in the hot wall boundary layer, which results in warmer upper cavity. As time advances, due to the influence of the stratified flow feeding the hot and cold boundary layers, the strength of the boundary layer gradually decreases and increases in the hot and cold boundary layers, respectively. When a balance is attained between these two boundary layers, the cold wall boundary is found at a higher equivalent Rayleigh number, justifying its premature transition. Accordingly, the early transitioning cold wall boundary layer is considerably thicker, and interacts actively with the hot wall boundary layer, causing vertical oscillations in the transition to turbulent locations on both boundary layers. This interaction is also responsible for the degradation of the already shifted stratification zone. This effect is not captured by means of two-dimensional simulations. As for the heat transfer, unlike the previous investigations, the Non-Oberbeck-Boussinesq effects do not necessarily enhance the heat transfer, as Oberbeck-Boussinesq solution is observed to overestimate the Nusselt number by about 3 %.

3.1 Introduction

The differentially heated cavity (DHC) flow has been extensively addressed by the scientific community in numerous numerical and experimental works carried out in the last three decades. This flow configuration is attractive due to its potential to model many applications of industrial relevance, such as solar thermal energy equipment, electronic devices, advanced building facades, etc. Although the first efforts were limited to steady laminar two-dimensional cases due to the lack of computational resources, especially in the last two decades, more demanding two- and three-dimensional transitional and turbulent flows appeared in the literature [1, 2, 3], contributing to understand the physical phenomena of turbulence and providing useful data.

Compared with the plethora of the studies concerning air-filled cavities (Prandtl number $Pr = 0.7$), the works focused on water-filled cavities are rather scarce [4, 5, 6]. This can be due to, but not limited to, factors like the additional difficulty associated with thinner boundary layer [7], which requires finer grids to capture the smallest scales of the turbulent flow, thus increasing the cost of the calculations. It must also be kept in mind that, unlike air-filled cavities, the validity of the Oberbeck-Boussinesq (OB) approximation might be questioned [8], especially as a result of significant variations in viscosity when the working fluid is water under low-to-moderate temperature differences.

Interesting studies appeared in the literature addressing water-filled cavities with variable thermophysical properties for the Rayleigh Bénard (RB) problem. This configuration -in spite of the expected differences due to the change in the direction of thermal gradient- can serve as a reference to understand the physics that is present in a water-filled DHC flow. Ahlers et al. [9] studied the non-Oberbeck-Boussinesq (NOB) effects of water and other liquids for RB both experimentally and theoretically, finding that the Nusselt number (Nu) and Reynolds number (Re) are not sensible to the NOB effects despite a variation of a factor of 2 in viscosity and thermal expansion coefficient between the top and bottom plates. In their study, although NOB effects can be observed as the temperature drops are taken into account, these finally do not affect the global Nu and Re, which is explained by the compensation of the NOB corrections by means of the shift in the temperature at center of the cavity. Sugiyama et al. [10] performed 2D simulations for the RB convection considering both OB approximation and NOB effects, focusing on aspects like the deviation of the center temperature from the arithmetic mean, thermal boundary layer thicknesses in both top and bottom walls, and symmetry of the flow structure as the NOB effects are taken into account. Their numerical results, despite employing a 2D approximation, match well with the available experimental data, like the center temperature and Nu number proportions. They also found that the NOB deviations in Re are strongly governed by the temperature dependance of the thermal expansion

coefficient. Horn *et. al.* [11] recently studied the NOB effects in three-dimensional Rayleigh-Bénard convection for glycerol in a cylindrical cell of aspect ratio 1. They conducted an extensive study within a wide range of Rayleigh numbers and temperature differences, analyzing temperature and velocity profiles, thermal and viscous boundary-layer thicknesses, and the temperature of the core. Besides the differences in flow structures and the loss of symmetry, they found the considerably warmer cavity core as the most remarkable NOB effect in their study. Moreover, at higher Rayleigh numbers, they identified the typical large scale circulation which was not captured in the previous two-dimensional simulations of Sugiyama *et al.* [12], concluding that three-dimensional simulations are required to capture all the relevant NOB effects.

With the present work, the authors aim at taking to a further step the recent studies of turbulent flow in a tall water-filled DHC. In a previous study, the authors [6] studied the NOB effects in a tall DHC by means of two-dimensional direct numerical simulations (DNS), identifying important NOB effects beyond the temperature difference of $30\ ^{\circ}C$ between the hot and cold walls. However, in spite of the loss of symmetry registered it was observed that these effects do not degrade the stratification zone which simply shifts towards the top of the cavity.

The present study, thus, focuses on the analysis of the NOB effects and their impact on the boundary layers and on the mechanism of transition to turbulence by means of three-dimensional DNS in a water-filled DHC cavity of aspect ratio 10. The study aims at shedding light into the physics of the complex flow under consideration, and particularly into the topology of the flow and the dynamics of the boundary layers. In order to check the adequacy of the 2D assumption in capturing the NOB effects, two-dimensional DNS are also performed. A complete analysis of the turbulent flow is accomplished.

The remainder of the present paper is organized as follows. In the next section, the studied case is defined. Then, Section 3 is devoted to the mathematical and numerical methodologies, together with the details of the mesh studies. In Section 4, the numerical results obtained by both using OB approximation and considering NOB effects are extensively compared. The analysis includes the instantaneous flow structures, boundary layer analysis, topology of the flow, energy spectra, stratification, and heat transfer. Finally, discussion and concluding remarks are given in Section 5.

3.2 Definition of the case

The turbulent natural convection submitted to study for a DHC element of height H, width W, and depth D is shown in Figure 3.1. The present configuration yields a height aspect ratio, $\Gamma = H/D$, of 10. This aspect ratio was studied previously by Le

Table 3.1: Coefficients a_n of the equation 3.1 to calculate the temperature dependent thermophysical properties of water.

n	ρ (kg/m^3)	C_p $(J/kg \cdot K)$	μ $(kg/m \cdot s)$	k (W/m)
0	8.487×10^{2}	2.282×10^{4}	1.942×10^{-1}	-2.978×10^{0}
1	1.29×10^{0}	-1.94×10^{2}	-2.19×10^{-3}	3.07×10^{-2}
2	-2.6×10^{-3}	7.52×10^{-1}	9.89×10^{-6}	-9.8×10^{-5}
3		-1.29×10^{-3}	-2.22×10^{-8}	1.43×10^{-7}
4		8.3×10^{-7}	2.4×10^{-11}	-8.2×10^{-11}
5			-1.1×10^{-14}	

Quéré [4] for water-filled cavity on a 2D domain, in order to determine the critical Rayleigh number for the transition to unsteady natural convection. The depth aspect ratio, $\Gamma_d = D/W$, is 0.75. As will be shown in the next section, this span width is sufficiently large to contain all the scales of the flow. The cavity is heated and cooled by means of vertical isothermal confining walls, whose temperatures are set to $T_h = 90\ ^\circ C$ and $T_c = 10\ ^\circ C$, respectively. The top and bottom walls are adiabatic. No-slip condition is adopted in these horizontal and vertical confining walls, while in the spanwise direction periodic boundary condition is imposed.

The cavity height-based Rayleigh number, $Ra = |\mathbf{g}|\beta(T_h - T_c)H^3Pr/\nu^2 = 3 \times 10^{11}$, and the Prandtl number, $Pr = \nu/\alpha = 3.41$, where $\mathbf{g}$ is the gravity acceleration, β is the thermal expansion coefficient, ν is the kinematic viscosity, α is the thermal diffusivity. The thermophysical properties of water are calculated at the mean temperature, i.e. at $T_m = (T_h + T_c)/2 = 50\ ^\circ C$. The variable thermophysical properties of water used in the present NOB approach are adapted from [14] yielding the following temperature dependance:

$$\phi(T) = \Sigma_{n=0}^{N} a_n T^n \tag{3.1}$$

where ϕ is the thermophysical property (ρ, C_p, μ, k), T is the temperature in Kelvins, and the coefficients a_n of equation 3.1 are given in Table 3.1.

3.3 Mathematical and numerical model

OB approximation is a mathematical convenience which is commonly adopted to derive more manageable governing equations. The approach consists of considering constant thermophysical properties except for the density in the buoyancy term, which is approximated as a linear function of temperature. If the thermophysical properties are a weak function of temperature, this approximation can yield reliable

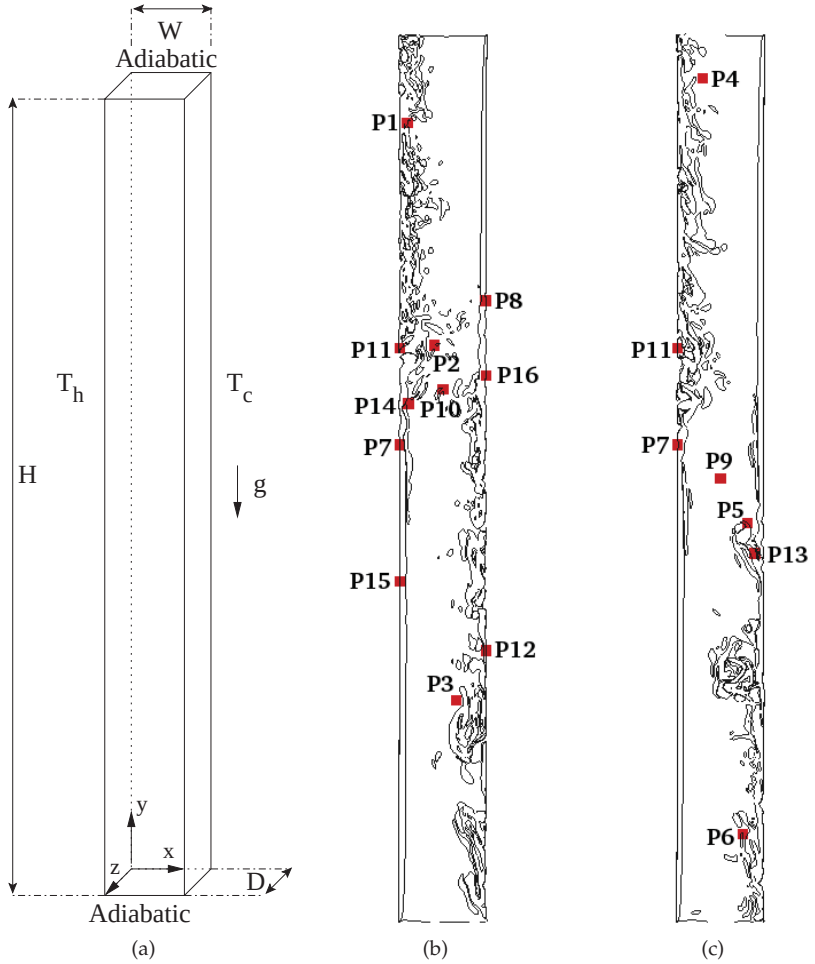

Figure 3.1: Geometry of the case submitted to study (a), locations of the probes used in two-point correlations and energy spectra for NOB (b) and OB (c) simulations.

results. The expected validity of the OB approximation was mathematically specified [8], questioning indeed its applicability for even small temperature differences as $2\ ^{\circ}C$ for water.

The present investigation is on the determination of the NOB effects by means of three-dimensional DNS. To that end, the DNS of the defined case is first performed considering the well-known OB approximation, which assumes that the thermophysical properties are constant. In order to account for the buoyancy force, the driving force of the natural convection flow, the temperature dependence of the density is linearized using the thermal expansion coefficient. The resulting governing equations take the following form:

$$\begin{aligned} \nabla \cdot \mathbf{u} &= 0, \\ \partial_t \mathbf{u} + \mathcal{C}(\mathbf{u},\mathbf{u}) &= \nu_m \Delta \mathbf{u} - \nabla p - \beta_m (T - T_m)\mathbf{g}, \\ \partial_t T + \mathcal{C}(\mathbf{u},T) &= \alpha_m \Delta T, \end{aligned} \tag{3.2}$$

where $\mathbf{u}$ denotes the velocity field $\mathbf{u} = (u, v, w)$, p is the kinematic pressure, and the convective term is given by $\mathcal{C}(\mathbf{u},\mathbf{v}) = (\mathbf{u}\cdot\nabla)\mathbf{v}$. The subscript m denotes that the thermophysical properties are evaluated at the mean temperature T_m. The considered NOB approach leads to the following governing equations:

$$\begin{aligned} \nabla \cdot \mathbf{u} &= 0, \\ \partial_t \mathbf{u} + \mathcal{C}(\mathbf{u},\mathbf{u}) &= 2\rho_m^{-1} \nabla \cdot (\mu S(\mathbf{u})) - \nabla p + (1 - \rho/\rho_m)\mathbf{g}, \\ \partial_t T + \mathcal{C}(\mathbf{u},T) &= (\rho_m C_{p,m})^{-1} \nabla \cdot (k \nabla T), \end{aligned} \tag{3.3}$$

where $S(\mathbf{u}) = 1/2(\nabla \mathbf{u} + \nabla \mathbf{u}^T)$ is the rate-of-strain tensor. Note that in the present approach, the dynamic viscosity, $\mu(T)$, and $k(T)$ are temperature dependent whereas $C_{p,m}$ and ρ_m are constant and evaluated at the mean temperature, with the exception of the buoyancy term where the temperature dependence of the density is properly taken into account. It is expected that ignoring the temperature dependance of $C_{p,m}$ and ρ_m would not alter the present results, considering that these two properties are weak functions of temperature under the conditions of the studied case. Note that the same NOB approach was employed in [10] for RB convection of water.

Both set of equations (OB and NOB) are discretized by means of a finite volume fully conservative fourth-order scheme [15]. For time integration, a second order explicit scheme [17] is used. The pressure-velocity linkage is solved by means of an explicit finite volume fractional step procedure. The generated domain is periodic in the $z-$direction. Therefore, the system of equations is reduced to a set of 2D systems by means of a Fourier diagonalization method. These systems are solved using a Direct Schur complement-based domain decomposition method in conjunction with a Fast Fourier Transform [18]. The present methodology was successfully employed in previous DNS studies with similar flow configuration (see, for instance [2, 3, 13]).

In the case of NOB, in order to overcome the difficulty in the discretization of the viscous dissipation term for the NOB case, $2\nabla \cdot (\mu S(\mathbf{u}))$, with spatially varying dynamic viscosity the following form for the viscous term

$$2\nabla \cdot (\mu S(\mathbf{u})) = \nabla \cdot (\mu \nabla \mathbf{u}) + \nabla(\nabla \cdot (\mu \mathbf{u})) - \mathcal{C}(\mathbf{u}, \nabla \mu), \tag{3.4}$$

has been derived, as shown in [16]. From a numerical point-of-view, the most remarkable property is that it can be straightforwardly implemented by simply reusing operators. Moreover, for constant viscosity, formulations constructed via Eq. 3.4 become identical to the original formulation since the last two terms in the right-hand-side exactly vanish.

3.3.1 Verification of DNS solutions

The DNS code for OB approximation was previously verified by means of several benchmark results (see for instance [2]) and also by using the Method of Manufactured Solutions (MMS) [19]. The present DNS results, similar to the previous conducted DNS studies [2, 3, 13], use a random initial perturbation of the initial temperature field to trigger three-dimensionality. The flow statistics are averaged over two statistically invariant transformations: time and spanwise direction for both OB and NOB studies. In the case of OB DNS, the central-point symmetry is additionally employed. This averaging for both studies is hereafter denoted as $< \cdot >$. The results are presented in dimensionless form, using the reference quantities $L_{ref} = H$, $t_{ref} = (H^2/\alpha)Ra^{-0.5}$, $v_{ref} = (\alpha/H)Ra^{0.5}$, and $\Delta T_{ref} = (T_h - T_c)$, for length, time, velocity, and temperature, respectively. In order to assure that time-independent solution is obtained, several numerical probes are located at representative locations in the domain (see Figure 3.1 and Table 3.2). In Figure 3.2, the evolution of temperature and streamwise velocity component in some of these representative locations are depicted, together with their corresponding accumulated fluctuations and mean values for the NOB DNS. Note that part of the initial transient period prior to the statistical steady-state has been excluded from the calculations in order to properly determine the time-independent solution. The gray solid lines represent the time evolution of the observed variable, while the black solid lines and the dashed lines show the time-averaged mean value and time-averaged fluctuation value, respectively. Note that the time-averaging begins at the simulation time of $t/t_{ref} = 160$. The convergence of the two mentioned time-averaged statistics to a certain mean value is taken as the criterion for the adequacy of the chosen time-integration period. Given the disparity among the time scales present in this complex flow configuration, the more restrictive larger time scale probes have been considered to properly evaluate the time-independent statistics. Consequently, notice that while the chosen time-integration period is more than sufficient to properly evaluate the first-order

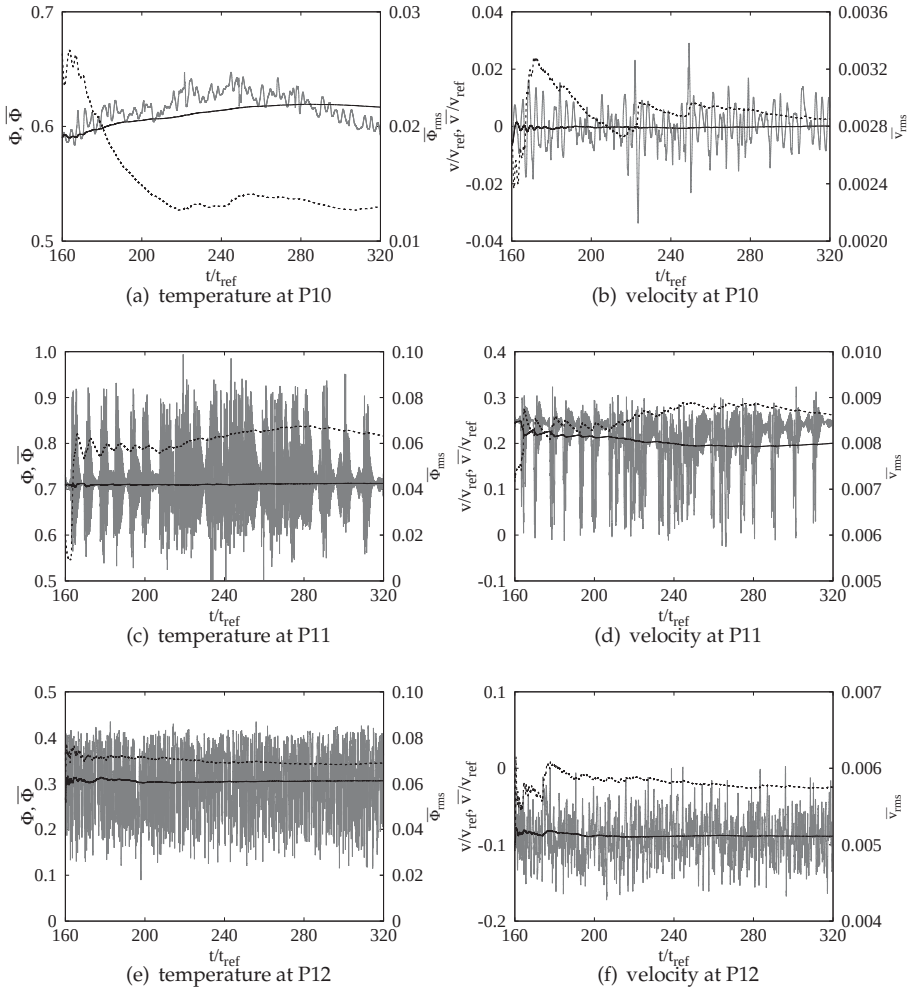

Figure 3.2: Evolution of temperature, streamwise velocity, their time-averaged mean and fluctuation values for different locations considering NOB. Gray and black solid lines represent the time history of the probe reading and their time-averaged mean values, respectively. Dashed lines depict the time-averaged fluctuations. See Table 3.2 for probe locations.

Table 3.2: Location of numerical probes used in the present NOB and OB simulations.

Probe	x/H	y/H
P1	0.01000	0.9000
P2	0.04000	0.6500
P3	0.06500	0.2500
P4	0.03000	0.9500
P5	0.08000	0.4500
P6	0.07500	0.1000
P7	0.00160	0.5381
P8	0.09775	0.7000
P9	0.05000	0.5000
P10	0.05000	0.6000
P11	0.00198	0.6468
P12	0.09798	0.3064
P13	0.08854	0.4157
P14	0.01146	0.5842
P15	0.00181	0.3845
P16	0.09819	0.6155

statistics for P11 and P12, it can be observed that even a slightly shorter period would fail in determining the first-order time-independent statistics of P10, which is located on the vertical centerline. On the other hand, for P11 located in the proximity of the hot wall transition point, whose vertical oscillations due to the Tollmien-Schlichting (TS) waves can result in dissimilar fluctuation patterns, larger integration periods are required, which is critical to capture the second-order statistics. As for the more turbulent locations like P12, both the first and the second order statistics can be determined at shorter time-integration periods. An analogous analysis has been carried out considering the DNS with OB approximation, as can be seen in Figure 3.3. The center of the cavity, a zone with typically larger time scale, plays a dominant role in determining the time-integration period, as shown in Figure 3.3(a). It is interesting to note that P11 falls in the turbulent zone under OB approximation (see Figure 3.2(c) for its transitional behavior when NOB effects are considered). This anticipates an upstream transition in the hot wall if NOB effects are not taken into consideration. Indeed, as is manifest from this example, independent analyses are required for the adequate time-integration periods for the OB and NOB DNS studies.

The meshes used for the grid study, and the numerical parameters of the simula-

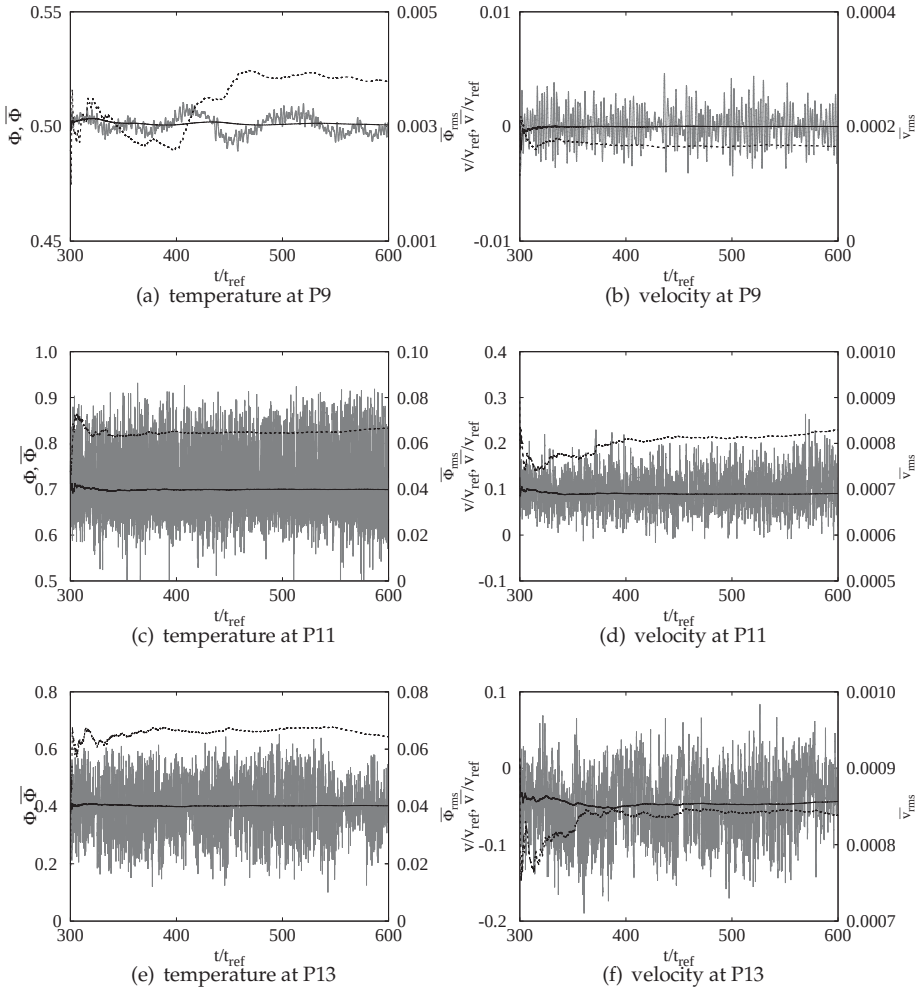

Figure 3.3: Evolution of temperature, streamwise velocity, their time-averaged mean and fluctuation values for different locations considering OB. Gray and black solid lines represent the time history of the probe reading and their time-averaged mean values, respectively. Dashed lines depict the time-averaged fluctuations. See Table 3.2 for probe locations.

tions are given in Table 3.3. Grid spacing in the streamwise and spanwise directions is chosen uniform, while for the wall-normal direction, the following hyperbolic-tangent function is used:

$$x_i/H = \frac{W}{2H}\left(1 + \frac{tanh\left[\gamma_x\left(2(i-1)/N_x - 1\right)\right]}{tanh\gamma_x}\right) \qquad i = 1, 2, ..., N_x + 1 \tag{3.5}$$

where x_i indicates the location of the control volume face, γ_x is the mesh concentration factor and N_x is the number of CVs in the wall-normal direction. This approach of grid generation was previously used in other DNS studies [2, 6, 13], providing satisfactory results. The simultaneous fulfillment of both adequate grid resolution in the xy-plane -through adequate placement of the grid points in wall-normal and streamwise directions- to solve the smallest scales of the flow, together with the sufficiently large periodic direction grid size to contain the largest scales of the flow is required in the DNS study. In the quest of the adequate grid resolution, the present study initially adopted the considered spanwise grid size of a previous OB DNS study on a tall water-filled cavity of the same Rayleigh number [13]. That study showed that the first- and second-order turbulent statistics were not affected when a spanwise domain of half the cavity width, $D/W = 0.5$, was employed. Although not shown here, different grids have been tested, keeping this spanwise grid parameter constant. Successive studies have shown that *Mesh B* (see Table 3.3) is sufficiently fine to reproduce the physics of the flow properly. However, given the inclusion of the NOB effects in the DNS of this rather complex flow configuration, and as a further step to assure that the flow parameters are not affected by the periodic direction domain size, *Mesh A* has been generated by expanding the spanwise domain size (and also the CVs in this direction) by 50 %, and tested in the OB DNS. In order to check the adequacy of the periodic direction computational domain size in capturing the largest scales of the flow, spanwise two-point correlation, $R_{\phi\phi}$, defined as

$$R_{\phi\phi}(x, y, \delta z) = \frac{< \phi'(x, y, z)\phi'(x, y, z + \delta z) >}{< \phi'^2(x, y, z) >} \tag{3.6}$$

with ϕ' the fluctuation of the variable ϕ, ($\phi' = \phi - < \phi >$), is used. In Figure 3.4, the correlation values are plotted using the spanwise velocity fluctuations, w', at three monitoring points for OB and NOB. See Figure 3.1 for the locations of these probes. It can be observed that the larger span can be justified, especially for the OB case, since the correlations have a better trend to fall off to zero, which indicates that the narrower mesh might not be sufficient to represent all the scales of the flow. Note that due to the planning of the present investigation, OB simulations are followed by the corresponding NOB DNS, which indeed required almost four-times higher computational resources. Particularly, *Mesh C* simulations considering NOB

Table 3.3: Numerical simulation parameters for DNS. N_x, N_y, and N_z are the number of CVs in wall-normal, streamwise, and spanwise directions, respectively. $(\Delta x)_{min}$ and $(\Delta x)_{max}$ are the smallest and largest wall-normal distances, respectively, and γ_x is the mesh concentration factor.

Case	N_x	N_y	N_z	D/H	γ_x	$(\Delta x)_{\min}/H$	$(\Delta x)_{\max}/H$
Mesh C	174	702	96	0.050	1.8	1.15×10^{-4}	1.09×10^{-3}
Mesh B	194	782	128	0.050	1.8	1.03×10^{-4}	9.80×10^{-4}
Mesh A	194	782	196	0.075	1.8	1.03×10^{-4}	9.80×10^{-4}

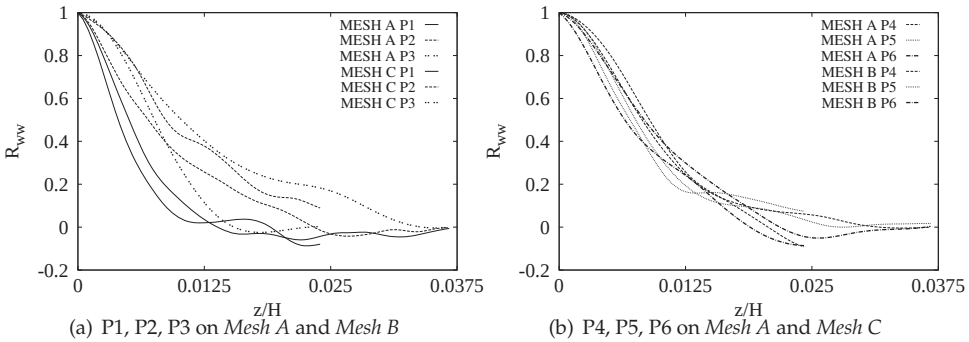

(a) P1, P2, P3 on *Mesh A* and *Mesh B* (b) P4, P5, P6 on *Mesh A* and *Mesh C*

Figure 3.4: Two-point correlations of the spanwise velocity fluctuations, w, at different monitoring locations. NOB (a), OB (b).

effects concluded while *Mesh A* using OB approximation was at an advanced level of simulation. In accordance with the outcomes of the preliminary results and having anticipated the justification of the use of denser *Mesh A* grid in the OB study, *Mesh B* simulation considering NOB effects were omitted owing to the efficient usage of the available computational resources, and the NOB simulations were proceeded with the denser *Mesh A*. For this reason, the two-point correlations for NOB compare *Mesh A* with the second-available denser mesh, *Mesh C* (see Figure 3.4).

As for the grid resolution, the near-wall regions are the most critical, since the proper resolution of the boundary layer directly affects the success of the simulations. In this regard, the location of the first grid point in the vertical boundary layers has to be sufficiently close to the wall to permit proper resolution of the boundary layer. This location is depicted in Figure 3.5 using wall-units for *Mesh A*. Note that wall-units are defined as $(\Delta x)^+ = u_\tau (\Delta x)_{min}/\nu$, where u_τ is the friction velocity cal-

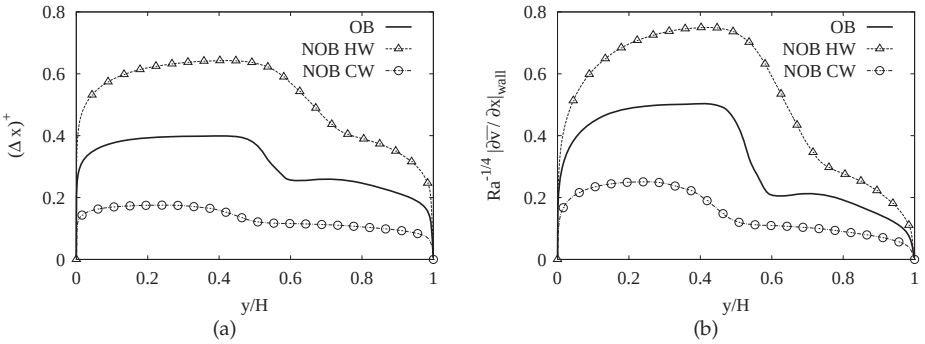

Figure 3.5: (a) Location of the first grid point (b) scaled wall shear stress values for the DNS considering both NOB effects and OB approximation.

culated as $u_\tau = (\tau_w/\rho)^{1/2}$ and τ_w is the wall friction given by $\tau_w = \rho\nu|(\partial v/\partial x)|_w$. In the same figure, the corresponding scaled wall shear stress values are also depicted considering both NOB effects and OB approximation. It can be observed that the location of the non-dimensional wall-normal distance falls well below the unity for both cases, indicating sufficient grid resolution.

In turbulent regions, the smallest resolved length scale is required to be in the order of Kolmogorov length scale, $\eta = (\nu/ < \epsilon >)^{1/4}$, where $< \epsilon >$ is the time-averaged local dissipation of turbulent kinetic energy. In Figure 3.6, the ratio between the wall-normal grid spacing and the Kolmogorov length scale is depicted at three representative horizontal profiles for both NOB and OB cases using *Mesh A*. Notice that this ratio is generally smaller than unity for these representative locations, thus confirming the adequacy of the grid resolution.

Finally, in support of the present analysis, representative first- and second-order statistics are compared for the OB and NOB simulations, in order to check the influence of the grid resolution and spanwise domain size on these results. Although not shown here, indistinguishable behavior is observed in the comparison of the first-order statistics for both simulations. As for the second-order statistics, however, the employment of 50 % larger domain size in the periodic direction seems to slightly affect the statistics, although none qualitative difference is reported as the physics of the flow is concerned (see Figure 3.7). In case of the NOB simulations, the deviations are more visible, still not affecting the trend observed in the critical locations of the flow. Notice that both the improvement of the mesh resolution in xy-plane and enlarged periodic domain size contribute to these somehow more noticeable differences. In accordance with the before-mentioned results, for both cases OB and

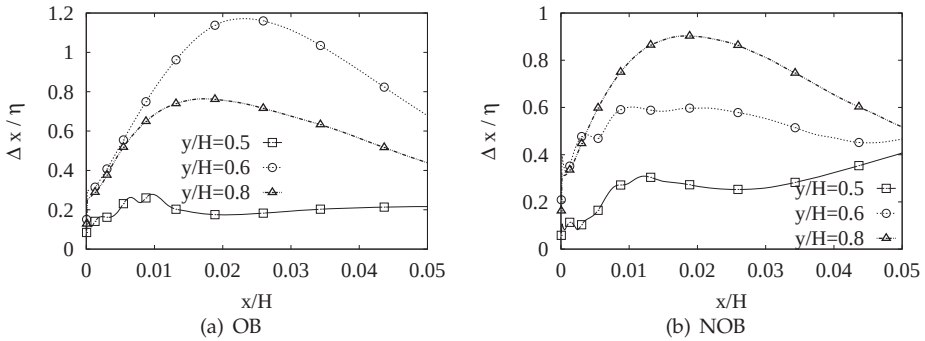

Figure 3.6: Ratio between wall-normal grid spacing and Kolmogorov length scale, η, over $y/H = 0.5, 0.6, 0.8$ by means of DNS.

NOB, the employment of *Mesh A* is justified since the second order statistics, thus the physics of the flow, may not be properly captured if *Mesh C* is used.

Owing to the present analysis, *Mesh A* results are referred to as the DNS results hereafter for this configuration. Nonetheless, as usual, a compromise between accuracy and the cost of the calculations are adopted.

3.4 Numerical results

In this section, the physics of the flow under consideration, and particularly the influence of the NOB effects, will be analyzed in detail by means of the obtained numerical data, with focus on the dynamics of the flow, time-averaged flow parameters, heat transfer, and the boundary layer.

3.4.1 Instantaneous flow

The analysis of the instantaneous flow is critical in identifying the dynamics of the flow. This configuration involves some flow patterns like the fluid accelerating along the vertical boundary layers up to a location where the instabilities grow and the boundary layer is disrupted. In the core of the cavity, where a stratified region can be identified, the flow is in motion with relatively small velocity values.

Analyzing in more detail the time traces of temperature and vertical velocity shown in Figures 3.2 and 3.3, one can see that, as expected, different flow regimes coexist in the cavity (notice the difference in velocity magnitude in different locations).

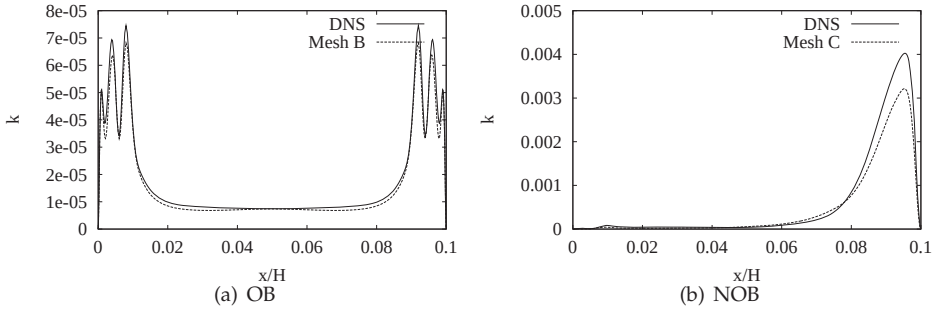

Figure 3.7: Mesh resolution study using turbulent kinetic energy at $y/H = 0.5$.

Moreover, a dissimilar flow regime can be observed at identical locations if the NOB effects are considered, as has been pointed out in the previous section.

In Figure 3.8, a sequence of instantaneous isotherms are depicted. The graphs are formed by homogeneously spaced contour lines between $\Phi = (T - T_c)/\Delta T_{ref} = 0$ and $\Phi = 1$ for both NOB and OB cases. The three graphs on the left correspond to the NOB case, while on the right side their OB counterparts are shown. In all the graphs, quasi-horizontal parallel isotherms are visible in the core of the cavity, except for the vicinity of the vertical boundary layers, which are regions of high temperature gradients in the wall-normal direction. Note that, as a general consideration for this configuration, the fluid heated (cooled) in the hot (cold) vertical wall accelerates, traveling up to the transition location where finally is ejected in the core of the cavity. Note that this ejected fluid, due to the fact that it partly originates from upstream locations, is potentially colder (warmer) then the one found in the proximity of the corresponding transition region. This colder (warmer) fluid eventually descends (ascends) as a result of the existing density gradient, giving rise to a parallel and opposite flow.

In the case of OB (see Figure 3.8), the isotherms are ordered in a symmetric manner, giving rise to a central highly stratified region. This region seems to be placed in between the locations of the hot and cold wall boundary layers where large-eddies are injected in the core of the cavity. It is interesting to figure out that the location where these large unsteady plumes are ejected in the core of the cavity is found slightly downstream with respect to the midheight location on both vertical boundaries. Thus, the enhanced mixing effect of these ejected eddies forms large bands of isotherms above and below the midheight location, giving rise to a highly stratified zone in the central region. However, when the NOB effects are considered,

(a) $\tau \approx 416$ (b) $\tau \approx 417$ (c) $\tau \approx 418$ (d) $\tau \approx 600$ (e) $\tau \approx 601$ (f) $\tau \approx 602$

Figure 3.8: A sequence of instantaneous isotherms separated by one dimensionless time, $\tau = t/t_{ref}$. (a-b-c) NOB; (d-e-f) OB.

the organization of the isotherms present some notable differences: the flow is no longer symmetric, and the highly-stratified region found in the center of the cavity disappears. Indeed, in the hot wall boundary layer, the transition to turbulence is delayed as can be observed from the location of the large plumes which are visible at a relatively higher location of the cavity in comparison with the OB case. As for the cold wall, in contrast with the OB case, the first instabilities are triggered earlier, although the formation and shedding of cortices to the core is not as intensive as in the hot wall. The combined effect of the upward shift of the transition points on both boundary layers, which is more pronounced on the cold wall, is partly responsible for the vanishing of the stratified zone, as the relative positions of these locations do not precisely favor the stratification phenomena. Due to both the overlapping effect of the mixing power from both walls, and the unstable behavior of the both boundary layer transition locations observed when NOB effects are involved, the expected stratification region expands vertically in size producing finally a degradation in the stratification value, $S = \partial\Phi/\partial Y|_{x,y=0.05,0.5}$. This phenomena will be further discussed in this chapter.

The coherent structures in the vertical boundary layers can be captured by means of the Q-criterion method proposed by Hunt et al.[21]. In Figures 3.9 and 3.10, the

vortical structures considering NOB effects are depicted for a time sequence of snapshots in the hot and cold wall boundary layers, respectively. Note that the figure displays the upper half of the hot wall boundary layer, i.e. $0.5 \leq y/H \leq 1.0$. In the cold wall boundary layer, a centered element of identical size, i.e. $0.25 \leq y/H \leq 0.75$, is chosen to be able to highlight the transition region, which occurs earlier. In all the snapshots, two-dimensional Tollmien-Schlichting (TS) structures are clearly visible in the upstream part of the boundary layers. These structures are initiated as the instabilities appear, and they travel downstream while the nonlinearities are slowly amplified. This can be observed in the structures at more downstream location, which still preserve to a large extent their two dimensionality while small variations are introduced due to the interaction between the high speed flow in the boundary layer and the low speed opposite direction flow in the outer edge of the viscous boundary layer, which develops as the relocated fluid from upstream locations try to find its way back to the original location.

In the particular case of the hot wall boundary layer (see Figure 3.9), the high speed 2D TS structures ascend along the wall up to a location where the interaction with the colder structures that are simultaneously descending at a lower velocity becomes important, and introduces instabilities in the boundary layer flow. As a consequence of this interaction between the ascending and descending flows, the TS structures decelerate and form small-to-medium vortex structures (see Figures 3.9(a)- 3.9(b)). Then, they cluster with the newly ascending 2D TS structures to form a larger vortex as can be seen in Figure 3.9(c). At times, two independent vortex structures appear, which later unify to form an even larger vortex which is then shed away from the wall to the core of the cavity, as can be captured in the sequence of snapshots in Figures 3.9(d)- 3.9(f). This process of ejecting large vortex structures also introduces instabilities in the ascending 2D TS structures, which become 3D after the interaction, feeding further the vortex (see for instance Figure 3.9(e)).

In the cold wall, as can be observed in Figure 3.10, the combined motion of the cold fluid descending along the wall with the warmer fluid ascending in the outer edge of the boundary destabilizes the 2D TS structures that become first undulated (see Figures 3.10(a)-3.10(b)), then further downstream the legs of the structures begin to lift, roll up (see Figures 3.10(c)-3.10(d)), and then finally break into smaller pieces as can be observed finally in Figures 3.10(e)-3.10(f). This is the mechanism of the transition to turbulence taking place due to subsequent characteristic three-dimensional structure formation. Note that, in the upstream transitioning cold wall, large scale vortex formation is not observed in the same manner as in the hot wall. This might be due to the fact that in the hot wall boundary layer, the flow is decelerating as it approaches the transition location, after having accelerated along approximately half of the cavity height (see Figure 3.9) and reached relatively higher velocity values. The higher velocity means that the fluid from much lower (upstream) locations of

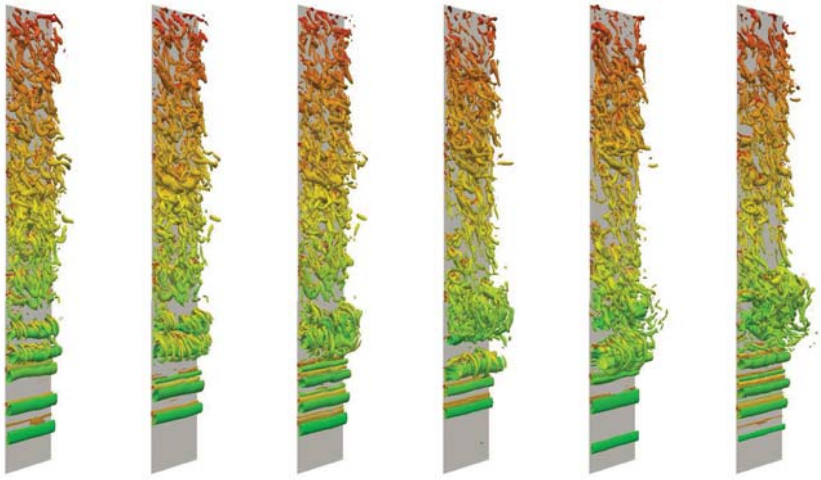

(a) $\tau = 418.81$ (b) $\tau = 418.94$ (c) $\tau = 419.04$ (d) $\tau = 419.47$ (e) $\tau = 419.70$ (f) $\tau = 420.51$

Figure 3.9: Visualization of instantaneous vortical structures considering NOB effects in the hot wall boundary layer.

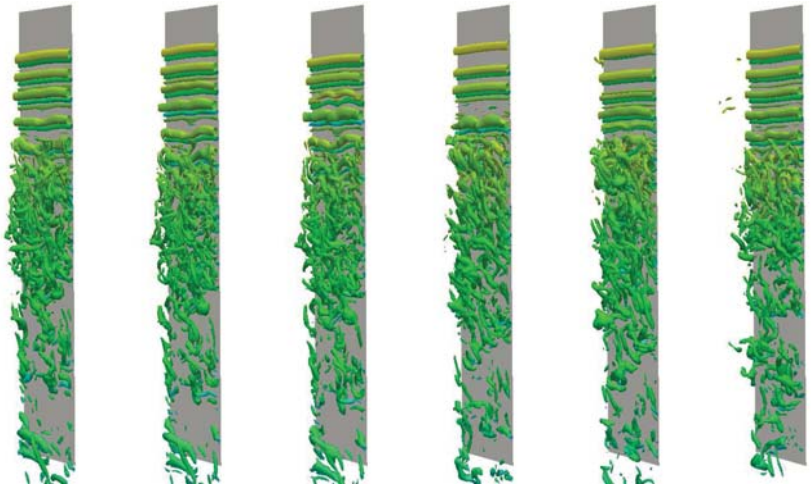

(a) $\tau = 418.81$ (b) $\tau = 418.94$ (c) $\tau = 419.04$ (d) $\tau = 419.47$ (e) $\tau = 419.70$ (f) $\tau = 420.51$

Figure 3.10: Visualization of instantaneous vortical structures considering NOB effects in the cold wall boundary layer.

the cavity, where fluid could be substantially colder, are dragged up to the transition location where these are then ejected in the core of the cavity. Due to the lower temperature and consequently higher density of the fluid which comes from the lower cavity, a flow in the opposite direction -descending flow- occurs. The velocity of the descending flow is expected to be proportional to that of the ascending flow, as they mutually feed each other. In the particular case of hot wall both velocities are of considerable magnitude, and their interaction thus gives rise to formation of large vortices. In the cold wall, however, the earlier triggered transition eventually hinders the formation of a significant ascending flow close to the outer edge of the cold boundary. This is due to the fact that the main stream within the cold wall boundary layer descends with a lower velocity magnitude with respect to the ascending flow observed in the hot wall. The relatively lower velocity results in a lower penetration power of the upstream fluid, which means smaller density gradients in the transition region when flow separation occurs. The buoyancy force as a result of these smaller gradients is not sufficiently high to compete with the gravity. Thus, in the absence of a significant ascending flow in this cold wall boundary, large eddies are not observed. The possible causes of early triggered transition in the cold wall will be further discussed in this section.

From Figures 3.9 and 3.10, the transition to turbulence locations in the hot and cold boundary layers can be identified, confirming the information deduced from the isotherms regarding the loss of symmetry. Note, though, the pronounced oscillation of this location upstream and downstream during the simulation. In Figure 3.11, the streamwise velocity evolution and its energy spectrum are depicted for P14 in the hot wall boundary layer past the midheight (see Figure 3.1). The figure shows the intermittency of the boundary layer instability mechanism. The instabilities registered at this point can be observed as high-frequency fluctuations with a high energy content. These intermittencies, which can be here identified with the passage of Tollmien-Schlichting waves (see for instance Figure 3.9) are quite similar to those registered in the detached boundary layer of circular cylinders and well described by Prasad and Williamsom [22]. Indeed, the footprint of these instabilities is effectively captured in the energy spectrum of Figure 3.11(b), as a broad-band peak centered around $f = 4.59$. Although not shown here in detail for other probes, these high-frequency intermittencies are manifest along the transitional hot and cold boundary layers for both OB and NOB cases, as this is the main mechanism of transition to turbulence. The low frequency captured as a peak centered at $f = 0.31$, in turn, is thought to be related with the oscillation of the transition point in the hot wall and with the shedding of the vortices from this boundary layer to the core.

In Figures 3.12 and 3.13, the resulting vortical structures for the OB case are depicted. Note that the mechanism of transition, the nature of the two-dimensional structures, and the breakdown of these structures into smaller three-dimensional

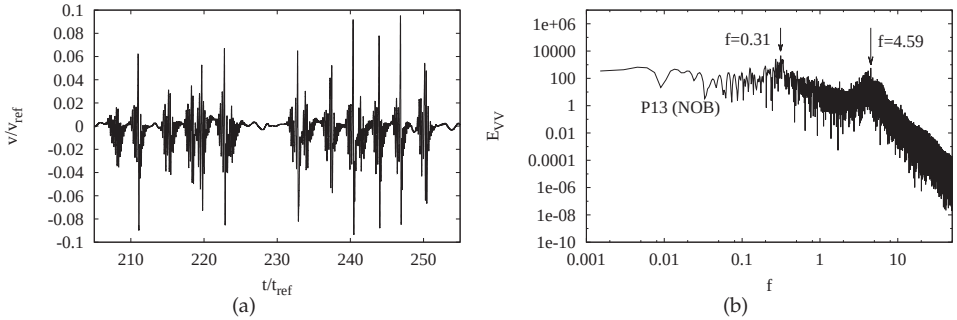

Figure 3.11: Time evolution of the streamwise velocity component of P13 (a) and its energy spectrum (b).

structures occur in an equivalent manner, as can be captured in the figures. The sizes of these structures are quite similar to those found in the NOB case. As expected, the flow exhibits a symmetric behavior with respect to the transition locations in the hot and cold boundary layers. In the hot wall for OB, less vortical structures after the transition location are observed when compared with the NOB case, which can be attributed to upstream transition of OB (see Figures 3.9 and 3.12) and subsequently shorter acceleration along the hot wall, which seems to result in less energetic vortices that die out before reaching the top of the cavity.

In Figure 3.14, the energy spectra of streamwise velocity fluctuations for P7, P8, P9, and P10 are depicted (see Figure 3.1 for probe locations). For the sake of clarity, spectra are shifted in the y-axis to allow their direct comparison. Similar to the energy spectrum shown in Figure 3.11, in the probes located in the boundary layers the frequency corresponding to the Tollmien-Schlichting (TS) waves can be identified as a broad band peak in the spectrum at $f = 4.59$ and $f = 4.76$ for NOB and OB, respectively. In an equivalent location in the cold wall boundary layer, the frequency of these instabilities is centered at $f = 4.91$. It is worth noting that the frequency of the TS waves for OB coincides with the arithmetic mean of the frequencies on hot and cold walls for NOB case.

In the cavity core region, as commented by Trias et al. [2], isotherms oscillate in a wave-like motion. This oscillation might be attributed to the influence of the vortices shed in the boundary layers and can be identified with the non-dimensional Brunt-Väisälä frequency $f_{BV,NOB} = (S \times Pr)^{0.5}/2\pi$, where S is the non-dimensional stratification number defined as the vertical temperature gradient in the center of the cavity. In Figure 3.14(b), the frequencies at the core of the cavity are identified. The

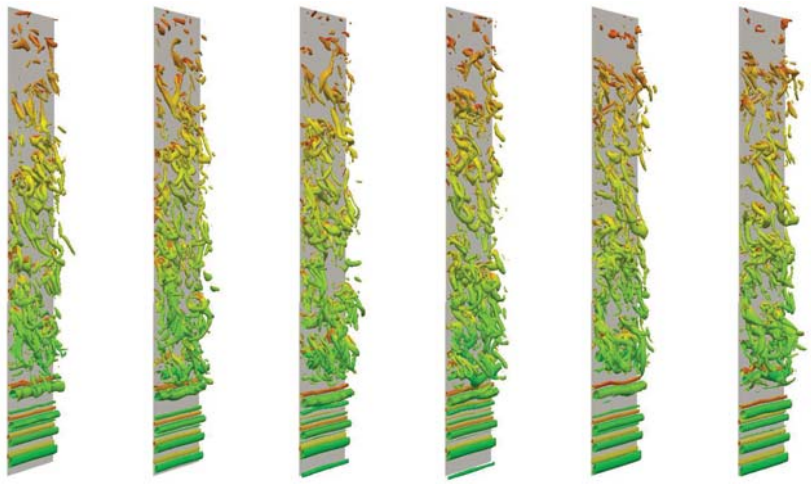

(a) $\tau \approx 600.22$ (b) $\tau \approx 600.56$ (c) $\tau \approx 600.91$ (d) $\tau \approx 601.30$ (e) $\tau \approx 601.80$ (f) $\tau \approx 602.00$

Figure 3.12: Visualization of instantaneous vortical structures for OB assumption in the hot wall boundary layer.

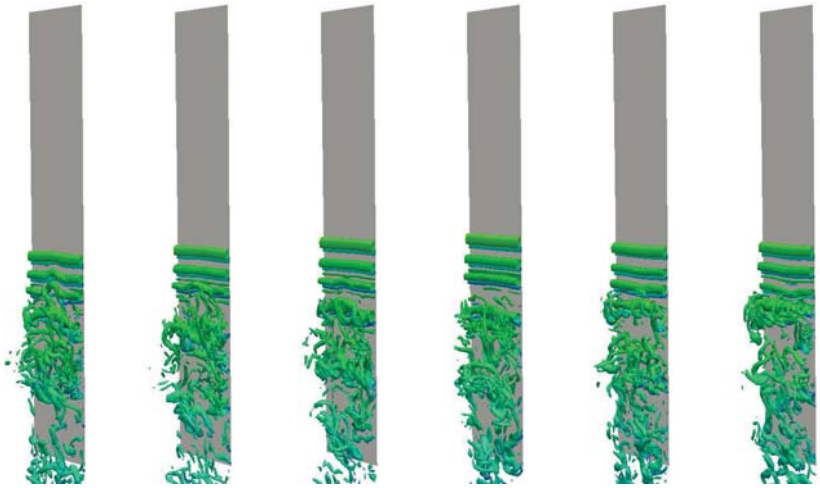

(a) $\tau \approx 600.22$ (b) $\tau \approx 600.56$ (c) $\tau \approx 600.91$ (d) $\tau \approx 601.30$ (e) $\tau \approx 601.80$ (f) $\tau \approx 602.00$

Figure 3.13: Visualization of instantaneous vortical structures for OB assumption in the cold wall boundary layer.

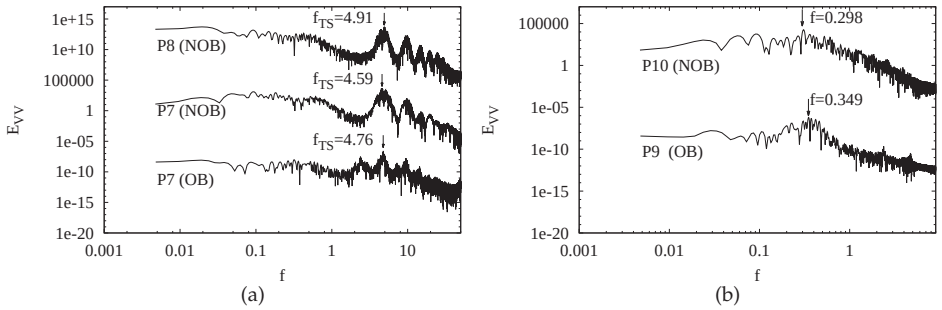

Figure 3.14: Energy spectra of streamwise velocity fluctuations at locations in the hot and cold vertical boundary layer, from bottom to top: P7 (hot wall) with OB, P7 with NOB, P8 (cold wall) with NOB (a); and in the core of the cavity, from bottom to top: P9 with OB, P10 with NOB (b). Bottom curve not shifted for both (a) and (b).

fundamental frequencies are found as $f = 0.298$ and $f = 0.349$ for NOB and OB, respectively. In the case of NOB, the frequency is in relatively good agreement with the Brunt-Väisälä frequency $f_{BV,NOB} = 0.285$. There is some discrepancy in case of OB, since $f_{BV,OB} = 0.471$.

Asymmetric transition to turbulence

In the context of the analysis of the observed NOB effects and their influence on the flow patterns, the delayed transition in the hot wall boundary layer, and the premature transition in the opposite cold wall boundary should be addressed. It is well-known that the present flow configuration is characterized by the corresponding Rayleigh and Prandtl numbers, and the aspect ratio. Beyond a critical value of the Rayleigh number, the conduction regime found within the cavity [23] becomes unstable and the natural convection regime is observed [25, 24], while the natural convection flow within the cavity undergoes a gradual transition to turbulence as the Rayleigh number is further increased (see [4, 5] , for instance). Indeed, Rayleigh number can be thought of as a measure of the strength of the driving force, i.e. buoyancy force, with respect to the damping by means of viscous and diffusive effects in a natural convection flow. Thus, given the symmetry present in the OB flow, the identical behavior of the hot and cold boundary layers for this case, can justify the well-established consideration of a unique Rayleigh number to characterize the flow. However, given the dissimilar flow structures detected in the hot and cold boundary

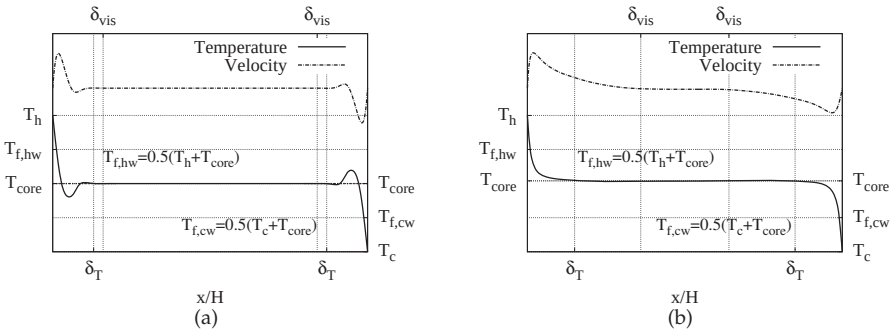

Figure 3.15: A representation of typical temperature and velocity profiles within a DHC cavity in statistically steady-state (not to scale) (a), temperature and velocity profiles for NOB case for an initial transient period of simulation (b).

layers for NOB, it might be a valid strategy to associate the particular flow regime experimented in each of the boundaries to a corresponding separate Rayleigh number. Moreover, due to the temperature dependance of the thermophysical property terms constituting the Rayleigh number, one might expect the existence of different Rayleigh numbers to characterize the strength and nature of the flow in each of the vertical boundaries. In Figure 3.15, a representation of typical average temperature and velocity profiles at an arbitrary height, y/H, of the cavity is depicted. Notice that in this representative example the temperature profile in the hot wall boundary layer falls from T_h value down to lower values, and then rises asymptotically to the corresponding core temperature in that height, T_{core}. In the cold wall, a similar but inverted phenomenon can be observed. As a consequence, a wide range of temperatures can be observed in the vicinity of a boundary layer, which may require the selection of a suitable fluid temperature to evaluate the corresponding Rayleigh number of the flow with variable thermophysical properties. Following a similar reconsideration of the Rayleigh number, Manga *et al.* [26] mention two possible approaches for a Rayleigh-Bénard flow with temperature-dependent viscosity: i) assumption of Rayleigh number based on corresponding wall temperature, ii) assumption of Rayleigh number based on the film temperature, which -adapted to the DHC case- can be defined as $T_f = 0.5(T_{wall} + T_{core})$ (see Figure 3.15(a)). In order to select a suitable reference temperature, some possible alternatives are visualized in Figure 3.16. In this figure, a boundary layer average temperature, defined as:

$$\Phi_{bl,wall} = \frac{1}{\delta_T} \int_{x_{wall}}^{x=\delta_T} \Phi(x) dx \tag{3.7}$$

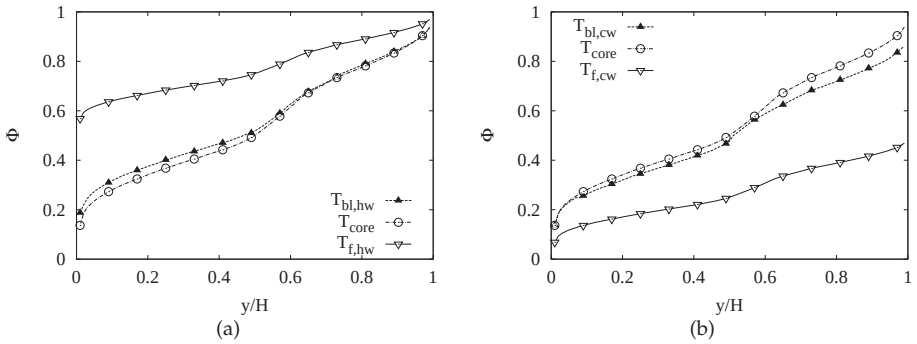

Figure 3.16: Comparison of different alternatives for a representative boundary layer mean temperature in (a) hot and (b) cold wall boundary layers considering NOB effects.

is also depicted. δ_T is the thermal boundary layer thickness, the details of which will be discussed in the next section. Notice that all data presented in this figure are gathered based on the statistically steady-state results for the NOB case. It is clear that the wall temperature is far from representing the mean fluid temperature in the boundary layer, as it solely constitutes an upper or lower limit ($\Phi_h = 1$ and $\Phi_c = 0$ not shown in the figure). Indeed, even the film temperature can be considered a distant approximation from this figure, especially for the particular conditions of the statistically steady-state regime. This actually can also be anticipated from the typical average isotherm presented in Figure 3.15(a) due to the observed overshooting below and above the core temperature in hot and cold walls, respectively. However, the core temperature is observed to be a valid alternative to represent the boundary layer average temperature, $\Phi_{bl,wall}$, especially when compared with the wall and film temperatures.

In line with the present discussion, we can estimate an equivalent Rayleigh number as

$$Ra_w^* \equiv \frac{|\mathbf{g}|\beta_{eq} H^3 Pr_{eq} |T_w - T_{core}|}{\nu_{eq}^2} \tag{3.8}$$

where w can represent the hot wall, h, or cold wall, c, boundary layers, and the subscript eq indicates that the values of β, Pr, and ν are evaluated at the corresponding reference (or equivalent) temperature. According to this approach, the intensity of the natural convection regime would vary depending on the particular height of the cavity -as the temperatures and thus the thermophysical properties depend on the

height-, whereas values at some representative locations could be useful to explain the dissimilar flow behavior found in this flow under NOB effects. Note that it is more convenient to employ the horizontal temperature gradient, $|T_w - T_{core}|$ in order to consider the dissimilar behavior in the vertical boundary layers, however it must be borne in mind that the resulting non-dimensional group obtained this way would only be an approximation of the classical Rayleigh number used in the DHC flows.

The present DNS studies depart from an initial temperature field of $T_{ini} = 0.5(T_h + T_c)$ with a random perturbation. In the initial period, the fluid in the cavity can be considered at this quasi-homogenous initial temperature. Thus, the fluid in the vicinity of both boundary layers are subject to an equivalent horizontal temperature gradient of $T_h - T_{core} = T_{core} - T_c$. Under these conditions, the strength of natural convection in the both vertical boundaries would be virtually equal, causing a preliminary ascending and descending flow of comparable intensity in both boundary layers. As the time marches, the boundaries gradually heat or cool their vicinity by an equivalent heating or cooling power. This effect, consequently provokes the formation of a boundary layer similar to one depicted in Figure 3.15(b). At this early stage, the cavity core still preserves its homogeneity substantially (see early stage temperatures in Figure 3.17(a) which depicts the transient core temperatures at different cavity heights). However the fluid in contact with the vertical walls have increased or decreased in temperature to some extent. The change in the temperature of this thin layer close to the vertical boundaries, start to affect the equivalent Rayleigh number of the hot and cold walls, as can be predicted from Eq. 3.8. Since the expected equivalent temperatures in both boundaries can follow the relation $\Phi_c \leq \Phi_{bl,c} \leq \Phi_{core} \leq \Phi_{bl,h} \leq \Phi_h$ (see Figure 3.15(b) for the temperature profiles in the vicinity of the walls for this initial stage, which essentially indicates an equivalent temperature similar to the film temperature), a relatively higher Rayleigh number is then expected in the hot wall for this early time span. Seki at al. [27] suggested the following correlation for laminar natural convection of water within a tall cavity:

$$Nu_H = 0.36(H/W)^{-0.11} Pr^{0.051} Ra_H^{0.25} \tag{3.9}$$

From this expression, although a lower Prandtl number is observed in the hot wall, taking also the equivalent Rayleigh number into account (which can be an approximation of the classical Rayleigh number), a considerably higher Nusselt number, i.e. considerably higher heat transfer can be foreseen in the hot wall for this initial period. This indeed can be observed in Figure 3.18(a) where the transient Nusselt numbers on hot and cold walls are depicted. Notice that for $t/t_{ref} \leq 20$, the cold wall Nusselt number, represented by a dashed gray line, is well below its hot wall counterpart. This fact points out a remarkable heating of the cavity in this initial period, as

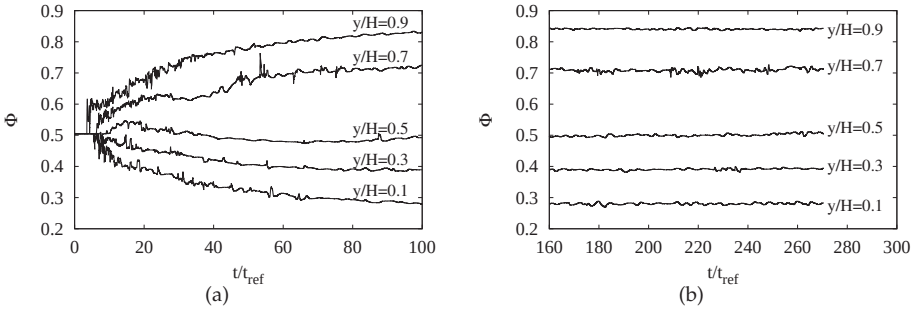

Figure 3.17: Time evolution of core temperature at different cavity heights. (a) initial period, (b) statistically steady-state period initial period.

the heat transferred from the hot wall to the core is greater than the heat transferred from the core to the cold wall. As the time further progresses, the heating and cooling effects begin to influence the core of the cavity (see Figure 3.17(a)), as a moderate stratification is seen to be established within the cavity. The upper part of the cavity reaches a relatively warmer state as a consequence of the before-mentioned enhanced heating attributed to the overall effect of the particular Rayleigh and Prandtl numbers attained in the hot wall boundary.

In order to shed light into the issue of dissimilar transition behavior in the hot and cold boundary layers, two numerical probes, P15 and P16, are located in symmetric locations within the hot and cold boundary layers. In Figure 3.19, the temperature evolution of these probes are depicted for the initial transient period. Note that the probes are located well before midheight, for which the isotherms and vortical structures have shown a laminar flow structure in the hot wall boundary layer considering NOB effects. In the figure, it can be observed that the intermittencies first appear in the hot wall, as early as $t/t_{ref} \approx 2$. This indeed corresponds to the start-up phase of the natural convection flow with homogenous cavity core, for which it has been argued that both boundaries have equivalent heating and cooling powers. Note that the instability later appears in the cold wall, at $t/t_{ref} \approx 3$, indicating that the intermittancies might be conveyed from the hot wall to the cold wall. Given the temperature distribution in the cavity for this phase which results in very similar equivalent Rayleigh numbers on both walls, one can reason that the observed transition location (detected at upstream of midheight for both boundaries) is characteristic of this corresponding equivalent Rayleigh number. However, at immediately later stages ($t/t_{ref} \approx 17$), the instabilities in the hot wall die out, while these still persist in the

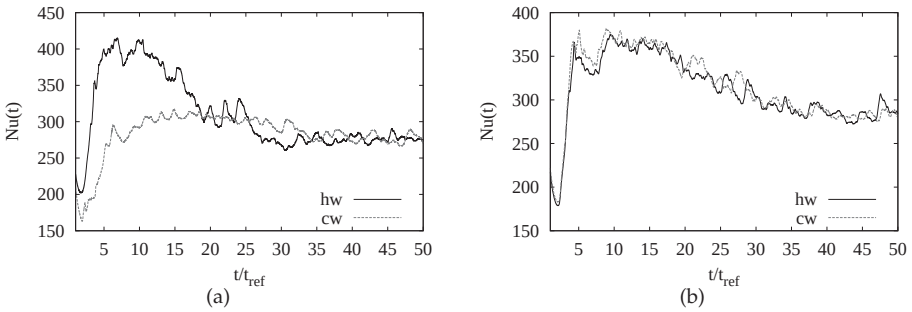

Figure 3.18: Time evolution of the instantaneous Nusselt number in the hot and cold walls under OB and NOB regimes during $t/t_{ref} \leq 50$. (a) NOB (b) OB.

cold wall. It is worth noting that this instant coincides approximately with the end of the period of enhanced heating of the whole cavity (see Figure 3.18(a)). Again, it must be noted that at this stage, a gradual stratification can be observed in the cavity core. In parallel, natural convection thermal and viscous boundary layers are more developed, resembling those shown in Figure 3.15(a) in laminar regions. These new conditions found in the cavity core and boundaries indeed introduce an inflection point regarding the flow regime. As a result of the stratification formed, due to lower temperatures in the bottom of the cavity with respect to the initial temperature field, the equivalent Rayleigh number starts to decrease in the upstream regions of the hot wall with respect to the initial value which gave rise to upstream transition. This reduction in the equivalent Rayleigh number explains the disappearing of the instabilities (see Figure 3.19), and anticipates a gradual downstream shift of the transition location in this boundary layer. In the cold wall, in turn, due to now warmer upper part of the cavity as a result of the ongoing enhanced heating, the equivalent Rayleigh number gradually increases in the upstream region of this boundary layer (note that the equivalent temperature in the boundary is similar to that of the core at a developed state of the natural convection flow as shown in Figure 3.16(b)). In Figure 3.17, the temperatures in the upper cavity continue to grow gradually which justifies the maintenance of the upstream transition location. The time evolution of the resulting equivalent Rayleigh numbers on both boundary layers are depicted in Figure 3.20, based on the cavity core temperatures presented in Figure 3.17(a). The current reasoning is reflected in this figure, as the equivalent Rayleigh number of hot wall peaks during the initial instants, followed by a flat reduction, while in the cold wall, the strength of the natural convection flow is observed to gradually increase.

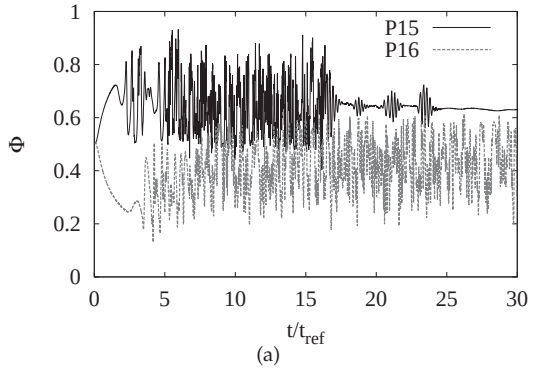

Figure 3.19: Initial period evolution of temperature for two probes located at symmetric locations, P15 and P16, in the vicinity of hot and cold walls, respectively.

Note, from Figures 3.17(b) and 3.21 that the process which ends up balancing the hot and cold wall heating and cooling powers by means of the gradual increments and reductions in the equivalent Rayleigh numbers is rather slow. This balance seems to be attained only after $t/t_{ref} \geq 370$ as can be observed in Figure 3.21.

The present approach, might partly be extrapolated to the OB case. In that case, the equivalent Rayleigh numbers would yield globally equal values on both vertical boundary layers due to constant and equal thermophysical properties. As a consequence, the heating and cooling power are expected to be essentially equal from the beginning since identical flow regime governs in both boundaries. This is indeed what is observed in Figure 3.18(b), where the instantaneous Nusselt numbers on both walls match closely.

Thus, in the light of the present discussion, it can be stated that the dissimilar transition behavior in the both boundary layers for NOB can be attributed to first an initial heating of the cavity due to favorable heat transfer properties at initial higher equivalent temperatures in the vicinity of the hot wall. As a consequence, this leads to warmer upper cavity which in turn feeds the cold wall boundary layer. As the time advances, the strength of the natural convection flow gradually decreases and increases in the hot and cold walls, respectively due to the effect of the feeding flow of these boundaries which originate from the gradually stratified flow. When balance is reached between the two boundary layers, the cold wall is found at higher equivalent Rayleigh number regime, which effectively results in a relatively earlier triggered transition. To support these ideas, some complementary first and second

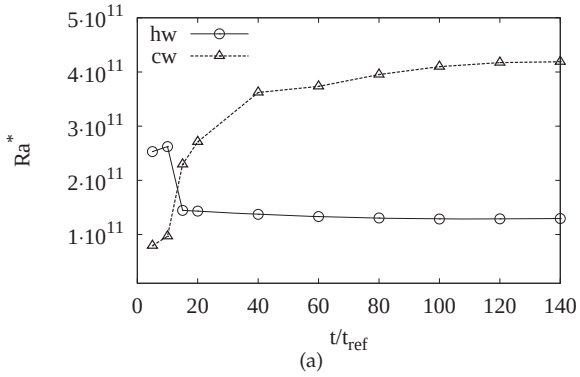

Figure 3.20: Equivalent Rayleigh number, Ra^*, according to Eq. 3.8 for both hot and cold wall upstream locations considering NOB.

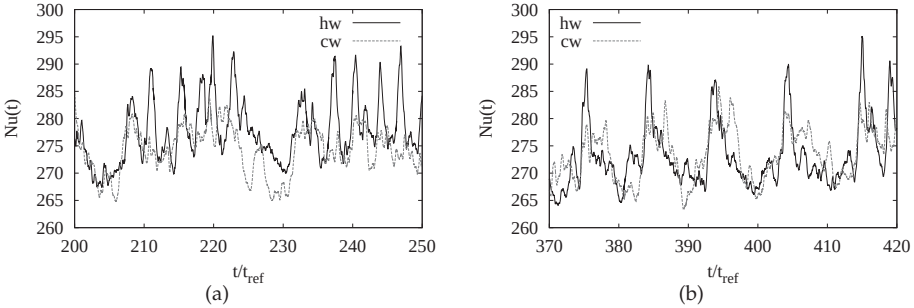

Figure 3.21: Time evolution of the instantaneous Nusselt number in the hot and cold walls for NOB case during (a) $200 \leq t/t_{ref} \leq 250$, (b) $370 \leq t/t_{ref} \leq 420$.

Table 3.4: Nusselt numbers, transition locations, and stratification at the center of the cavity for the actual 3D flow and 2D simulations. For NOB cases, the stratification peak value at the shifted location is provided in bolt.

Case	Nu	$x_{tr,h}/H$	$x_{tr,c}/H$	stratification
3D NOB	273.8	0.68	0.46	0.94(**1.32**)
3D OB	283.0	0.57	0.57	2.57
2D NOB	269.0	0.71	0.42	0.36(**2.52**)
2D OB	279.2	0.57	0.57	2.40

order statistics will be provided in the following sections.

2D vs. 3D NOB effects

Although turbulence is a three-dimensional phenomenon, in a previous study [6] NOB effects were studied by means of 2D DNS computations. In that study, although 2D assumption was not expected to predict properly the actual flow structures -especially in turbulent regions-, the methodology was used to identify the NOB effects when the temperature difference departs from the so-called OB regime. It was concluded that important effects were present, especially for temperature differences larger than 30 °C. Particularly, it was observed that the stratification zone, although shifted towards the top of the cavity was present at all the tested temperature differences. However, from the isotherms depicted in Figure 3.8, NOB effects actually degrade the stratification zone. It might be *a priori* argued that the conditions of the present numerical experiments are different from the previous studies, as temperature difference and aspect ratio are larger in the current simulations. Therefore, to shed more light into the present discussion of 2D vs. 3D NOB effects, a set of 2D simulations for OB and NOB using the same conditions as those employed in the present 3D study have been performed. It has been detected that, for the present flow parameters under 2D assumption, the stratification zone survives in both OB and NOB cases (see Figures 3.22 and 3.23). Indeed, one of the most relevant NOB effects seems to be related with the degradation of the stratification zone and an enhancement of the three-dimensionality of the flow, especially close to the transition to turbulence location. These effects, however, can not be captured by the 2D assumption. Thus, the present study concludes that in order to capture the NOB effects, 3D simulations have to be performed.

The data corresponding to the present discussion is summarized in Table 3.4, where Nusselt number, transition locations on both vertical boundary layers, and

(a) $\tau \approx 487$ (b) $\tau \approx 488$ (c) $\tau \approx 489$ (d) $\tau \approx 490$ (e) $\tau \approx 491$

Figure 3.22: A sequence of instantaneous isotherms separated by one dimensionless time unit using OB approximation considering two-dimensional flow.

(a) $\tau \approx 521$ (b) $\tau \approx 522$ (c) $\tau \approx 523$ (d) $\tau \approx 524$ (e) $\tau \approx 525$

Figure 3.23: A sequence of instantaneous isotherms separated by one dimensionless time unit considering NOB effects for 2D flow assumption.

stratification number are given for the studied cases. The results conclude the three-dimensionality of the NOB effects, as is indicated by the transition locations and stratification. However, it is interesting to note that 2D hypothesis might be a valid approximation in general terms for OB, considering the similarity of the results obtained for both the transition locations and the stratification phenomenon with respect to the corresponding 3D data.

3.4.2 Topology of the flow

The time-averaged statistics of the flow are presented in this section. In Figure 3.24, non-dimensional temperature, $\Phi = (T - T_c)/(T_h - T_c)$, and streamwise velocity component, $V = v/v_{ref}$, are depicted at different locations to identify the NOB effects by means of first-order flow statistics. In the midheight of the cavity, $y/H = 0.5$, the symmetric OB case presents pronounced peaks, which is partly mimicked by the NOB solution only in the vicinity of the hot wall. These peaks reveal that the flow is laminar at that location in the hot wall boundary layer, which effectively is observed during the study of the instantaneous flow. In the core region, the temperatures coincide, which is in contrast with a previous tall DHC study [6] that uses similar parameters, but considers two-dimensional flow. As for the streamwise velocity, the NOB clearly has a non-symmetric profile. In the hot wall, the velocity is about 20 % higher with respect to the OB result, which is in accordance with the downstream transition. However, in the cold wall, the maximum velocity is less than 50% of the OB result, which is attributed to the upward shift in the transition location, as it thickens the boundary layer, thus the streamwise velocity component is reduced. At $y/H = 0.7$, it can be observed that the core of the cavity is considerably warmer if NOB effects are considered. This is indeed visible in Figure 3.24(e) where the vertical temperature profile is displayed. Note that, except for a small region above the mid-height of the cavity, NOB effects result in warmer cavity core in the whole domain, which is one of the most relevant NOB effects observed and analyzed in the present study.

In Figure 3.25, some turbulent statistics, namely the turbulent kinetic energy, $\langle k \rangle$, temperature fluctuations, and the turbulent heat flux, $\langle V'\Phi' \rangle$, are presented at the same locations. Indeed, the discrepancies even in the first-order statistics anticipate important differences in the turbulent statistics. Note that if NOB effects are not taken into consideration, the instabilities are tiny in the midheight of the cavity, not generating important second-order statistics in temperature and velocity components. At $y/H = 0.7$ profile, in the vicinity of the hot wall, the turbulent statistics provide qualitatively similar results, with the exception of dissimilar fluctuation intensities in agreement with slightly different transition location. Note, however, that the turbulent heat flux has negative values in the outer part of the boundary layer when the NOB effects are considered. In the cold wall, at this location, OB approxi-

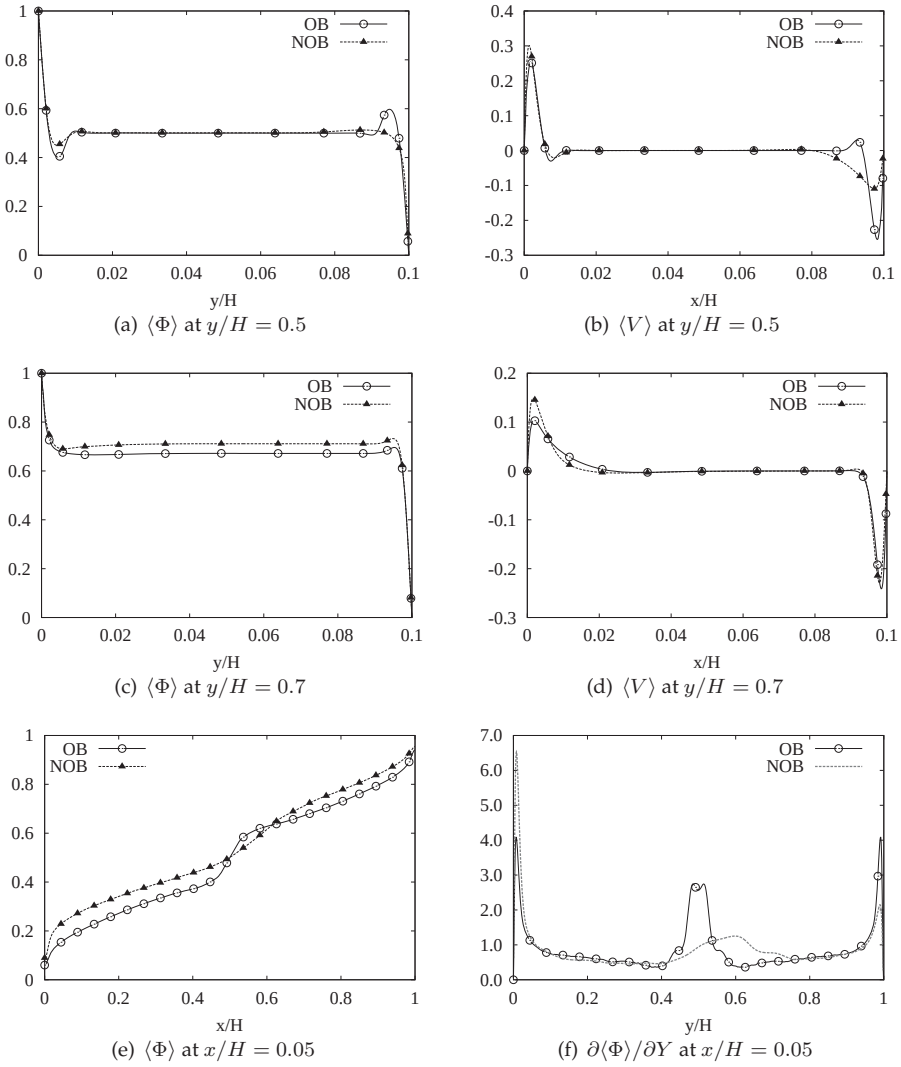

(a) $\langle\Phi\rangle$ at $y/H = 0.5$ (b) $\langle V\rangle$ at $y/H = 0.5$

(c) $\langle\Phi\rangle$ at $y/H = 0.7$ (d) $\langle V\rangle$ at $y/H = 0.7$

(e) $\langle\Phi\rangle$ at $x/H = 0.05$ (f) $\partial\langle\Phi\rangle/\partial Y$ at $x/H = 0.05$

Figure 3.24: First-order temperature and streamwise velocity statistics for NOB and OB.

mation does not produce any turbulent statistics as expected, while the NOB effects are manifest in form of preliminary noticeable fluctuations.

3.4.3 Boundary layer analysis

The analysis of the vertical boundary layers is essential in understanding the physics of the present flow configuration, since this dissimilar behavior gives rise to important effects which make the dynamics of the flow depart from those observed under the so-called OB regime. Note that in this water-filled cavity, the thermal boundary layer is expected to be thinner than the viscous boundary layer, as these are approximated *a priori* by the expression $\delta_v \approx Pr^{0.5}\delta_T$ (See [7] for details). In order to refer to the present boundary analysis, a scheme of the boundary layer referred to the actual flow is presented in Figure 3.26. Note that the inner viscous boundary layer is defined as location where the local streamwise velocity peaks. This is the sub-boundary layer where the highest velocity gradients are observed. The limit of the thermal boundary layer is assumed to be the location in which the temperature approaches asymptotically to the cavity core temperature at the corresponding height. Note here that, the diagram used in Figure 3.26 is one representing a location where the descending flow in the outer part of the boundary layer results in a region of lower temperature below that of the corresponding core. Finally, it should be noted that, due to the Pr number adopted in this study, the viscous diffusion is larger than the thermal diffusion, which results in a larger viscous boundary layer. Similar to the thermal boundary layer, the viscous boundary layer limit is adopted as the location where the streamwise velocity approaches to zero.

The inner viscous and viscous boundary layers are comparatively presented in Figure 3.27. Note that the inner viscous boundary layer is found considerably thicker on the cold wall, with a factor of approximately 2, with respect to the hot wall. This behavior can be partly attributed to the temperature dependance of the viscosity which has approximately 4 times larger values in the cold wall when compared with the hot wall. Thus viscous effects penetrate well within the core of the cavity, resulting in a larger portion with significant viscous effects. As for the viscous boundary layer, δ_{vis}, the differences between the hot and cold wall boundary layer thicknesses are relatively reduced in the downstream portion of the boundary layer, which can be explained with the fact that flows in both boundaries are already turbulent, and the confined -by the horizontal walls- and ordered flow with quasi-motionless core represents a natural limit to avoid further growth of this layer. However, in the mid-height of the cavity, in the absence of the horizontal boundaries, an approximately two-times thicker cold wall viscous boundary is still visible. Notice that close to the corners of the cavity, the viscous boundary layer thickness trends are reverted, which can be due to the turbulence mixing effect taking place at these locations.

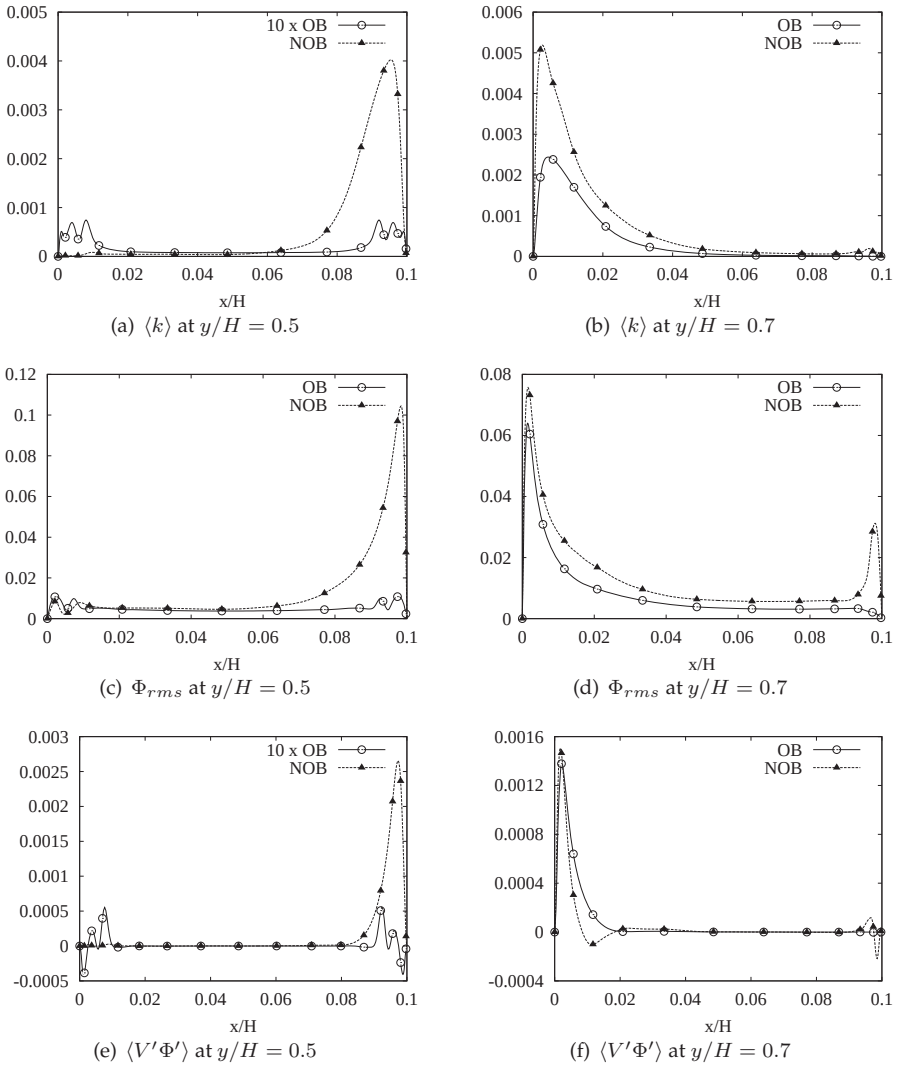

(a) $\langle k \rangle$ at $y/H = 0.5$

(b) $\langle k \rangle$ at $y/H = 0.7$

(c) Φ_{rms} at $y/H = 0.5$

(d) Φ_{rms} at $y/H = 0.7$

(e) $\langle V'\Phi' \rangle$ at $y/H = 0.5$

(f) $\langle V'\Phi' \rangle$ at $y/H = 0.7$

Figure 3.25: Profiles of turbulent statistics at different locations for NOB and OB.

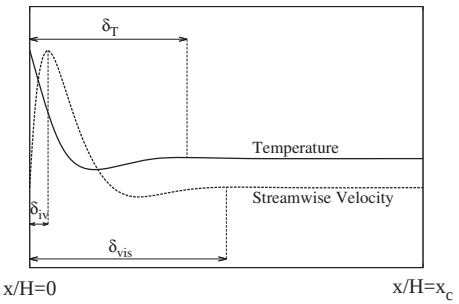

Figure 3.26: A scheme of the viscous, δ_{vis}, inner viscous, δ_{iv}, and thermal boundary layers,δ_T, as adopted in the present study.

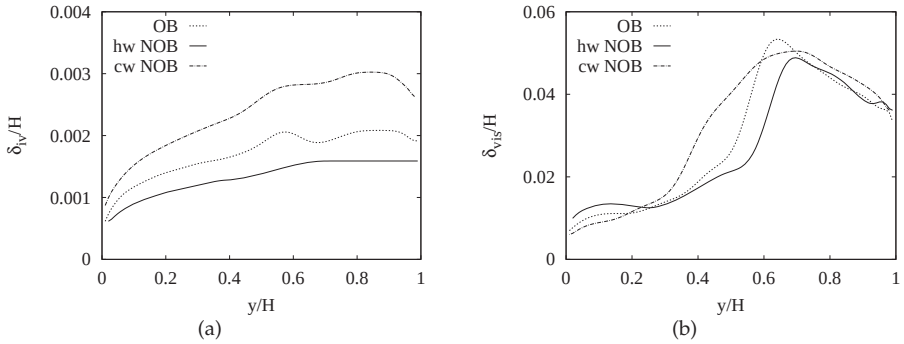

Figure 3.27: Inner viscous boundary layer limit (a) and viscous boundary layer thickness (b) for OB and NOB.

In Figures 3.28 and 3.29, temperature and velocity profiles are highlighted in the vicinity of the vertical boundaries. In these figures, except for a close distance from the wall, velocity profiles both for OB and NOB cases seem not to follow the wall of the law. However, the temperature profiles follow the law of the wall for the zone $x^+ \leq 5$ as in the forced convection boundary layers. This is in line with the findings of other authors [28].

3.4.4 Heat transfer analysis

One important consideration in the present study is the influence of the NOB effects on the heat transfer. To that end, time-averaged Nusselt number and its standard deviation is depicted in Figure 3.30. Notice that the maxima of the standard deviation of the Nusselt number is representative of the transition location. Considering this, the figure indicates that for OB approximation, the transition takes place at $y_{tr,OB}/H = 0.57$ at the hot wall, and in the symmetric location at the cold wall. For the NOB case, however, the transition location in the hot and cold wall from the leading edge is found as $y_{tr,NOB,h}/H = 0.68$, and $y_{tr,NOB,c}/H = 0.45$, respectively. In the boundary layer, before the transition takes place, the instabilities are slowly amplified, generating turbulent statistics. These can be deduced from Figure 3.30b, where at some location before transition, the standard deviation of the Nusselt number starts to increase with respect to the quasi-constant upstream value. This location can be denominated as the location of the onset of turbulence, x_o. In agreement with the previous analysis of the instantaneous flow, one of the observed NOB effects in this flow configuration is the significant oscillation of the transition location. Thus, although the onset of turbulence mainly coincides for OB and NOB cases, NOB transition -peak value of the standard deviation of Nu- takes place at a more downstream location. This oscillation is thought to be a consequence of the active interaction between the both boundary layers, as is manifest from the onset of transition locations. Remember that the flow configuration in the absence of the NOB effects resulted in a central highly stratified region, which in a way acts as a stable barrier, avoiding thus an overlapping region which receive high energy eddies from both boundary layers simultaneously. However, this is no longer true when the NOB effects are involved. Indeed, if the onset of transition location is conveniently defined as the location where the standard deviation of the Nusselt number exceeds 5% of the corresponding wall maxima value, then $x_{o,NOB,h} \approx 0.5$ and $x_{o,NOB,c} \approx 0.25$, which can mean that in the region $0.5 \leq y/H \leq 0.75$, the vortices are ejected from both sides to the core of the cavity, finally resulting in a more complex flow configuration. This interaction may explain the vertical oscillations in the both boundary layer transition locations.

Global average Nusselt numbers are calculated as $Nu_{OB} = 283.0$ and $Nu_{NOB} = 273.8$ for OB and NOB cases, respectively. Thus, if NOB effects are not considered,

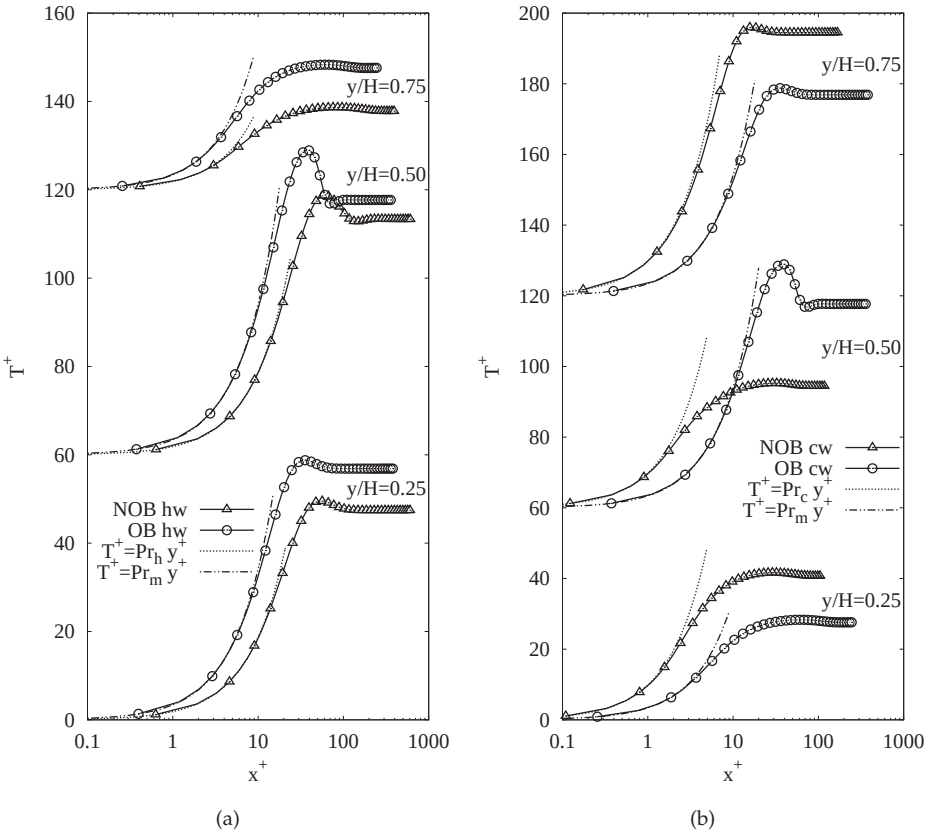

Figure 3.28: Temperature profiles near the hot (a) and cold (b) wall boundary layers for different cavity heights. The graphs are shifted by 60 temperature units.

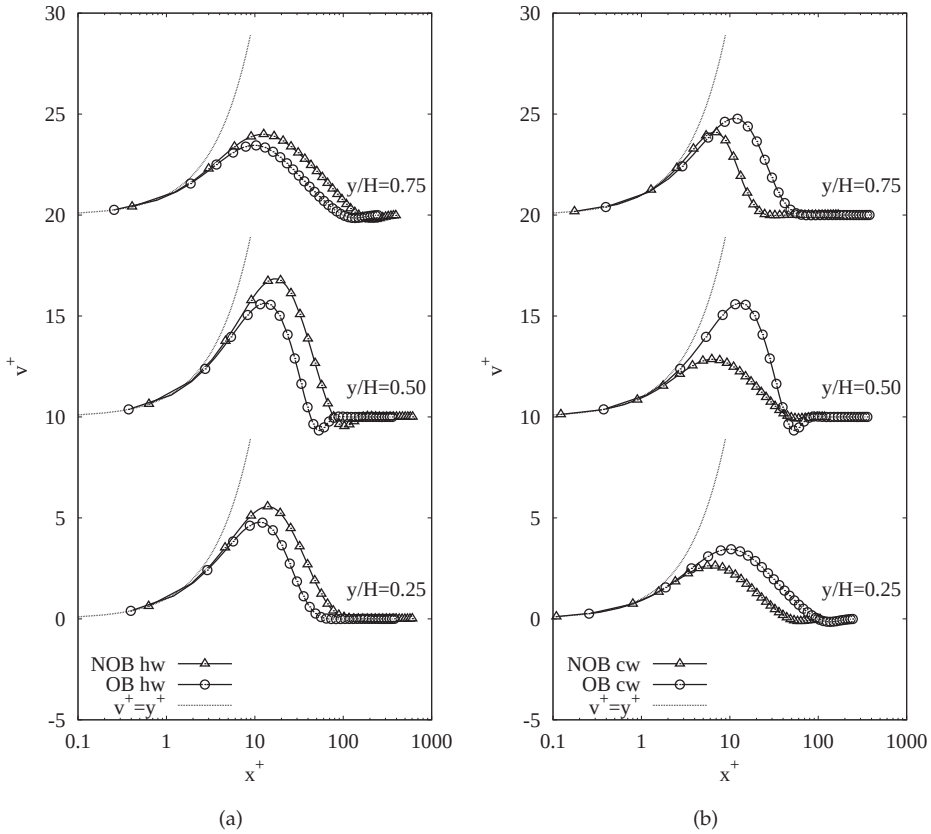

Figure 3.29: Velocity profiles near the hot (a) and cold (b) wall boundary layers for different cavity heights. The graphs are shifted by 10 velocity units.

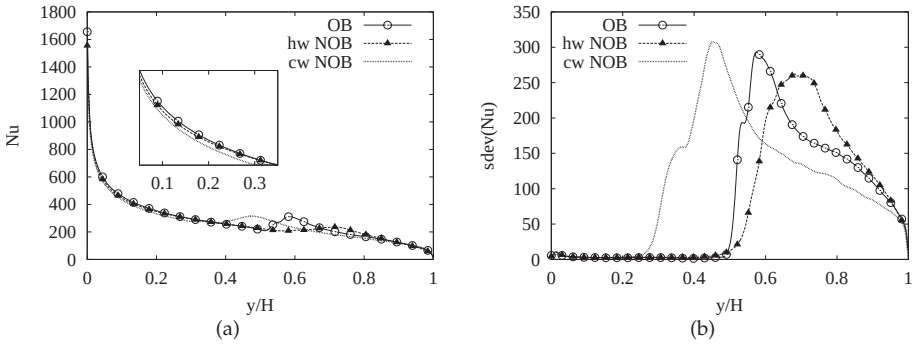

Figure 3.30: Time-averaged Nusselt number (a) and its standard deviation (b) for NOB and OB cases.

the heat transfer can be overpredicted by about 3 % for this configuration. It can be concluded that, although important NOB effects are identified as the dynamics of the flow is concerned, the influence of these on the heat transfer does not happen to be significant due probably to the damping effect which may take place as the boundaries interact. Note that, in the previous two-dimensional study on the NOB effects [6], the consideration of these enhances the heat transfer unlike the present finding. In that study, however, the interaction of the two boundary layers results in a highly stratified region, similar to the one that can be observed in Figure 3.8 for the OB case.

The analysis of the local averaged Nu shows that on upstream locations where the flow is essentially laminar, the Nusselt curve follows a similar trend for both hot and cold walls. To further highlight this, a detail of the curve is provided in Figure 3.30(a), where the hot wall curve registers slightly higher values in comparison with the cold wall. In the initial phases of the simulation, when the flow is governed by the laminar regime, a higher heat transfer is expected to take place in the hot wall boundary layer due to higher equivalent Rayleigh number value at the hot wall temperature. This fact could gradually heat the cavity up to a level where a balance in the heating and cooling power of the both boundaries is reached, and this balance is expected to occur at cavity core temperatures higher than those for an equivalent OB case due to higher (lower) intensity of the convection heat transfer in the hot (cold) wall during the initial phase of the flow. This is effectively the case as we can confirm in the present study. Under the effect of the buoyancy, the warm fluid ascends, emphasizing a warmer cavity especially in the upper core. This warmer fluid then entrains the cold wall boundary, which gives rise to upstream transition due to higher equivalent Rayleigh number, thus higher intensity of the natural convection driving

force. When the balance is reached, the local Nu numbers take the form as shown in Figure 3.30(a). The relevant data regarding the heat transfer analysis is briefly summarized in Table 3.4. Note that, as explained earlier, the stratification number for NOB gives a value lower than unity, as is anticipated in the ongoing analysis. In parenthesis the local peak value is provided which is observed at $y/H \approx 0.61$.

3.5 Conclusions

The NOB effects in a tall water-filled differentially heated cavity are analyzed by means of direct numerical simulation. The obtained results reveal significant NOB effects for this configuration, due to the dissimilar flow behavior in the vertical boundary layers, which result in downstream transition in the hot wall and upstream transition in the cold wall with respect to the OB approximation, breaking the symmetry of the flow. The transition to turbulence phenomenon on both vertical boundary layers are investigated when NOB effects are present: The mechanism of the transition, the nature of the 2D structures and their breakdown into three-dimensional structures have been observed to occur in an equivalent manner with respect to OB approximation. Due to the variable thermophysical properties, a relatively warmer cavity is observed with the inclusion of the NOB effects, as in the initial phases of the flow, hot wall boundary layer has an enhanced heating power if compared with the cold wall cooling power. As a consequence, this leads to a warmer upper core for the cavity. As the time further advances, the strength of the natural convection flow gradually decreases and increases in the hot and cold wall boundary layers, respectively, due to the effect of the variable heat transfer properties of the feeding flow that originate from the stratified core. This explains the premature transition in the cold wall boundary layer. The interaction between the both boundary layers is thought to give rise to important vertical oscillations as the transition locations are concerned. Eventually this fact ends up with the existence of a large overlapping region which receives the simultaneous ejecting of large vortical structures from both sides, thus avoiding the formation of a highly stratified zone. It has been also shown that the 2D assumption is unable to represent even qualitatively the actual NOB effects, due to not being able to capture the mentioned degradation in the stratification value. This degradation finally results in slightly lower Nusselt number, which again is in disagreement with the previous works on the NOB effects ignoring the three-dimensionality of the flow. The analysis is complemented with the presentation of the results on the topology of the flow, and an analysis of the vertical boundary layers considering NOB effects.

References

[1] J. Salat, S. Xin, P. Joubert, A. Sergent, F. Penot, P. Le Quere, Experimental and numerical investigation of turbulent natural convection in large air-filled cavity, International Journal of Heat and Fluid Flow 25 (2004) 824–832.

[2] F. X. Trias, M. Soria, C. D. Pérez-Segarra, A. Oliva, Direct Numerical simulations of two and three dimensional turbulent natural convection flows in a differentialy heated cavity of aspect ratio 4, Journal of Fluid Mechanics 586 (2007) 259–293.

[3] F. X. Trias, A. Gorobets, M. Soria, A. Oliva, Direct numerical simulation of a differentially heated cavity of aspect ratio 4 with Rayleigh numbers up to 1E11 Part II: Heat transfer and flow dynamics, International Journal of Heat and Mass Transfer 53 (1) (2010) 674–683.

[4] P. Le Quéré, Transition to unsteady natural convection in a tall water-filled cavity, Physics of Fluids A 2 (1990) 503–515.

[5] P. J. A. Janssen, R. A. W. M. Henkes, Influence of Prandtl number on instability mechanisms and transition in a differentially heated square cavity, Journal of Fluid Mechanics 290 (1995) 319–344.

[6] D. Kizildag, I. Rodríguez, A. Oliva, O. Lehmkuhl, Limits of the Oberbeck-Boussinesq approximation in a tall differentially heated cavity filled with water, International Journal of Heat and Mass Transfer 68 (2014) 489–499.

[7] J. Patterson, J. Imberger, Unsteady natural convection in a rectangular cavity, Journal of Fluid Mechanics 100 (1) (1980) 65–86.

[8] D. Gray, A. Giorgini, The validity of the Boussinesq approximation for liquids and gases, International Journal of Heat and Mass Transfer 19 (1976) 545–551.

[9] G. Ahlers, E. Brown, F. F. Araujo, D. Funfschilling, S. Grossmann, D. Lohse, Non-Oberbeck-Boussinesq effects in strongly turbulent Rayleigh-Bénard convection, Journal of Fluid Mechanics 569 (2006) 409–445.

[10] K. Sugiyama, E. Calzavarini, S. Grossmann, D. Lohse, Flow organization in two-dimensional non-Oberbeck-Boussinesq Rayleigh-Bénard convection in water, Journal of Fluid Mechanics 637 (2009) 105.

[11] S. Horn, O. Shishkina, C. Wagner, On non-Oberbeck-Boussinesq effects in three-dimensional Rayleigh-Bénard convection in glycerol, Journal of Fluid Mechanics 724 (2013) 175–202.

[12] K. Sugiyama, E. Calzavarini, S. Grossmann, D. Lohse, Non-Oberbeck-Boussinesq effects in two-dimensional Rayleigh-Bénard convection in glycerol, Europhysics Letters (EPL) 80 (3) (2007) 34002.

[13] D. Kizildag, F. X. Trias, I. Rodríguez, A. Oliva, Large eddy and direct numerical simulations of a turbulent water-filled differentially heated cavity of aspect ratio 5, International Journal of Heat and Mass Transfer 77 (2014) 1084–1094.

[14] E. R. G. Eckert, R. M. Drake, Heat and Mass Transfer, McGrow-Hill, New York (1972).

[15] R. W. C. P. Verstappen, A. E. P. Veldman, Symmetry-preserving discretization of turbulent flow, Journal of Engineering Mathematics 187 (1) (2003) 343–368.

[16] F. X. Trias, A. Gorobets, A. Oliva, A simple approach to discretize the viscous term with spatially varying (eddy-)viscosity. *Journal of Computational Physics*, 253 (2013) 405–417.

[17] F. X. Trias, O. Lehmkuhl, A self-adaptive strategy for the time integration of Navier-Stokes equations, Numerical Heat Transfer, Part B 60 (2) (2011) 116–134.

[18] R. Borrell, O. Lehmkuhl, F. X. Trias, A. Oliva, Parallel direct Poisson solver for discretisations with one Fourier diagonalisable direction, *Journal of Computational Physics*, 230(12) (2011) 4723–4741.

[19] P. J. Roache, Code verification by the method of the manufactured solutions, Journal of Fluids Engineering 124(1) (2001) 4–10. doi:10.1115/1.1436090.

[20] D. G. Barhaghi, L. Davidson, Natural convection boundary layer in a 5:1 cavity, Physics of Fluids 19 (12) (2007) 125106–125106.

[21] J. C. R. Hunt, A. A. Wray, P. Moin, Eddies, stream and convergence zones in turbulent flows. *Tech. Rep.* CTR-88. Center for Turbulence Research (1988).

[22] A. Prasad, C. H. K. Williamson, The instability of the shear layer separating from a bluff body, Journal of Fluid Mechanics, 333, pp 375-402 doi:10.1017/S0022112096004326.

[23] G. K. Batchelor, Heat transfer by free convection across a closed cavity between vertical boundaries at different temperatures, Quart. App. Math., Vol. 12, p. 209. (1954)

[24] A. E. Gill, The boundary-layer regime for convection in a rectangular cavity, Journal of Fluid Mechanics, 26 (1966) pp 515-536 doi:10.1017/S0022112066001368.

[25] S. A. Korpela, D. Gozum, C. B. Baxi, On the stability of the conduction regime of natural convection in a vertical slot, International Journal of Heat and Mass Transfer, 16(9) (1973) pp 1883–1690 http://dx.doi.org/10.1016/0017-9310(73)90161-0.

[26] M. Manga, D. Weeraratne, S. J. S. Morris, Boundary-layer thickness and instabilities in Bénard convection of a liquid with a temperature-dependent viscosity, Physics of Fluids 13 (3) (2001) 802–805.

[27] N. Seki, S. Fukusako, H. Inaba, Heat Transfer of Natural Convection in a Rectangular Cavity with Vertical Walls of Different Temperatures, Bulletin of the JSME 21(152) (1978) pp 246–253, doi:10.1299/jsme1958.21.246.

[28] D. G. Barhaghi, L. Davidson, R. Karlsson, Large-eddy simulation of natural convection boundary layer on a vertical cylinder, International Journal of Heat and Fluid Flow 27 (5) (2006) 811–820.

Chapter 4

Large eddy and direct numerical simulations of a turbulent water-filled differentially heated cavity of aspect ratio 5

This chapter have been published as:

Kizildag, D., Trias, F. X., Rodríguez, I., & Oliva, A. (2014). Large eddy and direct numerical simulations of a turbulent water-filled differentially heated cavity of aspect ratio 5. International Journal of Heat and Mass Transfer, 77, 1084-1094. doi:10.1016/j.ijheatmasstransfer.2014.06.030

Abstract.

Natural convection in a differentially heated cavity is characterized by different phenomena such as laminar to turbulent flow transition in the boundary layer, turbulent mixing, and thermal stratification in the core of the cavity. In order to predict the thermal and fluid dynamic behavior of the flow in these cavities, the location of transition to turbulence should be accurately determined. In this work, the performance of three subgrid-scale (SGS) models is submitted to investigation in a water-filled cavity of aspect ratio 5 at Rayleigh number $Ra = 3 \times 10^{11}$. To do so, the models are compared with the solution obtained by means of direct numerical simulation. The models tested are: (i) the wall-adapting local-eddy viscosity (WALE) model, (ii) the QR model, (iii) the WALE model within a variational multiscale framework (VMS-WALE). It has been shown that the VMS-WALE and WALE models perform better in estimating the location of transition to turbulence, and thus their overall behavior is more accurate than the QR model. The results have also revealed that the use of SGS models is justified in this flow as the transition location and consequently the flow structure cannot be captured properly if no model is used for the tested spatial resolution.

4.1 Introduction

The flow in a differentially heated cavity (DHC) has been studied extensively in the literature, due to its relevance to model many applications of industrial interest, like air flow in buildings, heat transfer in solar collectors, or cooling of electronic devices. The flow is characterized by a thermal gradient which is orthogonal to the gravitational field. In accordance with the available computing power, first efforts mainly addressed steady laminar two-dimensional flows (see for instance [1]). In the last two decades, more demanding two- and three-dimensional transitional and turbulent flows appeared in the literature thanks to the increasing computational resources, which allowed dealing with different scales of motion present in such flows at moderate and high Rayleigh numbers (Ra) [2, 3, 4, 5]. Although the geometry is rather simple, different regimes coexist when the Rayleigh number is increased beyond a critical value: i) laminar flow in the upstream part of the vertical boundary layers and in the core of the cavity, ii) transitional and turbulent flow at some location where the downstream traveling waves grow sufficiently to disrupt the vertical boundary layer and eject large unsteady eddies. In the core of the cavity, a thermally stratified zone is expected. Even though at relatively smaller velocities compared with the vertical boundary layer, the core is in motion, as the isotherms oscillate around a mean horizontal profile, which can be attributed to the internal gravity waves. Although conducting direct numerical simulation (DNS) in real-scale engineering problems is not feasible yet, the present configuration, being a canonical case, has been subject of DNS studies on moderate Rayleigh numbers [6, 7, 8]. These works have contributed to understand the physical phenomena of turbulence and provided useful data.

The vast majority of the performed studies consider air-filled cavities (Prandtl number $Pr \approx 0.7$). However, the working fluid is water for many buoyancy-driven applications. In the case of a water-filled cavity, i.e. greater Prandtl number compared with air, obtaining solutions for the governing equations gets more complicated since the thermal boundary layer becomes thinner for the same Rayleigh number [9]. Therefore, finer grids are required to capture the smallest scales of the flow. This may be one of the reasons explaining that numerical studies of water-filled DHC are quite scarce when compared with air-filled ones and are generally limited to a two-dimensional domain [10, 11, 12]. Alternatively, large eddy simulations (LES) are an encouraging alternative for the resolution of turbulent natural convection in these cavities as they model the smallest scales of flow while the large scales are solved. The selection of an appropriate subgrid-scale (SGS) stresses model for describing the complex flow behavior is crucial in this cavity flow, where the overall performance of the model is dependent on the accurate prediction of the transition to turbulence phenomenon.

With regard to the use of LES models in DHC flows, several authors published

relevant contributions for the air-filled cavities. Peng and Davidson [13] studied a flow with a low level of turbulence ($Ra = 1.58 \times 10^9$) in a cubical cavity. They obtained good results in the main flow quantities by using approximately 0.6 million control volumes (CV). On the other hand, second-order turbulent statistics showed discrepancies with the reference experimental work, due mainly to the lower resolution of the grid in the outer shear layer and the spanwise direction.

In the recent years, different studies of LES on a DHC configuration of aspect ratio 5 appeared in the literature. Barhaghi and Davidson [14] studied a turbulent DHC of aspect ratio 5 at $Ra = 4.028 \times 10^8$ (based on the cavity width) by means of the Smagorinsky [15], the dynamic eddy-viscosity [16], and the wall-adapting local-eddy viscosity (WALE) [17] models. The finest mesh they employed had approximately 2.5 million CVs. The tested SGS models gave substantially different results in capturing the location of transition in the vertical boundary layer, with the dynamic eddy viscosity model the most accurate one. They performed a full analysis of turbulent statistics in both transitional and turbulent regions of the cavity. They indicated that the results in the transition region showed considerable differences between the coarse and fine meshes, while in the fully turbulent region the grid dependency was no longer important.

More recently, two works for very similar Rayleigh numbers were carried out using the same aspect ratio. Lau et al. [18] tested different SGS models in an air-filled DHC of aspect ratio 5 at $Ra = 4.56 \times 10^{10}$ using approximately 2.1 million CVs. The comparison with the available experimental data demonstrated that the transition to turbulence cannot be well captured if the models are too dissipative, thus leading to important discrepancies with the reference data. Trias et al. [19] studied a turbulent DHC flow of aspect ratio 5 by means of DNS and regularization modeling for $Ra = 4.5 \times 10^{10}$. For the modeling of turbulence they used a novel class of regularization that restrain the convective production of small scales of motion in an unconditionally stable manner. The comparison of the results showed that the method was able to capture the general patterns of flow even for very coarse meshes, illustrating the potential of the regularization method to deal with complex flows.

Ghaisas et al. [20] tested different SGS models for weakly turbulent flow in a DHC of aspect ratio 4 for two different Rayleigh numbers, obtaining good agreement with the available DNS data for $Ra = 6.4 \times 10^8$, although higher mesh resolution was shown to be needed when the Rayleigh number was raised to 2.0×10^9.

Sergent et al. [21] recently used LES to show that the discrepancies between the numerical and experimental stratification values in the center of the air-filled DHC is due to the contribution of the front and rear end walls in heat transfer and fluid flow.

The conducted studies so far showed that the accurate assessment of the transition location is essential in predicting flow configuration in a turbulent DHC flow.

As a result, the performance of the SGS models are primarily dependent on their capability to capture this location. Considering this, the present work aims at testing the performance of three SGS models for the turbulent natural convection flow in a water-filled DHC of aspect ratio 5 at $Ra = 3 \times 10^{11}$. The tested models are: (i) the WALE model [17], (ii) the QR model [22], and (iii) the WALE model within a variational multiscale framework [23] (VMS-WALE). In the literature, for the DHC configuration, the numerical investigations of LES are concentrated on the air-filled cavities. Thus, the current study is intended to fill a gap, providing DNS and LES results for moderate-to-high Rayleigh numbers in three-dimensional water-filled cavities. Moreover, to the best knowledge of the authors, this is the first study to test the QR model in a DHC configuration.

The remainder of the present paper is organized as follows. In the next section, the description of the case is presented. Then, Section 3 is devoted to the DNS: the numerical methodology used is outlined and the details of the verification studies are explained. In Section 4, the LES models tested in the study are briefly described. In Section 5, the performance of the LES models is assessed by comparison with the DNS results. The discussion is focused on the prediction of the transition to turbulence location and its influence on the flow structure and heat transfer. Finally, concluding remarks are given in Section 6.

4.2 Description of the case

The turbulent natural convection in a three dimensional DHC of height H, width W, and depth D is submitted to investigation (see Figure 4.1). The aspect ratio is $H/W = 5$. This aspect ratio was studied previously by different authors [14, 24, 19, 18]. The cavity is subjected to heating along the left vertical wall, and cooling along the right vertical wall by means of isothermal confining walls at T_h and T_c, respectively. The cavity height based Rayleigh number ($Ra = g\beta\left(T_h - T_c\right) H^3 Pr/\nu^2$) is 3×10^{11}, where g is the gravity, β is the thermal expansion coefficient, and ν is the kinematic viscosity. The Prandtl number ($Pr = \nu/\alpha$) in this water-filled DHC is 4.31, which corresponds to water at $40\ ^\circ C$, where α is the thermal diffusivity. The confining walls at the top and bottom of the cavity are adiabatic. No-slip velocity condition is imposed on these four boundaries in x- and y-directions, whereas periodic boundary conditions are imposed in the z-direction for all the variables.

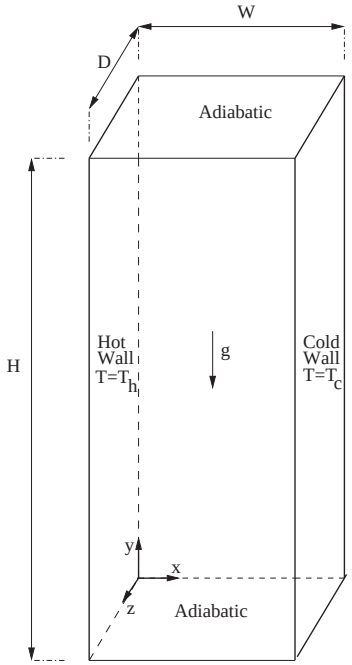

Figure 4.1: Schema of the three-dimensional DHC.

4.3 DNS

4.3.1 Governing equations

Considering an incompressible viscous Newtonian fluid, assuming the Oberbeck-Boussinesq (OB) approximation, and neglecting thermal radiation, the governing equations read,

$$\nabla \cdot \mathbf{u} = 0 \tag{4.1}$$

$$\frac{\partial \mathbf{u}}{\partial t} + (\mathbf{u} \cdot \nabla)\mathbf{u} - \nu \nabla^2 \mathbf{u} + \nabla p + \mathcal{F} = \mathbf{0} \tag{4.2}$$

$$\frac{\partial T}{\partial t} + (\mathbf{u} \cdot \nabla)T - \alpha \nabla^2 T = 0 \tag{4.3}$$

where $\mathbf{u} = (u, v, w)$ is the velocity vector, p and T are the kinematic pressure and

temperature fields, respectively. $\mathcal{F}$ is the body force $\mathcal{F} = \beta(T - T_m)\mathbf{g}$, with $T_m = (T_h + T_c)/2$ the mean temperature, and $\mathbf{g} = (0, -g, 0)$ the gravitational acceleration vector.

For the presentation of the dimensionless results, the adopted reference length, time, velocity, and temperature are $L_{ref} = H$, $t_{ref} = (H^2/\alpha)Ra^{-0.5}$, $u_{ref} = (\alpha/H)Ra^{0.5}$, and $\Delta T_{ref} = (T_h - T_c)$, respectively.

4.3.2 Numerical methods for DNS

The incompressible Navier-Stokes equations (4.1)-(4.2) are discretized on a staggered Cartesian grid by a fourth-order symmetry-preserving numerical scheme [25], representing the convective term by a skew-symmetric, and the diffusive term by a symmetric positive-definite matrices. The resulting operator-based finite-volume discretization of equations (4.1)-(4.2) for the temporal evolution of the spatially discrete staggered velocity vector $\mathbf{u}_s$ yields,

$$M\mathbf{u}_s = \mathbf{0}_c \tag{4.4}$$

$$\Omega\frac{d\mathbf{u}_s}{dt} + C\left(\mathbf{u}_s\right)\mathbf{u}_s + D\mathbf{u}_s - M^T\mathbf{p}_c = \mathbf{0}_s \tag{4.5}$$

where the subindices c and s refer to cell-centered and staggered discrete variables, respectively. The diffusive matrix, D, is symmetric and positive semi-definite, representing the integral of the diffusive flux $-\nu\nabla\mathbf{u}\cdot\mathbf{n}$ through the CV faces, where $\mathbf{n}$ is the unit vector normal to the CV face. The diagonal matrix, Ω, stands for the sizes of the control volumes and the approximate convective flux is discretized as in [25]. The resulting convective matrix, $C(\mathbf{u}_s)$, is skew-symmetric. Then, in the absence of body forces, the time evolution of the discrete kinetic energy $\|\mathbf{u}_s\|^2 = \mathbf{u}_s \cdot \Omega\mathbf{u}_s$ is governed by,

$$\frac{d}{dt}\|\mathbf{u}_s\|^2 = -\mathbf{u}_s \cdot \left(D + D^T\right)\mathbf{u}_s < 0 \tag{4.6}$$

where the convective and pressure gradient contributions cancel because of the skew-symmetry of the convective term and the incompressibility constraint of Equation (4.4), respectively. Therefore, even for coarse grids, the energy of the resolved scales of motion is convected in a stable manner, *i.e.* the discrete convective operator transports energy from a resolved scale of motion to other resolved scales without introducing any artificial dissipation of energy. The cell-centered temperature is discretized in a similar manner. For details, the reader is referred to [25].

For the temporal discretization, a second-order explicit one-leg scheme [26] is used by means of the classical fractional step projection method. A predictor velocity, $\mathbf{u}_s^p$, is explicitly evaluated without considering the contribution of the pressure

gradient. Then, by imposing the incompressibility constraint, $M\mathbf{u}_s^{n+1} = \mathbf{0}_s$, it leads to a Poisson equation for $\mathbf{p}_c^{n+1}$ to be solved once each time-step,

$$-M\Omega^{-1}M^T\mathbf{p}_c^{n+1} = M\mathbf{u}_s^p \tag{4.7}$$

For the details of the numerical algorithms and the Poisson solver, the reader is referred to [7].

4.3.3 Verification of the DNS

The DNS code was verified using the Method of Manufactured Solutions (MMS) [27], and tested for several benchmark reference results (see for instance [7]). Moreover, since the spatial discretization is fully-conservative, the exact fulfillment of the global kinetic energy balance was also used as an additional verification. Regarding the simulations, sufficiently fine grid resolution in space and time is required in order to resolve all the relevant turbulent scales, whereas the periodic z-direction should be large enough to contain the largest scales of the flow. Furthermore, the flow statistics should be integrated for a time span long enough to evaluate them properly. Note, however, that a compromise between accuracy and the cost of the calculations has to be adopted.

In the present DNS, the flow is initially at rest with a random perturbation of the initial temperature field to trigger three-dimensionality. The flow statistics are averaged over the three statistically invariant transformations: time, spanwise direction, and central-point symmetry. This averaging is denoted as $< \cdot >$. The total simulation period is 600 time units, where the last 200 time units are used for the flow statistics. Three meshes are used for the grid study. The numerical parameters of the simulations are given in Table 4.1. Grid spacing in the streamwise and spanwise directions is chosen uniform, while for the wall-normal direction, the following hyperbolic-tangent function is used:

$$x_i/H = \frac{W}{2H}\left(1 + \frac{tanh\left[\gamma_x\left(2(i-1)/N_x - 1\right)\right]}{tanh\gamma_x}\right) \qquad i = 1, 2, ..., N_x + 1 \tag{4.8}$$

where x_i indicates the location of the control volume face, γ_x is the mesh concentration factor and N_x is the number of CVs in the wall-normal direction.

Spanwise two-point correlation, $R_{\phi\phi}$, defined as

$$R_{\phi\phi}(x, y, \delta z) = \frac{< \phi'(x, y, z)\phi'(x, y, z + \delta z) >}{< \phi'^2(x, y, z) >} \tag{4.9}$$

with ϕ' the fluctuation of the variable ϕ ($\phi' = \phi - < \phi >$), is used to check the adequacy of the computational domain in the periodic direction. In this regard, two

Case	N_x	N_y	N_z	$N_{tot} \times 10^{-6}$	D/H	γ_x	$(\Delta x)_{\min}/H$	$\Delta t/t_{ref}$
Mesh A	240	648	128	19.91	0.1	2.0	6.20×10^{-5}	2.71×10^{-4}
Mesh B1	160	432	128	8.85	0.1	2.0	9.38×10^{-5}	8.06×10^{-4}
Mesh B2	160	432	256	17.69	0.2	2.0	9.38×10^{-5}	8.06×10^{-4}

Table 4.1: Numerical simulation parameters for DNS. N_x, N_y, and N_z are the number of CVs in wall-normal, streamwise, and spanwise directions, respectively. N_{tot} is the number of total CVs, $(\Delta x)_{min}$ is the smallest wall-normal distance, γ_x is the mesh concentration factor, and Δt is the average time-step.

meshes, Mesh B1 and Mesh B2, are considered. Note that these grids only differ in the length of the domain in the periodic direction, as Mesh B2 has twice larger domain than Mesh B1. In Figure 4.2, the correlation values are plotted using the spanwise velocity component, w, at six monitoring points for these meshes. In all the monitoring points, the correlations fall off to approximately zero at separations of one half-period even for the narrower Mesh B1, showing that this computational domain length in the spanwise direction ($D/H = 0.1$) is sufficiently large. It should be pointed out that, for the narrower mesh, the correlations drop only approximately to zero for some monitoring points. However, given the similarity of the two-point correlation values for both meshes, the choice of the narrower domain is only expected to alter the size of the largest structures in a small degree, which in turn should not affect the first- and second-order statistics significantly, as was shown in [28]. Although not shown here, similar results are obtained for other monitoring points and variables.

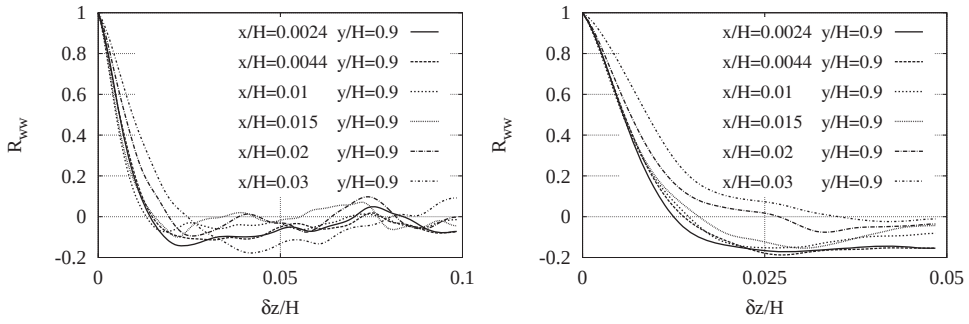

Figure 4.2: Two-point correlations of the spanwise velocity, w, at six monitoring locations for Mesh B2 (left) and Mesh B1 (right).

When constructing the mesh, the proper resolution of the boundary layer should be guaranteed. Based on the periodic direction domain size of Mesh B1, Mesh A improves considerably the grid resolution in the wall-normal and streamwise directions. Figure 4.3 displays the location of the first grid point in wall-units, $(\Delta x)^+ = u_\tau(\Delta x)_{min}/\nu$, for Mesh A, where u_τ is the friction velocity, $u_\tau = (\tau_w/\rho)^{1/2}$, and τ_w is the wall friction, $\tau_w = \rho\nu\partial v/\partial x$. Note that $(\Delta x)^+$ falls down to values smaller than unity, indicating sufficient resolution in the wall-normal direction.

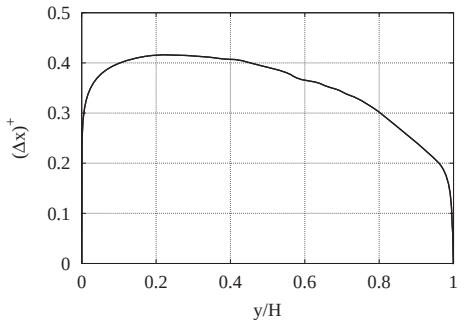

Figure 4.3: Location of the first grid point in wall-units for Mesh A.

In order to ensure that the smallest relevant scales are well-resolved, the grid resolution in the spanwise direction has to be adjusted. To that end, one-dimensional energy spectra of the spanwise velocity component, $E_{ww}(x, y, k_z) = \hat{w}_{k_z}(x, y)\hat{w}^*_{k_z}(x, y)$, at six different monitoring points have been checked for the suitability of the numerical simulation parameters in the z-direction using Mesh A, where $(\cdot)^*$ represents the complex conjugate. As can be seen in Figure 4.4, there is no energy pile-up at high wavenumbers, and the magnitude of the energy density between the smallest and the largest wavenumbers has dropped several orders of magnitude, which indicates that the grid is fine enough to resolve the smallest relevant scales.

Finally, in support of the present analysis, the local average Nusselt number, defined as

$$< Nu > \; = -\frac{H}{\Delta T_{ref}} \; \frac{\partial < T >}{\partial x}\Big|_{x=0} \tag{4.10}$$

for a given position at the hot wall is depicted together with the profile of temperature fluctuations, $< T'T' > /\Delta T^2_{ref}$, in Figure 4.5. In agreement with the two-point correlations, the results are only slightly affected by the domain size as Mesh B1 and Mesh B2 are concerned, thus confirming that the chosen spanwise domain size is adequate. It must be borne in mind that, a reasonable trade-off between accuracy and CPU-time is necessarily adopted, given the cost of the present calculations.

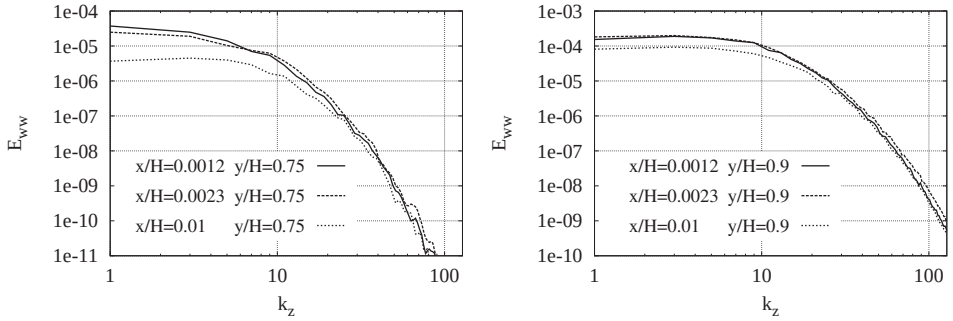

Figure 4.4: Energy spectra of the spanwise velocity component at six monitoring locations for Mesh A.

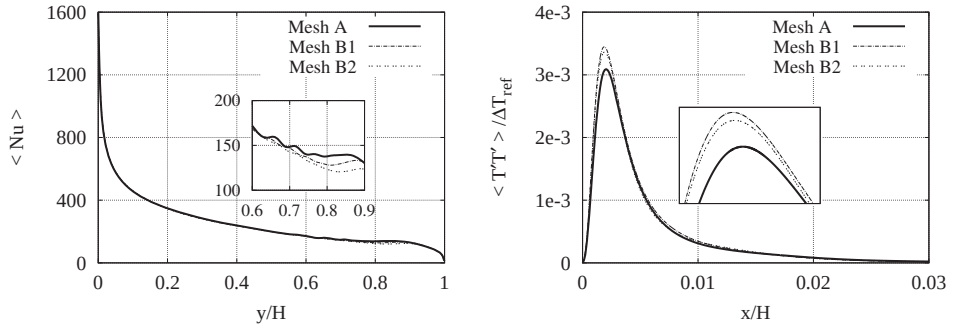

Figure 4.5: Local average Nusselt number (left) and temperature fluctuations, $< T'T' > /\Delta T^2_{ref}$, in the vicinity of the hot wall at $y/H = 0.9$ (right) for the tested meshes.

Thus, considering the present analysis, the numerical results obtained with Mesh A will be hereafter referred to as the DNS solution.

4.4 LES

4.4.1 Governing equations

LES equations are obtained by means of spatially filtering the Equations 4.1-4.3:

$$\nabla \cdot \overline{\mathbf{u}} = 0 \tag{4.11}$$

$$\frac{\partial \overline{\mathbf{u}}}{\partial t} + (\overline{\mathbf{u}} \cdot \nabla)\overline{\mathbf{u}} - \nu \nabla^2 \overline{\mathbf{u}} + \nabla \overline{p} + \overline{\mathcal{F}} = -\nabla \cdot \mathcal{T} \tag{4.12}$$

$$\frac{\partial \overline{T}}{\partial t} + (\overline{\mathbf{u}} \cdot \nabla)\overline{T} - \alpha \nabla^2 \overline{T} = -\nabla \cdot \mathcal{T}_T \tag{4.13}$$

where $\overline{(\cdot)}$ represents a linear spatial filter that commutes with the differential operators. The last terms in Equations (4.12) and (4.13) indicate some modeling of the filtered non-linear convective term. Due to its simplicity and robustness in complex configurations, the present work considers eddy-viscosity models (see [29], for instance). In this case, the traceless part of the SGS stress tensor, $\mathcal{T}$, is defined as,

$$\mathcal{T} - \frac{1}{3}(\mathcal{T} : \boldsymbol{I})\,\boldsymbol{I} = -2\nu_{sgs}\overline{\mathcal{S}} \tag{4.14}$$

where $\overline{\mathcal{S}}$ is the rate-of-strain tensor, $\overline{\mathcal{S}} = \frac{1}{2}[\nabla(\overline{\mathbf{u}}) + \nabla^*(\overline{\mathbf{u}})]$, and ∇^* is the transpose of the gradient operator. $\mathcal{T}_T$ term is evaluated like the $\mathcal{T}$ term, but ν_{sgs} is substituted by ν_{sgs}/Pr_t, where Pr_t is the turbulent Prandtl number (0.4 in this work).

To close the formulation, a suitable expression for the SGS viscosity, ν_{sgs}, must be introduced. In this work, the behavior of different models have been investigated: (i) the WALE model [17], (ii) the QR model [22], (iii) the VMS-WALE model [23]. A brief description of these models is given below.

Wall-adapting local-eddy viscosity (WALE) model

This model is based on the square of the velocity gradient tensor, and it accounts for the effects of both the strain and the rotation rate of the smallest resolved turbulent fluctuations. It was formulated with the following properties: i) vanishing eddy-viscosity ($\nu_{sgs} = 0$) in the regions where the flow is laminar; ii) for any two-dimensional flow $\nu_{sgs} = 0$; iii) at no-slip walls eddy-viscosity also vanishes as $\nu_{sgs} \propto y^3$ and, iv) eddy-viscosity vanishes as the filter size (ℓ) approaches the smallest scales of the flow (i.e. $\nu_{sgs} \to 0$ when $\ell \propto Re^{-3/4}$). The model reads,

$$\begin{aligned} \nu_{sgs} &= (C_w\ell)^2 \frac{(\overline{\mathcal{V}} : \overline{\mathcal{V}})^{\frac{3}{2}}}{(\overline{\mathcal{S}} : \overline{\mathcal{S}})^{\frac{5}{2}} + (\overline{\mathcal{V}} : \overline{\mathcal{V}})^{\frac{5}{4}}} \\ \overline{\mathcal{V}} &= \frac{1}{2}[\nabla(\overline{\mathbf{u}})^2 + \nabla^*(\overline{\mathbf{u}})^2] - \frac{1}{3}(\nabla(\overline{\mathbf{u}})^2 : \boldsymbol{I})\boldsymbol{I} \end{aligned} \tag{4.15}$$

where C_w is the model constant, whose value lies in the range between 0.3 and 0.5. In the present calculations, a value of $C_w = 0.325$ is used. The filter length, ℓ, is evaluated as the cube root of the volume of the cell.

QR eddy-viscosity model

This model has similar properties as the WALE model except for the linear dependance of ν_{sgs}, i.e. $\nu_{sgs} \propto y$, and it is based on the invariants of the rate-of-strain tensor. The model reads,

$$\nu_{sgs} = (C_{qr}\ell)^2 \frac{r^+}{q} \tag{4.16}$$

where $C_{qr} = 1/\pi + 1/24$ is the model constant, $q = (\overline{\mathcal{S}} : \overline{\mathcal{S}})/2$, and $r = -det\,\overline{\mathcal{S}}$ are the second and third invariants of the rate-of-strain tensor, respectively. The r^+ stands for positive values of r invariant, otherwise r is set to zero.

Wall-adapting local-eddy viscosity model within a variational multiscale framework (VMS-WALE)

Originally formulated for the Smagorinsky model in the Fourier space, the variational multiscale approach considers three classes of scales: large, small and unresolved. If a second filter with filter length $\hat{\ell}$ is introduced, a splitting of the scales can be performed,

$$f^{'} = \overline{f} - \hat{f} \tag{4.17}$$

where following Vreman's [30] notation, $f^{'}$ is called the small-scale component, $\hat{f}$ the large-scale component and $\overline{f}$ is the original resolved quantity. Thus, for the large-scale parts of the resolved $\overline{\boldsymbol{u}}$, a general governing equation can be derived,

$$\frac{\partial \overline{\mathbf{u}}}{\partial t} + (\overline{\mathbf{u}} \cdot \nabla)\overline{\mathbf{u}} - \nu\nabla^2\overline{\mathbf{u}} + \nabla\overline{p} + \overline{\mathcal{F}} = -\nabla \cdot \widehat{\mathcal{T}} - \nabla \cdot \mathcal{T}^{'} \tag{4.18}$$

In Equation (4.18) it is possible to identify $\widehat{\mathcal{T}}$ as the subgrid term in the large-scale equation and $\mathcal{T}^{'}$ as the subgrid small-scale term. Neglecting the effect of unresolved

scales in the large-scale equation ($\widehat{\mathcal{T}} \approx 0$), it is only necessary to model the $\mathcal{T}^{'}$. Here the *small-small* strategy is used in conjunction with the WALE model [17],

$$\mathcal{T}^{'} - \frac{1}{3}\left(\mathcal{T}^{'} : \boldsymbol{I}\right)\boldsymbol{I} \quad = \quad -2\nu_{sgs}\mathcal{S}^{'} \tag{4.19}$$

where the formulation is closed by means of ν_{sgs} obtained with the WALE formulation (see Section 4.4.1). In the present study, the globally conservative adjoint filter proposed by Vreman [30] is used as the second filter with $\hat{\ell} = 2\ell$.

4.4.2 Numerical methods for LES

LES are carried out by using the *Termofluids* code [31], which is a parallel object-oriented CFD code. The numerical methods used in both momentum and energy equations for LES are essentially the same as the ones detailed in Section 4.3.2, except for employing second-order conservative schemes on collocated meshes in the discretization of these equations (see for details [32]). As mentioned before, this kind of schemes ensure both stability and conservation of the global kinetic-energy balance on any grid, thus constituting a convenient starting point for LES-like simulations [25]. This numerical methodology has been previously used with accurate results for solving the flow over bluff-bodies with massive separation and turbulent natural convection in enclosures (see for instance [33, 12, 34]).

4.4.3 Numerical parameters for LES

In order to assure that the complex phenomena are reproduced by the LES models, different meshes have been tested. In Table B.1 the parameters of three of the tested LES meshes are given. As is done in the DNS, the meshes are generated uniformly in streamwise and spanwise directions, while the hyperbolic-tangent function of Equation (4.8) is used in the wall-normal direction. Mean flow parameters are obtained by integrating the results during a period of 500 time units in order to assure statistically steady-state solution. The initial transient period of approximately 400 time units is discarded in the light of the information obtained from various probes placed within the domain at locations of different time scales. Results presented in this paper for LES correspond to Mesh C. For further details on the mesh resolution studies see Appendix 5.3.

Mesh	N_x	N_y	N_z	$N_{tot} \times 10^{-6}$	γ_x	$(\Delta x)_{min}/H$
Mesh C	55	491	16	0.43	1.97	6.0×10^{-4}
Mesh D	33	319	8	0.08	2.15	8.0×10^{-4}
Mesh E	55	113	16	0.10	1.97	6.0×10^{-4}

Table 4.2: Main parameters of the numerical simulations for LES. See the caption of Table 4.1 for details.

4.5 Results and discussion

In this section the results obtained with WALE, QR, and VMS-WALE models are compared in detail with the DNS solution to assess their performance in estimating the turbulent flow under consideration. In order to highlight the influence of the models, a solution obtained by the LES code without using any SGS model (No Model) is also presented for Mesh C.

4.5.1 Instantaneous flow

Owing to the buoyancy effects as a consequence of the applied temperature difference at the vertical confining walls, the fluid in contact with the vertical walls moves upwards along the hot wall and downwards along the cold wall. The fluid accelerates along the vertical boundary layers up to a point where the boundary layer is disrupted, thus large unsteady eddies are ejected to the core of the cavity. It is a challenge to capture the location of the transition, which can be affected by the presence of the interacting vertical boundary layers. The extent of the stratified region is directly related with the transition point [12, 19], which shifts upstream as the Ra number increases.

In accordance with the results reported by several authors (see [14, 5, 19], for instance) for similar aspect ratios and Ra numbers, a complex flow with laminar, transitional, and turbulence regions is expected. The existence of different flow regimes can be visualized in Figure 4.6, where time evolution of the dimensionless temperature at different locations is depicted after the initial transient period is washed out (see figure caption for probe locations). Note that the flow in the center of the cavity (P1) is laminar and the temperature value is $\frac{T-T_c}{\Delta T_{ref}} = 0.5$, while at the top of the cavity (P3) more chaotic flow is observed. Due to the differences in the temperature fluctuations, a wide range of time scales are expected too.

In Figure 4.7, a view of the instantaneous isotherms are shown for the DNS. The figure indicates the structure of the flow in the vicinity of the transition region, near both the hot and cold walls. Away from the upper-left and lower-right corners of the cavity, the flow is stratified with quasi-parallel isosurfaces.

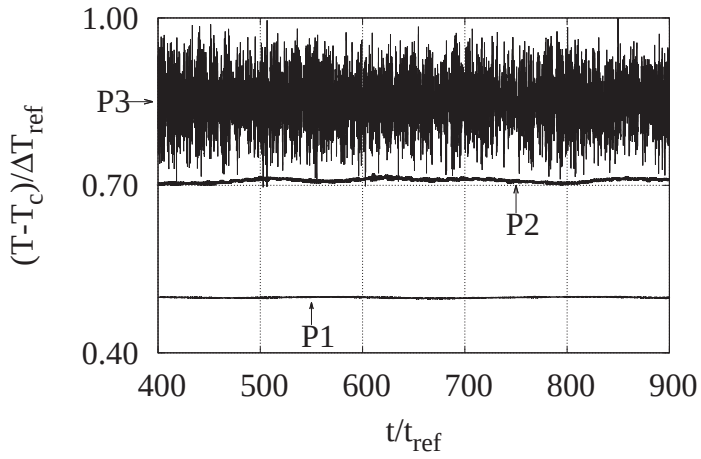

Figure 4.6: Time evolution of temperature at different domain locations for LES using Mesh C. P1≡(0.1,0.5,0.1), P2≡(0.1,0.8,0.1), P3≡(0.0024,0.9,0.1).

4.5.2 Mean flow parameters

The capability of the models to predict the complex physics of the flow is directly related with their performance in properly capturing the transition location. In order to analyze the transition to turbulence, the local average Nusselt number and its standard deviation are plotted in Figure 4.8. Note that the standard deviation of the local average Nusselt number is an indicator of the temperature fluctuations. In the laminar regime, fluctuations and thus standard deviations are insignificant. However, at some stage downstream, the standard deviation starts to rise, which points out the onset of turbulence (see Figure 4.8(b)). In the No Model and QR results, although in a smaller extent for the latter, the instabilities occur much earlier than in the DNS. On the other hand, for the VMS-WALE and WALE, the onset of turbulence location qualitatively coincides with that of the DNS solution.

In Table 4.3, the overall averaged Nusselt numbers, defined as $Nu = (1/H)\int_0^H < Nu > dy$, and the parameters related with the transition to turbulence are presented. Note that it is not straightforward to define a clear cut transition to turbulence location, especially in low-level turbulence flows. For this reason two locations are presented, the former being the location of the onset of turbulence, y_o, defined as the the location where the standard deviation of the Nusselt number exceeds 1 % of

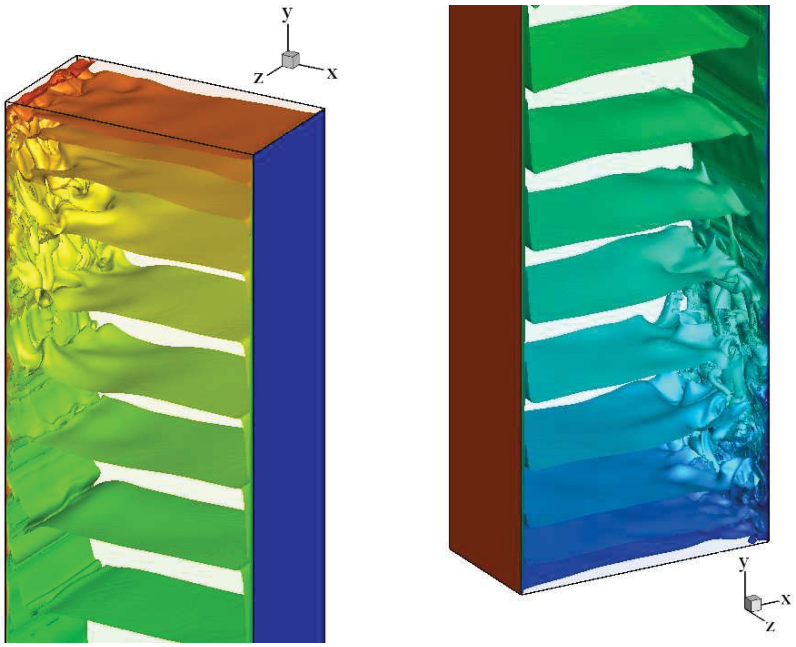

(a) (b)

Figure 4.7: A view of the instantaneous isotherms for the DNS. Transitional and turbulent regions in the vicinity of hot (left) and cold (right) walls. The axes are shown for orientation.

the local average value. The latter is the maximum fluctuation location, y_{max}, where standard deviation of the local average Nusselt number peaks. Regardless of the chosen criterion to define the transition location, the No Model solution indicates upstream transition, $y_o/H = 0.18$. As for the QR model, the onset of turbulence is predicted slightly upstream ($y_o/H = 0.38$) than the reference DNS solution. Note that the VMS-WALE and WALE models predict better the transition, which occurs around mid height of the cavity. Due to the good achievement of the transition location, the overall averaged Nusselt number is well predicted by these two models within an error of approximately 0.4 % .

As can be observed in the detail of the local average Nusselt number (see Figure 4.8(a)), the No Model is unable to predict the heat transfer accurately while the models reproduce the DNS results with relatively small discrepancies. This is espe-

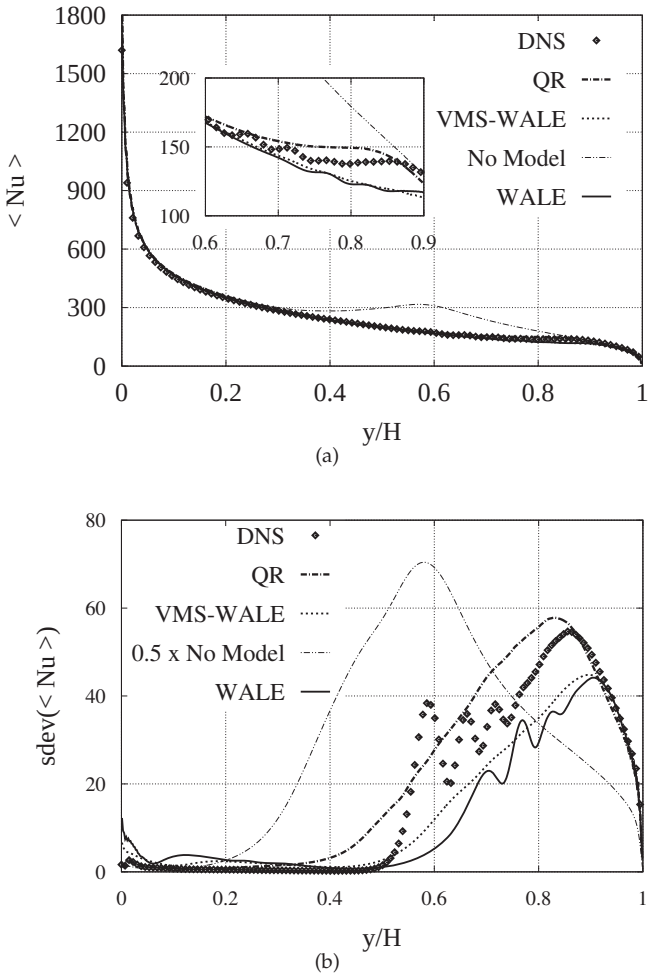

Figure 4.8: Local average Nusselt number and its standard deviation along the hot wall for the tested models.

cially true for the VMS-WALE and WALE models. The WALE model can mimic the complex flow after the onset of turbulence. The standard deviation curve shows that the turbulent fluctuations experience successive reductions and increments, indicating a weak relaminarization trend. The WALE is the only model within the tested

	Nu	e[%]	y_o/H	y_{max}/H	S
DNS	256.4	-	0.51	0.86	0.66
QR	264.0	3.0	0.38	0.83	0.68
VMS-WALE	256.2	0.1	0.49	0.90	0.60
No Model	303.3	18.3	0.18	0.57	0.94
WALE	255.3	0.4	0.54	0.91	0.59

Table 4.3: Overall averaged Nusselt number and transition parameters for the tested models. y_o/H and y_{max}/H are the locations of the onset of turbulence and maximum fluctuation, S is the thermal stratification in the cavity core, respectively.

ones to capture this feature, although this is predicted slightly downstream with respect to the DNS solution. This relaminarization phenomenon seems to be filtered by the VMS-WALE model, although the standard deviation values are quantitatively similar to those of the WALE model.

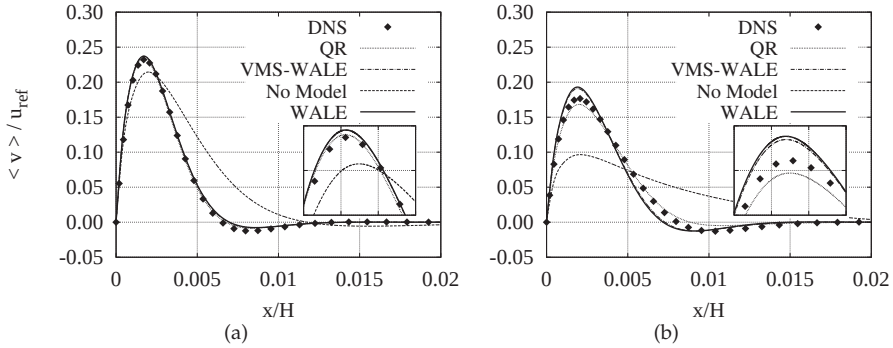

Figure 4.9: Streamwise velocity profile v/u_{ref} in the vicinity of the hot wall at different locations. (a) $y/H = 0.5$ (b) $y/H = 0.75$.

In Figure 4.9, the streamwise velocity profiles at mid height ($y/H = 0.5$) and at $y/H = 0.75$ are plotted in the vicinity of the hot wall. Note that the velocity is well predicted by all the models at the mid height. However, as the flow gets downstream, the models are unable to capture the streamwise velocity component with the same precision. The VMS-WALE and WALE overestimate, while the QR underestimates, the maximum streamwise velocity -all within 10 %- performing the QR slightly better than the other models. If no model is used, the discrepancies with the reference solution are of the order of 8 % even at the mid height, where a pronounced thickening of the boundary layer is observed. In the absence of model, for the tested

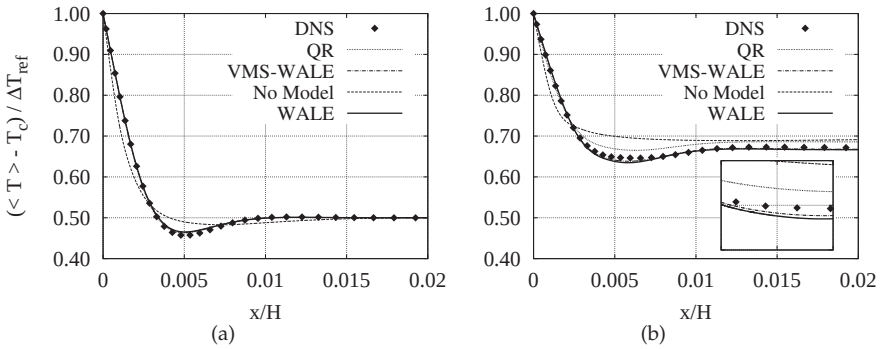

Figure 4.10: Temperature profile in the vicinity of the hot wall at different locations. (a) $y/H = 0.5$ (b) $y/H = 0.75$.

mesh, it seems that the excess of turbulent kinetic energy cannot be dissipated by the molecular viscosity, thus leading to an earlier transition. This implies the deceleration of the fluid due to enhanced wall-normal motion, which justifies the thicker boundary layer. This trend continues at the downstream location, where the physics of the flow can no longer be reproduced as the error is as high as 45 %.

The temperature profiles at the same locations are depicted in Figure 4.10, confirming the high degree of agreement of all the models at mid height. At the downstream location where the flow is more chaotic, the VMS-WALE and WALE models achieve good performance on temperature prediction, whereas the QR model yields a warmer cavity. The warmer cavity prediction of the QR model can be attributed to the upstream transition prediction. In the absence of model, however, the results deviate even qualitatively from the reference solution, which is due to the poor performance in capturing the transition location. It is important to note that both the VMS-WALE and WALE models, in turn, predict qualitatively similar flow structures to those of the reference solution, thanks to their refined prediction of the transition location.

The performance of the tested models in the whole cavity can also be assessed by means of the temperature profiles at mid width, $x/W = 0.5$, as shown in Figure 4.11. The conclusions drawn by analyzing the models at particular horizontal profiles (i.e. $y/H = 0.5, 0.75$) are seen to be applicable to the entire cavity. The VMS-WALE and WALE models predict the temperature satisfactorily throughout the cavity height, especially between $y/H = 0.6$ and $y/H = 0.9$ (and the equivalent locations at the bottom of the cavity) where turbulent fluctuations are expected to be influential. The No Model and the QR model, however, overestimate (underestimate) the tem-

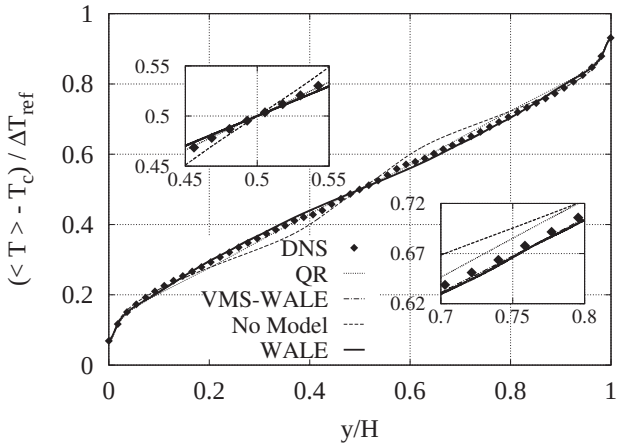

Figure 4.11: Temperature profiles at mid width along the cavity height.

perature at the top (bottom) of the cavity. Note that the discrepancies with the DNS solution are more pronounced when no model is used. As for the thermal stratification in the core of the cavity, the No Model highly overestimates the reference value while the model predictions are within approximately 10 %.

In Figure 4.12, the dimensionless time-averaged wall shear stresses obtained are compared with the DNS results. The results indicate that all the tested models can follow the trend of gradual shear stress reduction as observed in the DNS solution. As for the No Model, the marked decrease in the wall shear stress points out the thickening of the boundary layer. Note that the QR model can reproduce the reference wall shear stress values in the top of the cavity, which can also be anticipated from the higher degree of agreement in the streamwise velocity component for this model.

4.5.3 Turbulent statistics

The performance of the models in predicting the turbulent statistics is tested at the same locations, i.e. $y/H = 0.5$ and $y/H = 0.75$. Although the No Model has already failed in predicting the mean flow parameters accurately, the corresponding turbulent statistics are also presented for comparison purposes. In Figure 4.13, the normal and shear Reynolds stresses are depicted. Note that at $y/H = 0.5$, the Reynolds stresses for both the No Model and the QR model are significantly greater than the

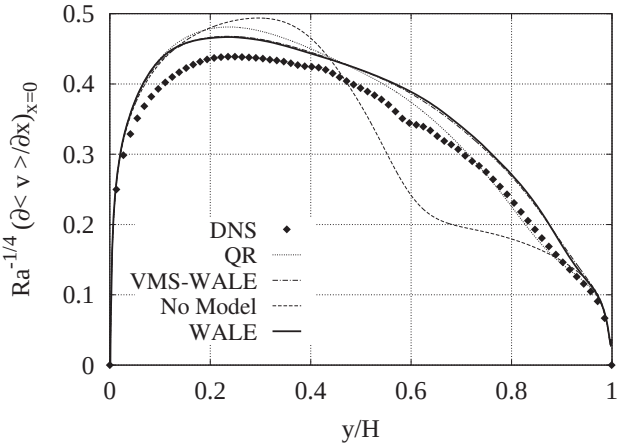

Figure 4.12: Dimensionless time-averaged wall shear stress at the hot wall scaled by $Ra^{1/4}$.

DNS results, which is in accordance with the upstream transition prediction as explained earlier in this section. Moreover, the maxima occur at different locations, indicating different physics of the flow. Note that the Reynolds stresses are overpredicted by the No Model up to three orders of magnitude, showing that the stresses cannot be reproduced even qualitatively without a model. As for the VMS-WALE and WALE models, although the Reynolds stress values are underestimated, the locations of maximum and minimum values are well predicted, with the exception of the local $< v'v' >$ and $< u'v' >$ peaks in the boundary layer, as these maxima are predicted slightly closer to the wall. Note that at this location the values are relatively small, indicating quasi-laminar flow. At $y/H = 0.75$, all the predictions are of the same order of magnitude, yet the VMS-WALE and WALE perform somehow better than the QR, especially in predicting the dominant $< v'v' >$ term.

In Figure 4.14, the turbulent heat fluxes and the temperature fluctuations are depicted at the same locations. The results confirm the good performance of the VMS-WALE and WALE models, while a similar mismatch in results are observed for the No Model and the QR. Note that the dominant streamwise turbulent heat flux term (see Figure 4.14(d)) is well predicted by the VMS-WALE and WALE models, not only in magnitude but also in the locations where the maxima occur, which may indicate a satisfactory overall performance of the mentioned models in predicting the flow under consideration.

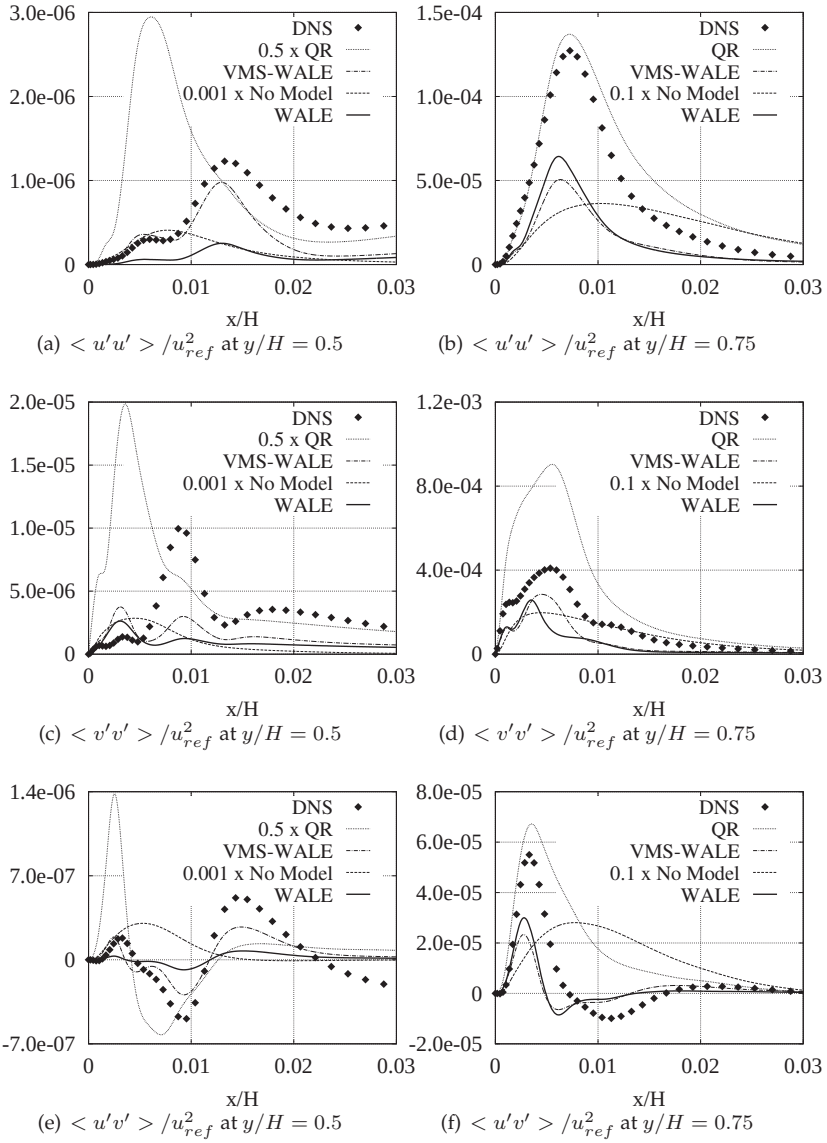

Figure 4.13: Reynolds stresses in the vicinity of the hot wall at different locations. (left) $y/H = 0.5$ (right) $y/H = 0.75$.

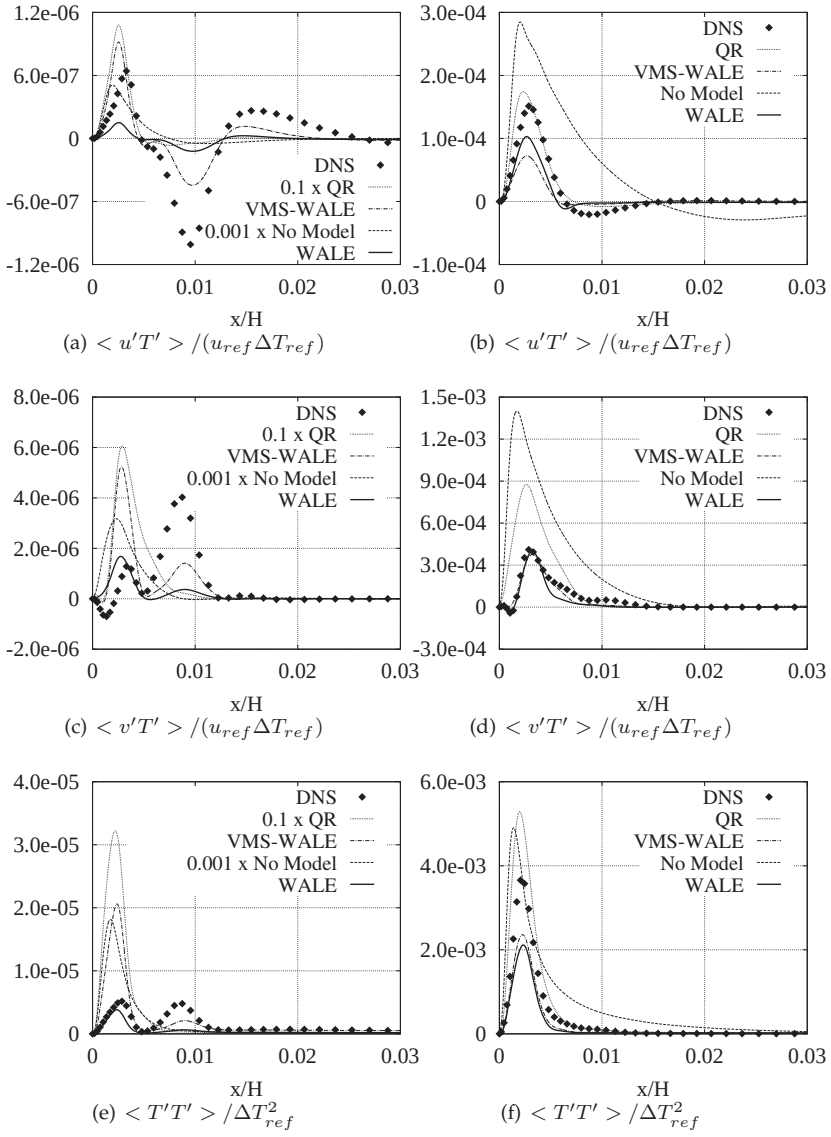

Figure 4.14: Turbulent heat fluxes and temperature fluctuations in the vicinity of the hot wall at different locations. (left) $y/H = 0.5$ (right) $y/H = 0.75$.

4.6 Conclusions

The performance of three subgrid-scale models for predicting the turbulent natural convection flow in a water-filled differentially heated cavity of aspect ratio 5 at $Ra = 3 \times 10^{11}$ and $Pr = 4.31$ has been studied. The models considered are the wall-adapting local-eddy viscosity model (WALE), the QR model, and the WALE model within a variational multiscale framework (VMS-WALE). A direct numerical simulation (DNS) has also been carried out in order to obtain a reference solution. Mean flow parameters and turbulent statistics have been presented for the tested models for their comparison with the DNS solution. It is shown that the performance of the models is directly linked to the accurate prediction of the transition to turbulence in agreement with the observations by other authors.

The results reveal that, for the flow under consideration, although all the models perform well, the VMS-WALE and WALE models perform better due to their capability to capture the transition to turbulence phenomenon, predicting accurately the heat transfer and flow structure. A similar behavior is observed for the turbulent statistics, where the VMS-WALE and WALE generally perform well, reproducing the general trend of the DNS results. It has been also shown that if no SGS model is used, the flow behavior cannot be reproduced even qualitatively due to inaccurate prediction of the transition location.

Finally, it is the aim of the authors to make publicly available the current DNS results by creating an extended database [35] which might be useful for validating future RANS and LES studies.

References

[1] G. De Vahl Davis, Natural convection of air in a square cavity: a benchmark numerical solution, International Journal for Numerical Methods in Fluids 3 (1983) 249–264.

[2] R. Henkes, F. van Der Vlugt, C. Hoogendoorn, Natural convection flow in a square cavity calculated with low Reynolds-number turbulence models, International Journal of Heat and Mass Transfer 34 (1991) 377–388.

[3] T. Fusegi, J. M. Hyun, K. Kuwahara, B. Farouk, A numerical study of three-dimensional natural convection in a differentially heated cubical enclosure, International Journal of Heat and Fluid Flow 34 (6) (1991) 1543–1557.

[4] R. Janssen, R. Henkes, Accuracy of finite-volume discretizations for the bifurcating natural-convection flow in a square cavity, Numerical Heat Transfer, Part B 24 (1993) 191–207.

[5] P. Le Quéré, M. Behnia, From onset of unsteadiness to chaos in a differentially heated square cavity, Journal of Fluid Mechanics 359 (1998) 81–107.

[6] S. Xin, P. Le Quéré, Direct numerical simulations of two-dimensional chaotic natural convection in a differentially heated cavity of aspect ratio 4, Journal of Fluid Mechanics 304 (1995) 87–118.

[7] F. X. Trias, M. Soria, A. Oliva, C. D. Pérez-Segarra, Direct numerical simulations of two and three dimensional turbulent natural convection flows in a differentially heated cavity of aspect ratio 4, Journal of Fluid Mechanics 586 (2007) 259–293.

[8] F. X. Trias, A. Gorobets, M. Soria, A. Oliva, Direct numerical simulation of a differentially heated cavity of aspect ratio 4 with Rayleigh numbers up to 10^{11} - Part II: Heat transfer and flow dynamics, International Journal of Heat and Mass Transfer 53 (2010) 674–683.

[9] J. Patterson, J. Imberger, Unsteady natural convection in a rectangular cavity, Journal of Fluid Mechanics 100 (1980) 65–86.

[10] P. Le Quéré, Transition to unsteady natural convection in a tall water-filled cavity, Physics of Fluids A 2 (1990) 503–515.

[11] P. J. A. Janssen, R. A. W. M. Henkes, Influence of Prandtl number on instability mechanisms and transition in a differentially heated square cavity, Journal of Fluid Mechanics 290 (1995) 319–344.

[12] D. Kizildag, I. Rodríguez, A. Oliva, O. Lehmkuhl, Limits of the Oberbeck-Boussinesq approximation in a tall differentially heated cavity filled with water, International Journal of Heat and Mass Transfer 68 (2014) 489–499.

[13] S. Peng, L. Davidson, Large eddy simulation for turbulent buoyant flow in a confined cavity, International Journal of Heat and Fluid Flow 22 (2001) 323–331.

[14] D. Barhaghi, L. Davidson, Natural convection boundary layer in a 5:1 cavity, Physics of Fluids 19 (2007) 125106.

[15] J. Smagorinsky, General circulation experiments with the primitive equations: I. The basic experiment, Monthly Weather Review 91 (1963) 99–164.

[16] M. Germano, U. Piomelli, P. Moin, W. Cabot, A dynamic subgrid-scale eddy viscosity model, Physics of Fluids A 3 (1991) 1760.

[17] F. Nicoud, F. Ducros, Subgrid-scale stress modeling based on the square of the velocity gradient tensor, Flow, Turbulence and Combustion 62 (1999) 183–200.

[18] G. E. Lau, G. H. Yeoh, V. Timchenko, J. A. Reizes, Large-eddy simulation of turbulent buoyancy-driven flow in a rectangular cavity, International Journal of Heat and Fluid Flow 39 (2013) 28–41.

[19] F. X. Trias, A. Gorobets, C. D. Pérez-Segarra, A. Oliva, DNS and regularization modeling of a turbulent differentially heated cavity of aspect ratio 5, International Journal of Heat and Mass Transfer 57 (2013) 171–182.

[20] N. S. Ghaisas, D. A. Shetty, S. H. Frankel, Large eddy simulation of thermal driven cavity: Evaluation of subgrid-scale models and flow physics, International Journal of Heat and Mass Transfer 55 (2013) 606–624.

[21] A. Sergent, P. Joubert, S. Xin, P. Le Quéré, Resolving the stratification discrepancy of turbulent natural convection in differentially heated air-filled cavities Part II: End walls effects using large eddy simulation, International Journal of Heat and Fluid Flow 39 (2013) 15–27.

[22] R. Verstappen, When does the viscosity damp subfilter scales sufficiently?, Journal of Scientific Computing 49 (1) (2011) 94–110.

[23] T .J .R. Hughes, L. Mazzei, K. E. Hanzen, Large eddy simulation and the variational multiscale method, Computing and Visualization in Science 3 (1) (2000) 47–59.

[24] R. Cheesewright, K. J. King, S. Ziai, Experimental data for the validation of computer codes for the prediction of two-dimensional buoyant cavity flows, in: Proceedings of Significant Questions in Buoyancy Affected Enclosure or Cavity Flows, ASME, Heat Transfer Division, HTD, vol 60 (1986) 75–81.

[25] R. W. C. P. Verstappen, A. E. P. Veldman, Symmetry-preserving discretization of turbulent flow, Journal of Engineering Mathematics 187 (1) (2003) 343–368.

[26] F. X. Trias, O. Lehmkuhl, A self-adaptive strategy for the time integration of Navier-Stokes equations, Numerical Heat Transfer, Part B 60 (2) (2011) 116–134.

[27] P. J. Roache, Code verification by the method of the manufactured solutions, Journal of Fluids Engineering 124(1) (2001) 4–10. doi:10.1115/1.1436090.

[28] J. Fröhlich, C. P. Mellen, W. Rodi, L. Temmerman, M. A. Leschziner, Highly resolved large-eddy simulation of separated flow in a channel with streamwise periodic constrictions, Journal of Fluid Mechanics, 526, 19–66 (2005), doi: 10.1017/S0022112004002812.

[29] P. Sagaut, Large eddy simulation for incompressible flows, Springer-Verlag, 2006.

[30] A. Vreman, The adjoint filter operator in large-eddy simulation of turbulent flow, Physics of Fluids 16 (6) (2004) 2012, doi: 10.1063/1.1710479.

[31] O. Lehmkuhl, C. D. Pérez-Segarra, R. Borrell, M. Soria, A. Oliva, TERMOFLUIDS: A new Parallel unstructured CFD code for the simulation of turbulent industrial problems on low cost PC cluster, in: Proceedings of the Parallel CFD 2007 Conference, 2007, pp. 1–8.

[32] L. Jofre, O. Lehmkuhl, J. Ventosa, F. X. Trias, A. Oliva, Conservation properties of unstructured finite-volume mesh schemes for the Navier-Stokes equations, Numerical Heat Transfer, Part B 65 (1) (2014) 53–79, doi:10.1080/10407790.2013.836335.

[33] I. Rodríguez, R. Borrell, O. Lehmkuhl, C. D. Pérez-Segarra, A. Oliva, Direct numerical simulation of the flow over a sphere at $Re = 3700$, Journal of Fluid Mechanics 679 (2011) 263–287.

[34] O. Lehmkuhl, I. Rodríguez, A. Baez, A. Oliva, C. D. Pérez-Segarra, On the large-eddy simulations for the flow around aerodynamic profiles using unstructured grids, Computers and Fluids 84 (2013) 176–189.

[35] The DNS data presented in this article are available by contacting the authors.

Chapter 5

Concluding remarks and further work

5.1 Concluding remarks

This thesis has aimed at contributing to the knowledge in the field of fluid dynamics and heat transfer in natural convection cases. This is a field where important contributions have been made and where the CTTC has an extensive knowledge. This work has intended to be a step forward into this research, broadening the study to cases where the effects of variable thermophysical properties on the heat transfer are important.

In this sense, the Chapter 2 has shown that even for relatively small temperature gradients between the vertical walls, these effects become relevant affecting not only the heat transfer, but also changing the flow topology. Even for temperature differences of 30^oC, the validity of the Oberbeck-Boussinesq hypothesis has to be questioned as the flow rapidly looses its symmetry and the evolution of hot and cold boundary layers significantly changes. All in all, it has been shown that neglecting the NOB effects may certainly lead to erroneous estimations of the phenomena taking place inside the cavity.

Although important effects were discussed in Chapter 2 regarding the influence of variable thermophysical properties as the thermal gradients increase, other effects related to the three-dimensional nature of the flow have not been studied. Thus, in Chapter 3, relevant characteristics of the flow topology have been investigated. The results have revealed that Non-Oberbeck-Boussinesq (NOB) effects seem to influence not only the heat transfer but also the way both hot and cold boundary layers transition to turbulence. Contrary to the Oberbeck-Boussinesq (OB) case where transition to turbulence occurs symmetrically about the midheight of the cavity, in the NOB problem this point moves forward towards the top of the cavity in the hot boundary layer, oscillating around a certain location. This oscillation of the transition point is

not observed in the OB case nor in the 2D NOB simulation. This is one of the effects of the three-dimensionality of the flow near the transition point, where Tollmien-Schlichting waves cluster and break into smaller structures that are regularly shed towards the core of the cavity in the hot boundary layer. This effect is not observed in the cold wall which behaves in a different manner. The periodic formation of a large vortex and its shedding into the fluid found in the core, degrades the stratification in the core of the cavity. This is another difference with respect to the 2D NOB flow, where despite the shift in transition, a highly stratified core was still observed. Moreover, important characteristics of the behavior of the boundary layers and their thickness measurements have been reported in this chapter.

One important challenge in the numerical simulation of fluid dynamics and heat transfer phenomena is to find numerical models that accurately describe the phenomena taking place without a huge computational cost. This is especially true in natural convection cases with water as working fluid, since the boundary layer becomes thinner with the increase of the Rayleigh number, and DNS turns out to be an expensive tool (from a computational point of view). In this sense, in Chapter 4 the appropriateness of different subgrid-scale closures for accurately describing the flow topology has been tested. The models used were known to behave quite well in other similar situations (especially transition to turbulence in forced convection). It has been shown that an important feature expected from the model is its ability to accurately capture the transition to turbulence in the attached boundary layer. Those models which exhibited this feature predict fairly well both first and second order statistics. This has been the case for the VMS-WALE and for the WALE models, the latter being also capable of capturing the transition, relaminarization and further transition to turbulence of the flow with quite good accuracy.

Last but not the least, it is convenient to point out that throughout the development of this thesis several direct numerical simulations considering both OB and NOB effects have been performed. The data resulting from these simulations constitute a valuable tool for the CFD community for assessing and developing new turbulence models. This data will become available from the CTTC site in the near future.

5.2 Ongoing work

In the context of the present thesis work, after having completed two- and three-dimensional DNS studies to have insight into the NOB effects, and having assessed the performance of different SGS models under OB flow regime for the DHC flow of water, the final step to conclude these investigations is the employment of the SGS models for capturing the flow dynamics and heat transfer when the NOB effects are taken into account, which -to the best knowledge of the PhD candidate- has not been

Table 5.1: Main parameters for LES and DNS calculations for aspect ratio 5. N_x, N_y, and N_z are the number of control volumes (CV) in (x), (y), and (z) directions, respectively. N_{total} is the number of total CVs. Δx_{min} is the smallest wall-normal distance.

Mesh	N_x	N_y	N_z	N_{total}	Δx_{min}
LES I	33	319	8	8.4×10^4	8.0×10^{-4}
LES II	55	491	16	4.3×10^5	6.0×10^{-4}
DNS III	192	518	64	6.4×10^6	1.8×10^{-4}

performed before for the flow under consideration. To that end, the case studied in Chapter 4 under OB regime, i.e. the water filled DHC of aspect ratio $H/W = 5$, $Ra = 3 \times 10^{11}$ based on cavity height, $T_h = 60\ ^\circ C$, $T_c = 20\ ^\circ C$, reference temperature $T_r = 40\ ^\circ C$, $Pr_r = 4.31$, has been submitted to investigation by means of direct numerical simulation, this time considering the NOB effects. The governing equations and the numerical method for NOB are given in detail in Chapter 3. First, the reference NOB DNS solution has been obtained. Owing to the know-how acquired in the assessment of the SGS models for OB (see Chapter 4), the methodology is then directly extended to the NOB. In this preliminary work, the WALE [5] model has been chosen as this model has provided promising results for OB. In Table 5.1, the numerical parameters employed in the present DNS and LES studies are presented.

The preliminary results obtained with WALE model are presented in Table 5.2, where the transition to turbulence locations and the global Nusselt number are given. Note that *LES II* predicts reasonably well (within 3 %) the Nusselt number, and the features like the loss of symmetry, delayed and premature transition in the hot and cold wall boundary layers, respectively, are captured relatively well by means of an approximately 15 times coarser mesh. In Figure 5.2, dimensionless temperature profile at upper cavity, $y/H = 0.95$, is plotted, where WALE solution on *LES II* mesh can provide acceptable results.

However, in the course of the present investigation, it has been observed that the chosen case might not be adequate for the purpose of the study since, for these flow parameters, the NOB effects have finally shown to have limited effect on the flow structure and heat transfer (see Figure 5.1 for representative instantaneous isotherms). In order to distinguish properly between the differences which can be attributed to the performance of the SGS models from those occurring due to the NOB effects, the case studied in Chapter 3 has been proposed as a new case to assess the performance of the SGS models considering NOB effects. Note that for this case, -with aspect ratio $H/W = 10$, $Ra = 3 \times 10^{11}$, $T_h = 90\ ^\circ C$, $T_c = 10\ ^\circ C$, and $Pr_r = 3.41$- the comparison

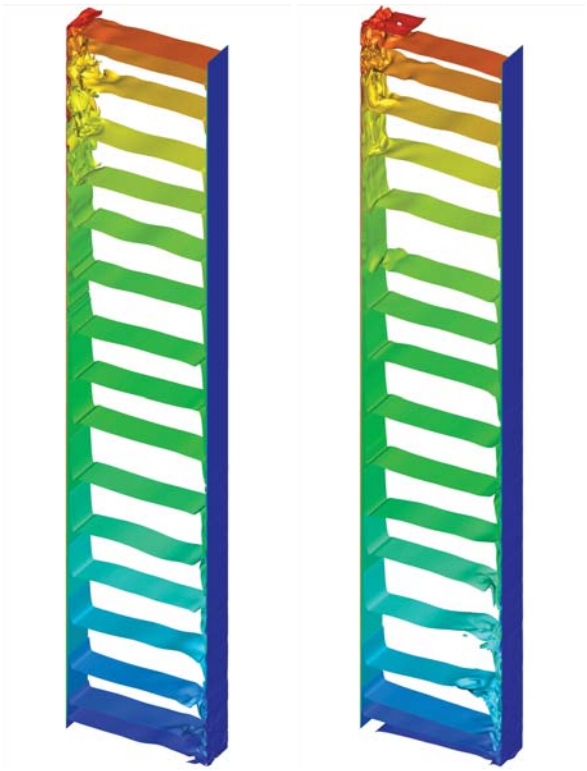

Figure 5.1: Instantaneous isotherms corresponding to OB (a) and NOB (b) by means of DNS for aspect ratio 5.

Table 5.2: Summary of the results obtained for NOB: Time averaged Nu and transition point in hot and cold vertical boundary layers, x_{tr-HOT} and $x_{tr-COLD}$, respectively (aspect ratio 5).

Case	Nu	x_{tr-HOT}	$x_{tr-COLD}$
NOB WALE (LES I)	336 (31.2 %)	0.08	0.57
NOB WALE (LES II)	262 (2.3 %)	0.76	0.68
NOB DNS (DNS III)	256	0.66	0.50

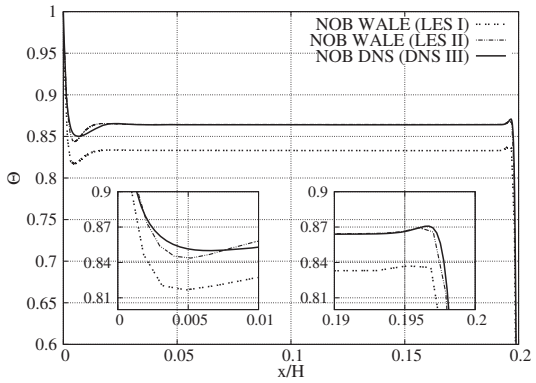

Figure 5.2: Dimensionless temperature profile Θ=(T-T_c)/($T_h - T_c$) considering NOB effects at $y/H = 0.95$ for aspect ratio 5.

Table 5.3: Main parameters for LES and DNS calculations and summary of the preliminary results considering NOB effects for aspect ratio 10 (See captions of Tables 5.1 and 5.2 for the definitions of the parameters.

Mesh	N_x	N_y	N_z	N_{total}	Δx_{min}	Nu	x_{tr-HOT}	$x_{tr-COLD}$
LES	55	511	16	4.5×10^5	4.8×10^{-4}	263.8 (3.6 %)	0.72	0.50
DNS	194	782	196	29.7×10^6	1.0×10^{-4}	273.8	0.68	0.46

of DNS results have already revealed important NOB effects.

At the time of the preparation of this manuscript, some preliminary results have been obtained with WALE model on the mesh shown in Table 5.3 which is given together with the DNS results for reference. Note that the vertical temperature profile depicted in Figure 5.3 indicates a generally reasonable agreement with respect to the DNS results, except for the portion affected by the transition region. The Nusselt number and the features related with the transition location are predicted relatively well (see Table 5.3), while it must be borne in mind that the results are still preliminary and a higher resolution mesh could improve discrepancies observed in the temperature profiles.

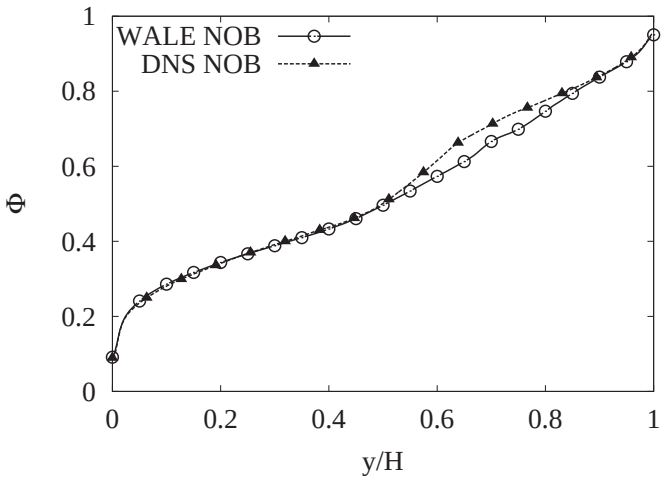

Figure 5.3: Dimensionless temperature profile Θ=(T-T_c)/($T_h - T_c$) considering NOB effects at $x/H = 0.05$ for aspect ratio 10.

5.3 Further work

Future action following the research performed within the framework of this thesis will mainly focus on two lines.

On the one hand, more research on subgrid-scale models, which are more appropriate for describing the phenomena taking place in natural convection problems, is needed. According to Obukhov-Bolgiano dynamics [1], first suggested for stratified turbulence in the range of scales between the large scales and the so-called Bolgiano's length, the turbulent kinetic energy decay would follow a slope of $-11/5$, whereas the thermal spectrum would follow a slope of $-7/5$. The energy decay would recover Kolmogorov scaling for smaller scales down to dissipative ones. It has to be pointed out that non of these scenarios have been captured neither by experimental nor by numerical techniques [2]. Conversely, what has been observed in some cases is a temperature spectrum decay according with a $-7/5$, and a velocity spectrum decay with a $-5/3$ slope following Kolmogorov theory [3, 4]. We do not foresee at this stage following an investigation focused on finding the proof of the Bolgiano's scaling. However, we can anticipate that our next focus could be trying to find new subgrid-scale closures that can mimic the observed behavior in the spectra decay, especially for the temperature. That is, considering that most SGS models are for-

mulated for reproducing a Kolmogorov energy cascade, and that energy decay in these kind of flows varies depending on the location within the cavity, an appropriate SGS model has to be capable of adapting its behavior to the different situations.

On the other hand, the present research has highlighted the importance of considering variable thermophysical properties when it comes to describing the flow structure and thermal behavior of the fluid inside a tall water-filled cavity subjected to large temperature gradients. For those cases, in which the simplified models used in long-term simulation of thermal systems are doomed to fail, new models and/or correlations for the heat transfer have to be introduced. In this sense, the future research will focus on fine tuning of these models and actually adapting the already known correlations for cases were the thermophysical properties play a major role in the heat transfer.

References

[1] R. Bolgiano. Turbulent spectra in a stably stratified atmosphere. *Journal of Geophysics Research*, 64:2226–2229, 1959.

[2] Detlef Lohse and Ke-Qing Xia. Small-Scale Properties of Turbulent Rayleigh-Bénard Convection. *Annual Review of Fluid Mechanics*, 42(1):335–364, 2010.

[3] Verzicco R. and R. Camussi. Numerical experiments on strongly turbulent thermal convection in a slender cylindrical cell. *Journal of Fluid Mechanics*, 477:19–49, 2003.

[4] I. Rodríguez, O. Lehmkuhl, R. Borrell, and C. D. Perez-Segarra. On DNS and LES of natural convection of wall-confined flows: Rayleigh-Bénard convection. In Hans Kuerten, Bernard Geurts, Vincenzo Armenio, and Jochen Fröhlich, editors, *Direct and Large-Eddy Simulation VIII (ERCOFTAC Series)*, pages 389–394. Springer, 2011.

[5] Nicoud, F., Ducros, F.: Subgrid-scale stress modeling based on the square of the velocity gradient tensor. Flow, Turbulence and Combustion, **62**:183–200, (1999)

Appendix A

Developement of a multi-functional ventilated facade with an integrated collector-storage: numerical model and experimental facility. Presented at ISES World Congress, Kassel, Germany. 2011

DEVELOPMENT OF A MULTI-FUNCTIONAL VENTILATED FAÇADE WITH AN INTEGRATED COLLECTOR-STORAGE: NUMERICAL MODEL AND EXPERIMENTAL FACILITY

Deniz Kizildag, Ivette Rodriguez and Assensi Oliva

Centre Tecnològic de Transferencia de Calor (CTTC)

Universitat Politècnica de Catalunya (UPC)

ETSEIAT, Colom 11, 08222 Terrassa (Barcelona), Spain

Fax: +34 93 739 89 20 e-mail: cttc@cttc.upc.edu

Abstract

The paper reports on physical modeling and experimental evaluation of glazed systems. A multi-functional ventilated façade with an integrated collector-storage is developed and mounted on a test cell facility under real weather conditions. The component uses solar radiation to produce solar heated water flow, which in turn can provide space heating or fulfill domestic hot water demands. Different operational modes of the ventilation channel are analyzed in order to improve the thermal performance of the buildings with glazed façades.

The existing numerical platform for the prediction of the thermal performance of buildings and solar systems is used to implement a numerical model to address the multi-functional ventilated façade with integrated collector-storage element. The model uses the measured outdoor data as boundary conditions to obtain predictions by means of a general energy balance in the test room and the façade component. The model permits different levels of simulation depending on the desired precision in each element, applying a modular methodology. In this study, the convection heat transfer coefficient within the parallelepiped storage tank is obtained from a direct numerical simulation (DNS) of turbulent natural convection flow of water, while the remaining empirical information is obtained from the literature for similar geometries.

1. Introduction

The existing buildings account for over 40 % of the total energy consumption in Europe. Growth in population, increasing demand for building services and comfort levels, together with the rise in time spent inside the buildings, indicate that the upward trend in energy consumption within buildings will continue to grow (Pérez-Lombard et al., 2008). This fact not only stimulates the efforts in the development of innovative and efficient products of reduced environmental impact, but also makes necessary tools and methodologies for analyzing the performance of these products and the buildings into which they are integrated (Bloem et al., 2010).

The envelopes play an important role in the thermal behavior of the buildings. In addition to fulfilling the architectural requirements, the energy efficient design of the building envelopes can contribute greatly in reducing the heating and cooling loads of the dwellings (Faggembauu, 2006). Multi-functional ventilated façades appear as an interesting solution taking into consideration aspects like improved thermal behavior, acoustic insulation and daylight illumination, attractive outdoor aspect, possibility to incorporate innovative elements.

The present work is on physical modeling and experimental evaluation of glazed systems. An integrated collector-storage element composed of a single glass pane, a layer of transparent insulation material (TIM), a parallelepiped storage tank with selective absorber surface, and opaque insulation is developed. This element, as a whole, works as an opaque element that produces solar heated water. Two cases have been considered in this work:

- CASE A: The integrated collector-storage element is mounted on a south facing aperture of the controlled test room as a single skin opaque element.

- CASE B: A double skin façade component is mounted where an external single-pane glass skin is separated from the inner skin by a ventilation channel. Natural and forced convection operational modes are possible. The inner skin consists of two zones: i) the upper double-pane glass skin, ii) the lower integrated collector-storage element.

The test facility is equipped with a data acquisition system monitoring outdoor and indoor climate conditions, namely the total and diffuse radiation incident on the façade, wind direction and velocity, air temperatures, relative humidity, and the temperatures at various test cell facility surfaces.

The numerical model to address the multi-functional ventilated façade with integrated collector-storage element (Faggembauu et al., 2003) is adapted to the existing numerical platform for the prediction of the thermal performance of buildings and solar systems (Damle et al., 2011). This object-oriented modular platform is intended to permit coupling between low level resolution models and CFD models based on large eddy simulation (LES) models or DNS, so that some critical zones within the façades or buildings can be modeled with more detail than others.

The collected experimental data is processed and analyzed to validate the numerical model, and to obtain a better understanding of the thermal behavior of the component.

Expected results are given for some operational modes, by comparing the numerically calculated and the measured test cell facility temperatures at different zones.

2. Experimental Facility

The scheme of the multi-functional ventilated façade is shown in Figure 1. The outer skin of the façade is composed of a single-pane glass layer. The inner skin is separated from the outer skin by means of an air channel. The air flow in the air channel can be due to natural or forced convection. The inner skin is composed of two zones. The upper zone is of double-pane glass, while in the lower zone the integrated collector-storage element is installed.

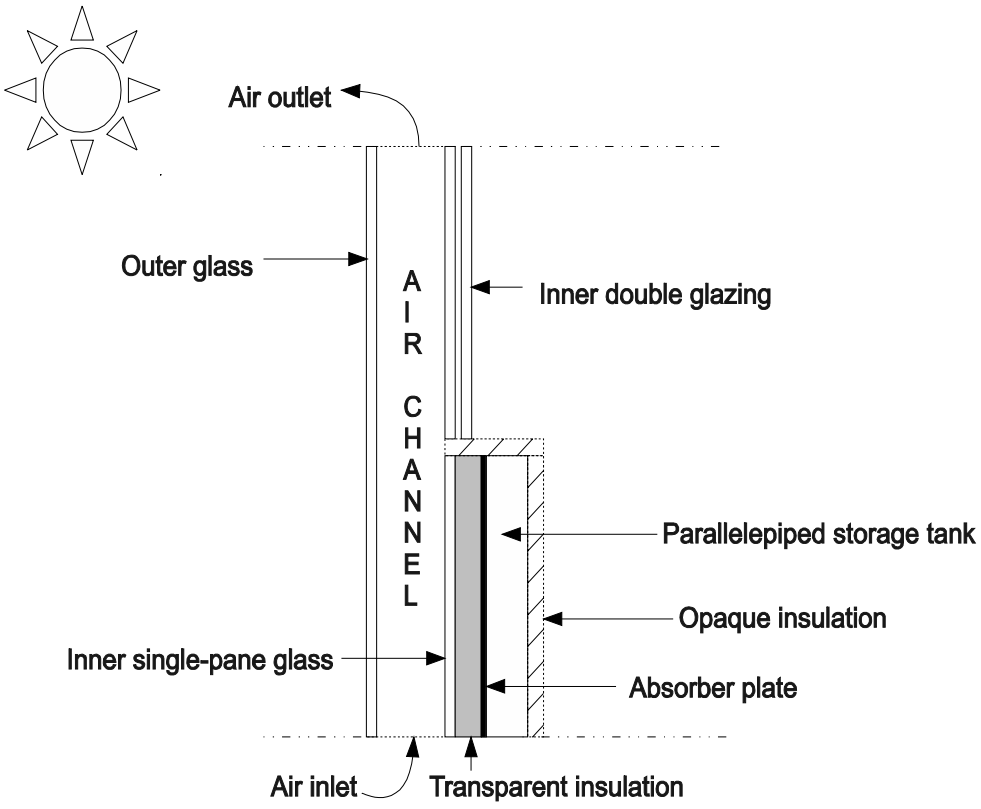

Fig. 1: Scheme of the multi-functional façade (CASE B)

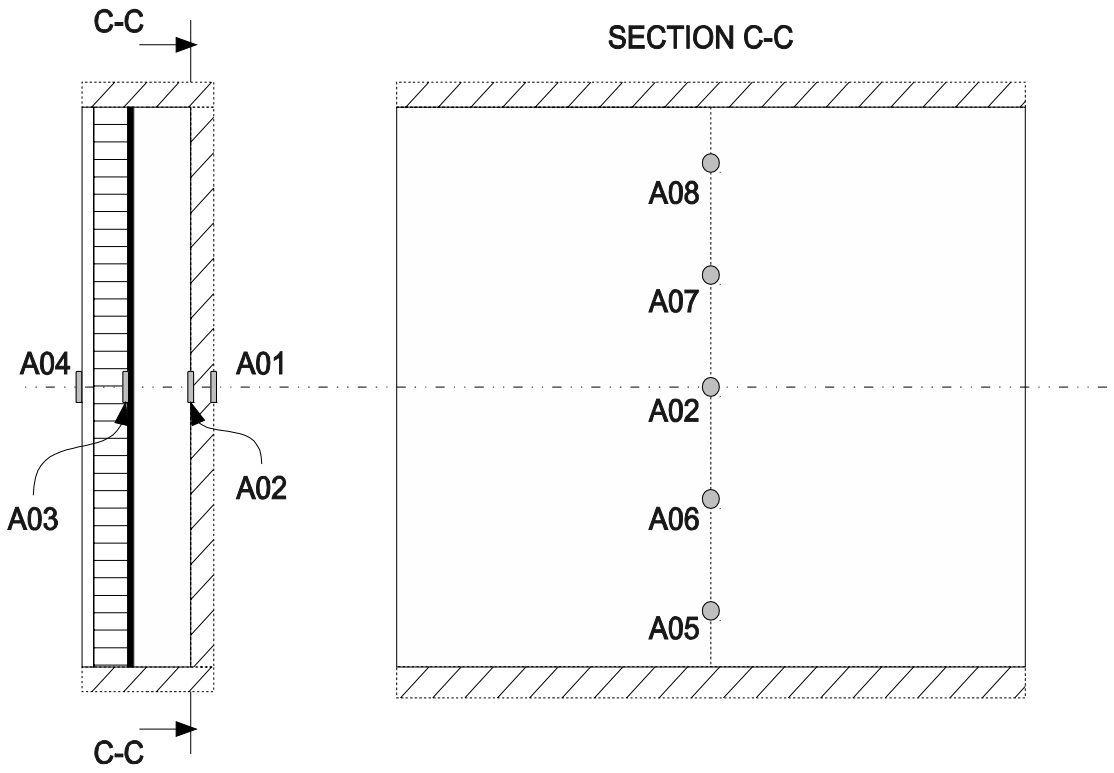

Fig. 2: Probe location in the integrated collector-storage element

The experimental facility is equipped with sensors to measure the temperatures in different façade zones and the meteorological data by means of a data acquisition system composed of a PC and a data acquisition unit. The metrological data registered during the experiment is: i) diffuse radiation on horizontal surface, ii) total radiation on horizontal surface, iii) outdoor ambient temperature, iv) wind velocity, v) wind direction, vi) relative humidity, vii) diffuse radiation on the façade surface, viii) total radiation on the façade surface, ix) indoor ambient temperature.

Regarding the integrated collector-storage element, temperatures at the indoor and outdoor wall surfaces, at the absorber plate, at both vertical confining walls of the parallelepiped storage tank, together with the temperatures within the storage element are registered. The locations of these thermocouple probes are shown in Figure 2.

Figure 3: parallelepiped storage element (left), transparent insulation material (right)

Pictures corresponding to the assembly of the collector-storage element are shown in Figure 3. On the left, the parallelepiped storage tank with some thermocouple sensors can be observed. On the right, the transparent insulation material glued on the single-pane glass skin can be seen.

In Figure 4, the appearance of the multi-functional façade element can be visualized from both sides. In the indoor view, the resistive thermal device (RTD) with radiation shield, and in the outdoor view, the pyranometers measuring the total and diffuse radiation on the façade surface can be noticed.

(a) (b)

Fig. 4: indoor (a) and outdoor (b) view of the multi-functional façade element

In order to study the CASE A, the ventilation channel is eliminated temporarily by removing the lower portion of the outer skin (see Figure 4.b). The upper portion of the ventilation channel adjacent to the inner double glazing is blocked as well.

The administration of the data acquisition unit is carried out by means of a data acquisition program developed in the CTTC.

3. Numerical Model

This work is based on the existing numerical platform (Damle et al., 2011) for the prediction of the thermal performance of buildings and solar systems. The buildings or solar systems are modeled as a collection of basic elements which can individually be solved for given boundary conditions. For each element, different levels of modeling can be employed, like one-dimensional or two-dimensional models, simplified energy balances or CFD models. The numerical platform permits linking different elements to form a specific configuration.

The global resolution algorithm of the numerical model is shown in Figure 5. At each iteration, inputs (e.g. pressure, temperature, etc.) are obtained from the neighbors, governing equations for each element are solved and the final outputs are supplied to the neighbor elements as boundary conditions. Iterations continue until convergence is reached at a given time step and next time step calculation starts as the variables are updated. Details of the numerical platform are explained in (Damle et al., 2011).

The main advantage of a modular object-oriented tool is the possibility of creating new elements/objects to model an innovative product while the rest of the elements to form a given configuration can remain unchanged. To model the present system, some existing objects with their respective numerical models are employed (e.g. OUTDOOR, COMPOSITE WALL, WALL, ROOM etc.) and two new objects are created, namely the *Glazed Areas and Transparent Insulation (TI) Layer* and the *Parallelepiped Storage Element*. The scheme of the system under study is shown in Figure 6.

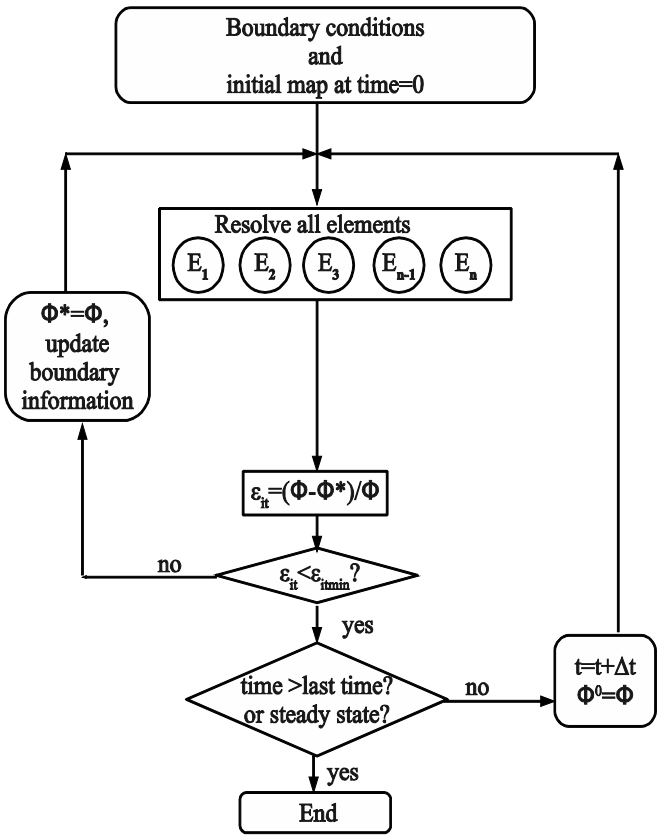

Fig. 5: Global resolution algorithm

As shown in Figure 6, an existing object is linked with two new objects to model the integrated storage element. The mathematical descriptions of the implemented objects are given below.

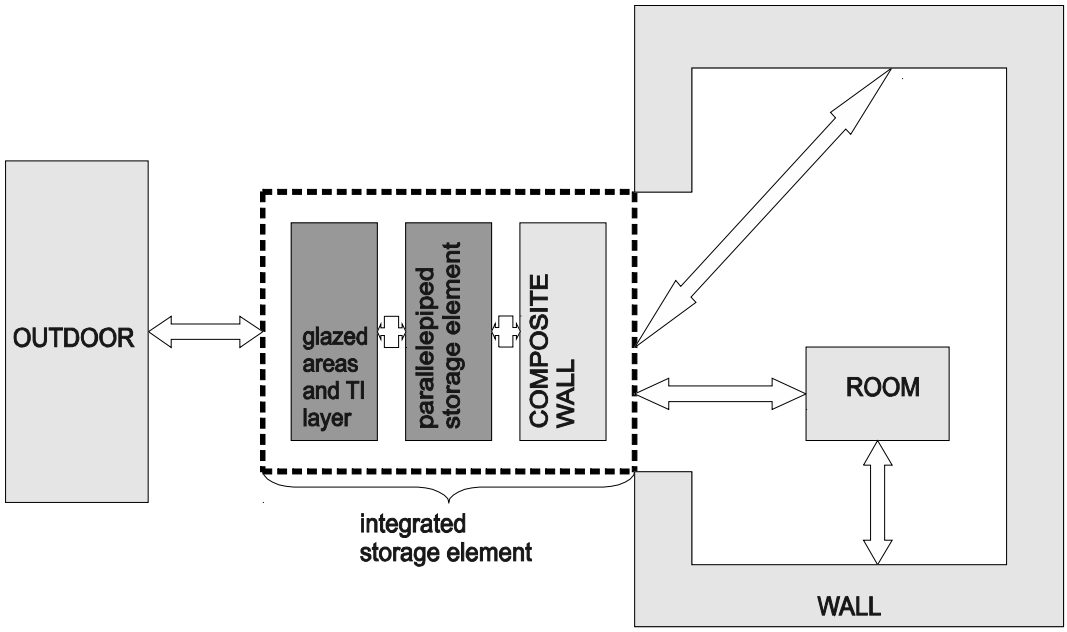

Fig 6: Scheme of the system as a collection of elements. Elements with uppercase letters represent existing elements.

3.1 Glazed Areas and TI Layer

In the resolution of transparent walls, one-dimensional energy conservation equation with an additional source term to include solar absorption is considered.

Governing equations for the phenomena taking place in TI layer are the so-called Radiative Transfer Equation (RTE) whose solution provides the field of Intensity, *I*, for all the domain and the directions, and the Energy Equation (EE) whose solution provides the field of temperatures.

The change in the intensity in the direction s is found by summing the contributions from emission, absorption, scattering, and in-scattering in the following form, neglecting the time dependence of the intensity (Modest, 1993):

$$\frac{dI}{ds} = \kappa_\eta I_{b\eta} - \beta_\eta I_\eta + \frac{\sigma_{s\eta}}{4\pi}\int_{4\pi} I_\eta(s_i)\phi_\eta(s_i, s)d\Omega_i \quad \text{(eq. 1)}$$

where $\kappa_\eta$is the linear absorption coefficient, $\sigma_{s\eta}$ is the linear scattering coefficient, ϕ_η is the scattering phase function, and β_η is the extinction coefficient defined as:

$$\beta_\eta = \kappa_\eta + \sigma_{s\eta} \quad \text{(eq. 2)}$$

If we write the above formulation in terms of non-dimensional optical coordinates,

$$\tau_\eta = \int_0^s (\kappa_\eta + \sigma_{s\eta})ds = \int_0^s \beta_\eta ds \quad \text{(eq. 3)}$$

and the single scattering albedo, defined as:

$$\omega_\eta = \frac{\sigma_{s\eta}}{\kappa_\eta + \sigma_{s\eta}} = \frac{\sigma_{s\eta}}{\beta_\eta} \quad \text{(eq. 4)}$$

leading to

$$\frac{dI_\eta}{d\tau_\eta} = -I_\eta + (1-\omega_\eta)I_{b\eta} + \frac{\omega_\eta}{4\pi}\int_{4\pi} I_\eta(s_i)\phi_\eta(s_i, s)d\Omega_i \quad \text{(eq. 5)}$$

Once eq. 5 is solved, field of intensity for all domain and all directions is obtained. RTE is coupled with EE which is of the following form:

$$\rho c_p \frac{DT}{dt} = \nabla\cdot(k\nabla T) - \nabla\cdot(\vec{q}_r) \quad \text{(eq. 6)}$$

where

$$\nabla\cdot(\vec{q}_r) = \kappa_\eta(4\pi I_b - \int_{4\pi} I d\Omega) \quad \text{(eq. 7)}$$

Eq. 7 is valid on spectral basis (for each wavelength) and states that the net radiation heat flux is equal to the emitted energy minus the absorbed irradiation. There is no scattering contribution in the radiation heat flux since scattering does not affect the energy content of any given unit volume.

The method of discrete ordinates (S_N-Approximation) (Modest, 1993) is used to discretize RTE. A one-dimensional model (intensity changing in the width direction of the TI material) assuming azimuth symmetry is adopted.

By means of the replacement of integrals over direction by numerical quadratures, like:

$$\int_{4\pi} f(s)ds = \sum_{i=1}^{n} \omega_i f(s_i) \quad \text{(eq. 8)}$$

where the $\omega_i$are the quadrature weights associated with the directions s_i. Thus the eq. 5 can be approximated by a set of n equations:

$$\frac{dI(r,s_i)}{ds_i} = \kappa(r)I_b(r) - \beta(r)I(r,s_i) + \frac{\sigma_s(r)}{4\pi}\sum_{j=1}^{n}\omega_j I(r,s_j)\Phi(r,s_i,s_j) \qquad \text{(eq. 9)}$$

$$i = 1, 2, \dots, n$$

For symmetry, n/2 equations are in positive and n/2 equations are in negative directions.

The intensity is considered not to vary within a cone of azimuthal θ around the axe of the width which is perpendicular to the vertical confining planes.

A discretization has been carried out in a one-dimensional control volume, where the temperatures and the radiative properties are determined at the discretization nodes, as shown in Figure 7.

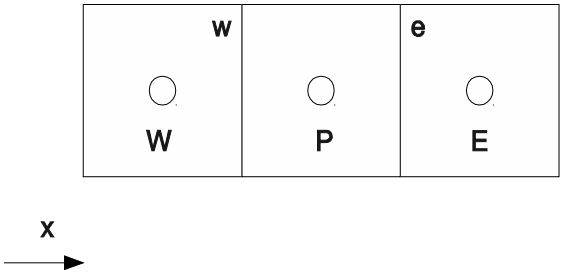

Fig. 7: Collocated mesh for RTE

Depending on the order of approximation (N=2, 4, 6, 8) eq. 9 can be expressed in a discrete way using the respective ordinates and weights. Finally n equations are solved to obtain the radiative intensities at the nodes (see Modest, 1993 for details). From eq. 7 radiation heat flux is evaluated. Discrete form of eq. 6 is solved for the temperature field, resulting in an iterative procedure.

Heat fluxes considering thermal radiation, solar radiation, and natural convection from the neighboring elements (Outdoor and Parallelepiped Storage Element) constitute the boundary conditions of this element.

3.2 Parallelepiped Storage Element

The well-known multinode model proposed by Kleinbach et al. (1993) has been adapted to simulate the storage element integrated in the façade. The model considers that the tank is divided into N totally mixed levels of temperature. In addition, the heat conduction between each of these segments is also considered.
Reviewing multinode mathematical formulation, for each i-th tank node, energy balance can be written as follows:

$$\rho c_p V \frac{dT_i}{dt} = h_w A_{i,w}\left(T_{wall,w} - T_i\right) + h_e A_{i,e}\left(T_{wall,e} - T_i\right) + k\frac{dT_i}{dy}S \qquad \text{(eq. 10)}$$

where ρ, c_p, k, and V are the density, specific heat capacity, conductivity, and volume of the fluid in segment i, h is the convection heat transfer coefficient in the storage element, A and S are the lateral and cross sectional area of the tank, T_{wall} is the temperature at the storage element inner wall, and T_i is the temperature of the fluid at segment i. Subscripts *w* and *e* correspond to west and east confining walls of the storage element.

The use of adequate empirical information regarding the convection heat transfer coefficient within the storage element is essential in performance prediction of these systems (Rodriguez et al., 2009). Suggested values in a recent CFD work for this geometry are employed (Kizildag et al., 2011) to model the convection heat transfer within the storage element.

Dirichlet boundary conditions at the west and east confining vertical walls are adopted to solve the equations. These wall temperatures are calculated by means of a global energy balance considering the neighbor elements.

4. Experimental Validation of the Model

The functioning of the implemented models has been tested by means of comparison with the experimental results. In this work only results corresponding to CASE A will be discussed. Mentioned experimental facility is used to register the meteorological data together with the relevant data corresponding to different zones of the integrated collector storage element. Part of the obtained data is used by the numerical model as boundary conditions.

To carry out the experimental validation, the data collected between the 31st March and 3rd Abril has been used. In Table 1 the measured data is given. The locations of the probes can be checked in Figures 2 and 4.

Tab. 1: Measured data

A01	Indoor wall temperature
A02, A05, A06, A07, A08	Temperatures at the east confining wall of the collector-storage element.
A03	Absorber temperature
A04	Outdoor wall temperature
01I	Total radiation on horizontal surface
01I_d	Diffuse radiation on horizontal surface
01I_t	Total radiation on façade surface
01W_v	Wind velocity
01W_d	Wind velocity direction
01Rh	Relative humidity
01T_{out}	Outdoor temperature
01T_{in}	Indoor temperature

As a preliminary study, three indicative temperature readings are compared with the numerically calculated values. Mentioned temperature evolution graphs are presented with respect to day of the year, as shown in Figure 7. In graph (a) the temperature at the indoor wall of the collector-storage element, and in graph (c) the temperature at the outdoor wall of the prototype can be observed. Both figures show an acceptable degree of agreement for the test period, however at the indoor wall the temperature is slightly overestimated by the numerical model. In graph (b) the temperature at the absorber plate is given. Although the numerical model can predict the temperature trend at this location, relatively greater discrepancies are observed. The numerical model underestimates the day-time peak temperature by about 1ºC and this underestimating behavior continues till the night time peak value is reached. During the cooling of the prototype after the day-time peak value, the discrepancies of more than 2ºC can be observed. Night-time peak values (minimum values). It is important to note that unlike the figures (a) and (c), in figure (b) a time shift between the experimental and numerical values is perceived. The different level of agreement during the day-time and night-time peak values in absorber temperature can be due to the model employed in glazed areas and TI layer.

Even though the results globally show a certain level of agreement, some discrepancies have been observed. Many factors can be considered to justify the discrepancies. Thermophysical and optical properties of the materials are obtained from the manufacturers, which can include some uncertainty. Moreover, some materials of the prototype may have degraded with time, thus giving rise to a change in the properties. Some assumptions regarding parameters like ground or indoor room reflectivities or view factors are not very precise as some recommended values are employed. The temperatures in the indoor (A01) and outdoor (A04) wall of the prototype are quite well predicted, which indicate that natural convection and thermal radiation phenomena are quite well approximated by the adopted empirical models, however the same is not

true for the absorber temperature (A03). This fact can be due to the difficulty in estimating the natural convection heat transfer coefficient within the collector-storage element, since the simple model used cannot reproduce the complex phenomena taking place in the tank. The model is unable to account for the laminar, transitional, turbulent, and relaminarization zones which coexist within the tank. The used natural convection heat transfer coefficient is obtained from steady state or statistically steady state calculations, while the phenomena under consideration are of transient character.

As a future work, using the modularity of the existing numerical platform, a CFD object which can reproduce the advanced physical phenomena taking place in the tank, or the test room, can be employed.

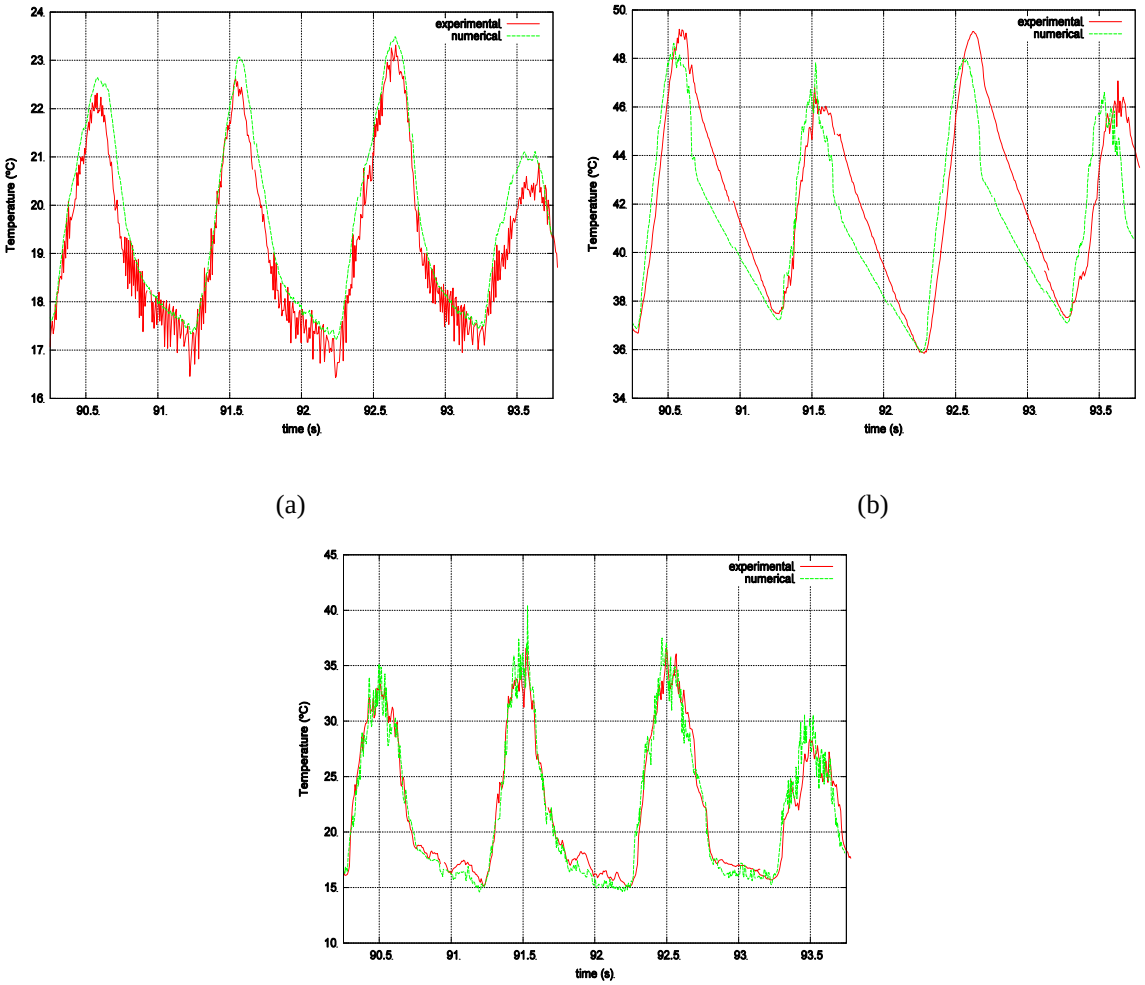

Fig. 7: Evolution of temperature at the (a) indoor wall (b) absorber plate (c) outdoor wall of the collector storage element

5. Conclusion and Future Work

A model to predict the thermal behavior of a multi-functional ventilated façade with a collector-storage element is implemented to an existing numerical platform. The comparison of the numerical and the experimental results indicates that the implemented model can be used to predict the thermal performance of the multi-functional façade with integrated storage element. The temperatures at the indoor and outdoor wall of the prototype are relatively well predicted while greater discrepancies are observed regarding the absorber plate temperature prediction. The well predicted values indicate that indoor and outdoor natural convection and thermal radiation phenomena are well approximated by the empirical model. The observed discrepancies can be due to various factors like the uncertainty in the termophysical and optical properties of the materials,

errors regarding some assumed values like ground and room optical properties, view factors within the prototype layers, and errors associated with the collector-storage element heat transfer coefficient which is evaluated for a statistically steady state situation, while the numerical simulation under study is of transient character. More efforts have to be made to check and improve the models in glazed areas and TI layer. More numerical and experimental tests have to be carried out for different time periods to assure the higher quality of the simulations.

As future work, once more confidence is built with the preliminary CASE A results, a more detailed work will be carried out considering CASE B. In parallel, the indoor conditions will be controlled by means of the construction of an inner test cell which will act as a calorimeter.

6. Acknowledgements

This work has been partially funded by the "Ministerio de Ciencia e Innovación, Secretaría de Investigación", Spain (ref. ENE-2009-09496).

7. References

1. Bloem, J.J., Baker, P.H., Strachan, P., Madsen, H., Vandaele, L., 2010. Dynamic Testing, Analysis and Modelling. http://www.dynastee.info

2. Damle, R., Lehmkuhl, O., Colomer, G., Rodriguez, I., 2011. Energy Simulation of Buildings with a Object-Oriented Tool. In Proceedings of the ISES Solar World Congress, Kassel, Germany.

3. Duffie, A., Beckman, W.A., 1991. Solar Engineering of Thermal Process. *John Wiley and Sons Inc*.

4. Faggembauu, D., Costa, M., Soria, M., Oliva, A., 2003. Numerical analysis of the thermal behaviour of ventilated glazed facades in Mediterranean climates. Part I: development and validation of a numerical model. *Solar Energy*, 75, pp 229-239.

5. Faggembauu, D., 2006. Heat transfer and fluid-dynamics in double and single skin façades. PhD Thesis. Universitat Politècnica de Catalunya (UPC), Terrassa.

6. Kizildag, D., Rodriguez, I., Oliva, A., 2011. On the validity of the Boussinesq approximation in a tall differentially heated cavity with water. In Proceedings of the *7th International Conference on Computational Heat and Mass Transfer*, Istanbul, Turkey.

7. Kleinbach, E.M., Beckman, W.A., Klein, S.A., 1993. Performance study of one-dimensional models for stratified thermal storage tanks. *Solar Energy*, Vol. 50, Issue 2, pp 155-166.

8. Modest, M.F., 1993. Radiative Heat Transfer. *McGraw-Hill*.

9. Pérez-Lombard, L., Ortiz, J., Pout, C., 2008. A review on buildings energy consumption information. *Energy and Buildings*, 40, pp. 394-398

10. Rodriguez, I., Castro, J., Perez-Segarra, C.D., Oliva, A., 2009. Unsteady numerical simulation of the cooling process of vertical storage tanks under laminar natural convection. *International Journal of Thermal Sciences*, Vol 48, Issue 4, pp 708-721.

Appendix B

Mesh refinement studies for LES

The success of the numerical simulations for the configuration under investigation is strongly dependent on the mesh resolution, since the flow has regions with different flow regimes, thus with time scales of different orders of magnitude. Different meshes have been tested in order to search for a good compromise between the accuracy and cost of the simulations, attaining the criteria of sufficient resolution in the boundary layer and the core of the cavity. Moreover, it has been observed that the streamwise resolution is particularly critical in order to capture the transition to turbulent location. The present investigation has shown that the transition phenomenon cannot be properly detected unless a moderately high streamwise resolution is used. Consequently, for the flow under consideration, the reduction in the grid with respect to the DNS solution is mainly in the wall-normal and spanwise directions, which are observed to be less critical in comparison with the streamwise direction.

In Figure B.1, the local average Nusselt number and streamwise velocity component are depicted for two coarse meshes (Mesh D and Mesh E) and a fine mesh (Mesh C) using WALE model (see Table B.1 for details). The results are compared with the DNS data. Note that the Mesh D and Mesh E are at least 4 times coarser than the Mesh C, which in turn is about 46 times coarser than the DNS mesh as the total number of CVs are concerned. It can be observed that the coarse mesh solutions highly overestimate the overall averaged Nusselt number due to very early transition to turbulence. Consequently, this causes a pronounced thickening in the boundary layer at mid height of the cavity. This is especially the case for the Mesh E which, despite having identical resolution to the fine mesh in wall-normal and spanwise directions, provides the poorest results due to insufficient resolution in the streamwise direction, thus indicating the influence of this direction in the model performance. Nevertheless, the Mesh C is capable of reproducing the time averaged results satisfactorily, due primarily to its performance in capturing the transition. Owing to the observed accuracy in the performed mesh refinement studies, it has been concluded that the Mesh C is an adequate mesh for obtaining results by means of LES for the present configuration.

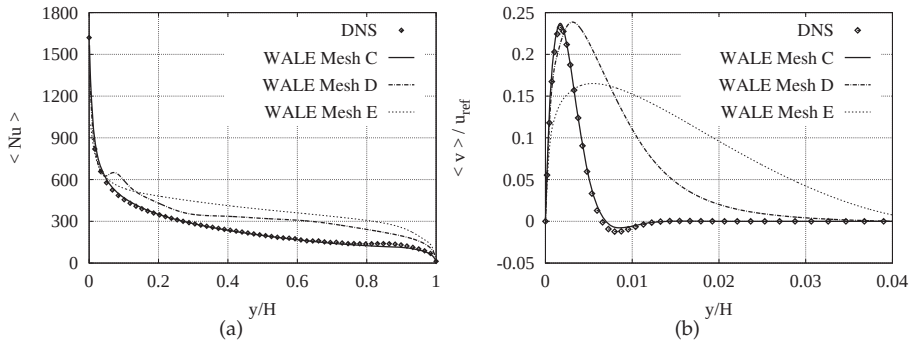

Figure B.1: Mesh refinement studies. (a) Local average Nusselt number (b) Streamwise velocity at mid height.

Mesh	N_x	N_y	N_z	$N_{tot} \times 10^{-6}$	γ_x	$(\Delta x)_{min}/H$
Mesh C	55	491	16	0.43	1.97	6.0×10^{-4}
Mesh D	33	319	8	0.08	2.15	8.0×10^{-4}
Mesh E	55	113	16	0.10	1.97	6.0×10^{-4}

Table B.1: Main parameters of the numerical simulations for LES. See the caption of Table 4.1 for details.

List of Publications

This is an exhaustive list of publications carried out within the framework of the present thesis.

On International Journals

Kizildag, D., Trias, F. X., Rodríguez, I., & Oliva, A. (2014). Large eddy and direct numerical simulations of a turbulent water-filled differentially heated cavity of aspect ratio 5. International Journal of Heat and Mass Transfer, 77, 1084-1094.
doi:10.1016/j.ijheatmasstransfer.2014.06.030.
http://dx.doi.org/10.1016/j.ijheatmasstransfer.2014.06.030.

Kizildag, D., Rodríguez, I., Oliva, A., & Lehmkuhl, O. (2014). Limits of the Oberbeck-Boussinesq approximation in a tall differentially heated cavity filled with water. International Journal of Heat and Mass Transfer, 68, 489-499.
doi:10.1016/j.ijheatmasstransfer.2013.09.046.
http://dx.doi.org/10.1016/j.ijheatmasstransfer.2013.09.046.

Kizildag, D., Rodríguez, I., & Castro, J. (2012). On the validity of the Oberbeck-Boussinesq approximation in a tall differentially heated cavity with water. Progress in Computational Fluid Dynamics, 12(4), 251-259.
doi:10.1504/PCFD.2012.048257, http://dx.doi.org/10.1504/PCFD.2012.048257.

Orozco, C., Kizildag, D., Oliva, A., & Pérez-Segarra, C. D., Verification of multidimensional and transient CFD solutions, Numer. Heat Transfer, Part B 57 (1) (2010) 46-73. doi:10.1080/10407791003613702.
http://dx.doi.org/10.1080/10407791003613702.

On Conferences Proceedings

Kizildag, D., Lehmkuhl O., Rigola, J., Capdevila, R., Oliva, A. (2015). Thermal Optimization Of Multi-Functional Ventilated Façades As Energy Efficient Solution In Retrofitting Of Public Buildings. In Proceedings of Building Simulation Conference 2015, Hyderabad (India).

Kizildag, D., Rodríguez, I., Trias, F. X., Oliva, A., Pérez-Segarra, C. D. (2015). Non-Oberbeck-Boussinesq effects in a turbulent tall water-filled differentially heated cavity. In Proceedings of the International Symposium Turbulence, Heat and Mass

Transfer 8, by K. Hanjalić, T. Miyauchi, D. Borello, M. Hadžiabdić and P. Venturini, Begel House Inc.

Kizildag, D., Rodríguez, I., Trias, F. X., & Oliva, A. (2014). Direct and large eddy simulations of non-Oberbeck-Boussinesq effects in a turbulent tall water-filled differentially heated cavity. In 11th World Congress on Computational Mechanics (WCCM XI) (pp. 1-9).

Deniz Kizildag, Oriol Lehmkuhl, Joaquim Rigola, & Assensi Oliva. (2014) A Multi-Functional Ventilated Façade model within a parallel and object-oriented numerical platform for the prediction of the thermal performance of buildings. EuroSun, Aix-les-Bains (France),

Joan Farnós, Jesus Castro, Sergio Morales, Eduardo García-Rivero, Assensi Oliva, & Deniz Kizildag. (2014) Preliminary results of a 7kW single-effect small capacity pre-industrial LiBr-H20 aircooled absorption machine. EuroSun, Aix-les-Bains (France),

Kizildag, D., Trias, F. X., Rodríguez, I., & Oliva, A. (2013). Direct ans large eddy simulation of non-Oberbeck-Boussinesq effects in a turbulent differentially heated cavity. In Direct and Large-Eddy Simulation IX. Dresden, Germany.

Kizildag, D., Rodríguez, I., & Oliva, A. (2011). On the validity of the Boussinesq approximation in a differentially heated cavity with water. In 7th International Conference on Heat and Mass Transfer (ICCHMT 2011), Istanbul, Turkey.

Kizildag, D., Rodríguez, I., & Oliva, A. (2011). Developement of a multi-functional ventilated facade with an integrated collector-storage: numerical model and experimental facility . In ISES World Conference 2011, Kassel, Germany.

Kizildag, D., Ventosa, J., Rodríguez, I., & Oliva, A. (2010). Non-Oberbeck-Boussinesq natural convection in a tall differentially heated cavity. In V European Conference on Computational Fluid Dynamics ECCOMAS CFD 2010 Methods (pp. 1-13), Lisbon, Portugal.

Kizildag, D., Pérez-Segarra, C. D., Oliva, A., & Rodríguez, I. (2008). Numerical simulations of natural convection of flow in a rectangular cavity under transient boundary conditions. In 5th European Congress on Computational Methods in Applied Sciences and Engineeering (ECCOMAS 2008), Venice, Italy.